ELECTRONIC TRANSPORT STUDIES ON GaN EPITAXIAL LAYERS FOR THE FABRICATION OF RADIATION HARD ULTRAVIOLET PHOTODETECTORS

By

ABHISHEK CHATTERJEE

PHYS03201504011

Raja Ramanna Centre for Advanced Technology,

Indore - 452013, India

A thesis submitted to the

Board of Studies in Physical Sciences

In partial fulfillment of requirements

for the Degree of

DOCTOR OF PHILOSOPHY

of

HOMI BHABHA NATIONAL INSTITUTE

March, 2021

Homi Bhabha National Institute

Recommendations of the Viva Voce Committee

As members of the Viva Voce Committee, we certify that we have read the dissertation prepared by **Shri Abhishek Chatterjee** entitled "**Electronic transport studies on GaN epitaxial layers for the fabrication of radiation hard ultraviolet photodetectors**" and recommend that it may be accepted as fulfilling the thesis requirement for the award of Degree of Doctor of Philosophy.

Chairperson – **Prof. Aparna Chakrabarti** Aparna Chakrabarti	**Date:** 19.3.2021
Guide / Convener – **Prof. Tarun Kumar Sharma**	**Date:** 19/03/2021
Examiner- **Prof. Rajendra Singh**	**Date:** 19/03/2021
Member 1- **Prof. Anil Kumar Sinha**	**Date:** 19/03/21
Member 2- **Prof. Maulindu Kumar Chattopadhyay** M K Chattopadhyay	**Date:** 19/03/2021
External Member - **Prof. Sandip Ghosh** Sandip Ghosh	**Date:** 19/3/2021

Final approval and acceptance of this thesis is contingent upon the candidate's submission of the final copies of the thesis to HBNI.

I hereby certify that I have read this thesis prepared under my direction and recommend that it may be accepted as fulfilling the thesis requirement.

Date: 19/03/2021

Place: RRCAT, Indore

Tarun Kumar Sharma

STATEMENT BY AUTHOR

This dissertation has been submitted in partial fulfillment of requirements for an advanced degree at Homi Bhabha National Institute (HBNI) and is deposited in the Library to be made available to borrowers under rules of the HBNI.

Brief quotations from this dissertation are allowable without special permission, provided that accurate acknowledgement of source is made. Requests for permission for extended quotation from or reproduction of this manuscript in whole or in part may be granted by the Competent Authority of HBNI when in his or her judgment the proposed use of the material is in the interests of scholarship. In all other instances, however, permission must be obtained from the author.

Abhishek Chatterjee

DECLARATION

I, hereby declare that the investigation presented in the thesis has been carried out by me. The work is original and has not been submitted earlier as a whole or in part for a degree / diploma at this or any other Institution / University.

Abhishek Chatterjee

List of Publications arising from the thesis

Journal

1. "Dislocations limited electronic transport in hydride vapour phase epitaxy grown GaN templates: A word of caution for the epitaxial growers",

   Abhishek Chatterjee, Shailesh K. Khamari, R. Kumar, V. K. Dixit, S. M. Oak, and T. K. Sharma, *Applied Physics Letter*, (**2015**), 106, 023509 (5).

2. "Dislocation-assisted tunnelling of charge carriers across the Schottky barrier on the hydride vapour phase epitaxy grown GaN ",

   Abhishek Chatterjee, Shailesh K. Khamari, V. K. Dixit, S. M. Oak, and T. K. Sharma, *Journal of Applied Physics*, **(2015)**, 118, 175703 (7).

3. "Effect of ^{60}Co gamma irradiation on the nature of electron transport in highly n-type GaN Schottky photodetector ",

   Abhishek Chatterjee, Shailesh K. Khamari, S. Porwal, S. Kher, and T. K. Sharma, *Journal of Applied Physics*, (**2018**), 123, 161585 (8).

4. "Peculiarities of the current-voltage and capacitance-voltage characteristics of plasma etched GaN and their relevance to n-GaN Schottky photodetectors",

   Abhishek Chatterjee, V. K. Agnihotri, Shailesh K. Khamari, S. Porwal, A. Bose, S.C. Joshi and T. K. Sharma, *Journal of Applied Physics*, (**2018**), 124, 104504 (10).

5. "Role of ZrO_2 Passivation Layer Thickness in the Fabrication of High Responsivity GaN Ultraviolet Photodetectors ",

   Abhishek Chatterjee, Shailesh K. Khamari, S. Porwal, and T. K. Sharma, *Physica Status Solidi: Rapid Research Letters*, (**2019**), 3 1900265 (6).

6. "Optimization of the growth of GaN epitaxial layers in an indigenously developed MOVPE system",

   Abhishek Chatterjee, V. K. Agnihotri, R. Kumar, S. Porwal, A. Khakha, Jayaprakash G., Tapas Ganguli and T. K. Sharma, *Sadhana*, (**2020**), 45, 249.

7. "Role of threading dislocations and point defects in the performance of GaN-based metal-semiconductor-metal ultraviolet photodetectors",

   Abhishek Chatterjee, Shailesh K. Khamari, R. Kumar, S. Porwal, A. Bose and T. K. Sharma, *Superlattices and Microstructures*, (**2020**), 148, 106733 (9).

Conferences

1. "An Accurate Measurement of Carrier Concentration in an Inhomogeneous GaN Epitaxial Layer from Hall Measurements",

   Abhishek Chatterjee, Shailesh K. Khamari, V. K. Dixit, T. K. Sharma and S. M. Oak, *Proceedings of 17th International Workshop on the Physics of Semiconductor Devices, Springer*, **(2014)**, p. 767.

2. "Structural and Optical Properties of GaN Epi-layers grown by Indigenously Developed Nitride MOVPE System",

   Abhishek Chatterjee, Shailesh. K. Khamari, V. K. Dixit, T. K. Sharma and S. M. Oak, *18th International Workshop on the Physics of Semiconductor Devices,* **December 2015**, IISc Bangalore, India.

3. "Reactive ion etching induced damage in n-type GaN and its recovery by treatment with O_2 plasma",

   Abhishek Chatterjee, Mohit Gupta, V. K. Agnihotri, S. Porwal and T. K. Sharma, *4th International Symposium on Semiconductor Materials and Devices*, **March 2017**, Kolkata, India.

4. "Effect of capacitance hysteresis on the performance of GaN metal-oxide-semiconductor photodetectors",

   Abhishek Chatterjee, Shailesh K. Khamari, S. Porwal and T. K. Sharma, *19th International Workshop on the Physics of Semiconductor Devices,* **December 2017**, Delhi, India.

5. "Impact of post deposition annealing of ZrO_2 insulating layer on the performance of GaN metal-semiconductor-metal ultraviolet photodetectors ",

   Abhishek Chatterjee, Shailesh K. Khamari, S. Porwal and T. K. Sharma, *4th International Conference on Emerging Electronics,* **December 2018**, Bangalore, India.

   DOI: 10.1109/ICEE44586.2018.8938018.

6. "Influence of threading dislocations on the performance of GaN-based ultraviolet photodetectors ",

   Abhishek Chatterjee, S. K. Khamari, S. Porwal A. Bose and T. K. Sharma, *20th International Workshop on the Physics of Semiconductor Devices,* **December 2019**, Kolkata, India.

Abhishek Chatterjee

Dedicated to my parents, wife and little 'Adi'….

ACKNOWLEDGEMENTS

A successful completion of my Ph.D. work is the result of dedicated efforts put by many others and this report would be incomplete without giving credit to them. Hereby I would like to thank them all, as each of them contributed, in one way or another, to my growth from both a professional and a human points of view.

Firstly, I would like to express my sincere gratitude to my Ph.D supervisor, Prof. Tarun Kumar Sharma, whose constant encouragement, guidance, support and valuable discussions motivated me immensely to pursue good quality research work during this period. In this long duration of my Ph.D., there are phases when things don’t move in my favor despite of hard work. He always stood behind me in those tough times which is unforgettable.

Besides my supervisor, I would like to thank Prof. Vijay Kumar Dixit and Dr. Shailesh Kumar Khamari who taught me the art of experiments and science behind the data analysis. They are like open books for me, always willing to share scientific knowledge without any hesitation. The day-to-day interaction with them helped me significantly to improve my scientific skills.

I would like to thank my Ph.D. Doctoral committee, HBNI for the rigorous evaluation of my thesis work and their insightful comments which helped me a lot to improve my research skills and motivated me to analyze the experimental data in more detail.

I would like to thank Mr. Sanjay Porwal for helping me establish the experimental set up in the spectroscopy lab. He is a person with huge experience in spectroscopy and it seemed that the signals never dared to come without his critical approval!

Thanks are due to Mr. Alexander Khakha, without whose help measurement of transient response of GaN detectors would not have been possible. I would also like to acknowledge the company of Mr. Vishal Agnihotri in MOVPE and RIE lab. I'm grateful to him for providing all kind of support while performing experiments. I'm thankful to Dr. Ravi Kumar for the XRD measurements of GaN epilayers and Dr. Neha Sharma for her support in performing AFM measurement in few samples. Special thanks to Mrs. Geetanjali, Ms. Payal Taya and Mr. Rijul Roychowdhury for their support. I'm also thankful to Mr. G. Jayaprakash, Mr. U. K. Ghosh and Mr. A. K. Jaiswal for the technical support I have received from them time to time.

I would like to thank Mr. Aniruddha Bose of SCRF CC & CS, RRCAT for the SIMS measurements and Smt. Rashmi Singh, Smt. S. Bhartiya, and Mr. M. K. Singh of LMD, RRCAT, for their help in the SEM measurements. Thanks also to Dr. D. Jana and Dr. S. Haldar for many scientific discussions during their stay at RRCAT.

I acknowledge Homi Bhabha National Institute (HBNI), Mumbai for providing me the opportunity to pursue my Ph.D. and Prof. Arup Banerjee, Dean Academics, HBNI for his constant support on academic and administrative fronts. I am also thankful to Shri Debashis Das, Director, RRCAT and Shri S. V. Nakhe, Director, Materials Science Group for their kind support during the entire work.

Above all, I'm thankful to my parents and my family members for their unconditional support. A special thanks to my wife Sanchita, who was always with me during happy and sad moments with her endless support and warmest love. No word would be good enough to express my appreciation to her.

Abhishek Chatterjee

CONTENTS

LIST OF FIGURES

LIST OF TABLES

Chapter 8

Summary and Future Scope

8.1 Summary of the thesis work

During the course of this thesis, novel electrical characterization techniques are used to investigate the electronic transport in GaN epitaxial layers and Au/Ni/GaN UV detector for potential application in harsh radiation environment. An indigenously developed nitride MOVPE growth system is used for the epitaxial growth of GaN. However, the crystalline quality of GaN layers is found to be rather modest, where a high background carrier concentration makes them unsuitable for photodetector applications. In-depth electronic transport measurements are thereafter performed on commercially available MOVPE and HVPE grown GaN samples. Further, a good control on the dislocation formation during epitaxial growth and a knowledge of dislocation behaviour are the two pre-requisite for optimizing the performance of nitride devices. These two issues are addressed in this thesis where 1) results from the epitaxial growth of GaN are presented by highlighting the issues related to dislocation density, and 2) role of dislocations in the performance of GaN based radiation hard UV photodetectors is explored. In particular, results from the MSM and MOS configurations of GaN photodetectors are presented, where a state-of-the-art performance of GaN based MOS devices is demonstrated.

Systematic electronic transport measurements are performed on 5 μm thick GaN/Sapphire epilayers grown by HVPE and MOVPE technique to understand the fundamental mechanisms associated with current conduction in GaN epilayers and Schottky diode under various experimental conditions. It is found that though the two samples possess a carrier density of ~2×10^{18} cm^{-3}, their electrical characteristics are very different. It is observed that the carrier concentration measured by Hall for HVPE grown samples is two orders larger than the value provided by C-V technique. Such a large difference in carrier concentration is associated with the formation of a degenerate layer at the layer-substrate interface, which is consisted of a large density of threading screw and edge dislocations. A 2-layer model is used to extract the appropriate values of carrier concentration of HVPE grown samples from Hall data. It is learnt that there exists a critical thickness of HVPE GaN epilayers below which the electronic transport properties of layers grown on top of them are severely limited by the interfacial charged dislocations. On the contrary MOVPE grown samples are found to be free from such limitations, which makes them attractive for device fabrication. Further, the impact of dislocations on the electronic transport properties of Au/Ni/GaN Schottky diodes fabricated on HVPE GaN template is evaluated. It is found that one needs to consider the activation of two donors operating in the two separate temperature ranges for understanding the temperature dependence of ideality factor. The two donors correspond to the fundamental mechanisms associated with 1) TE of carriers from bulk donors that dominates at high temperature, and 2) TFE associated with charged dislocations that dominates at low temperature.

Once the electronic transport in GaN epilayer and across Au/Ni/GaN Schottky diode is understood, attention is paid to fabricate GaN MSM UV detectors. From electronic transport studies, it is found that the HVPE GaN epilayers are largely influenced by the threading dislocations. On the other hand, MOVPE GaN epilayers are found be free from such limitations. It is therefore obvious that MOVPE GaN epilayers might be a preferred choice for the fabrication of optoelectronic devices. However, a high cost associated with MOVPE GaN epilayers becomes a major factor that compels researchers to look for other alternatives like HVPE GaN epilayers. MSM photodetectors are made on MOVPE and HVPE GaN epilayers for comparison purpose. Contrary to above, it is surprising to note that the photo response of HVPE based PDs is ~3 times higher than that of the MOVPE based devices. Further, the overall performance of HVPE based PDs is found to be better than those fabricated on MOVPE GaN, in spite of the variations in device geometry or the operating conditions. It is explained by considering the difference in the depletion width which is primarily determined by the different procedures adopted for the doping of HVPE and MOVPE GaN templates. A large carrier concentration at the edge of the depletion width in MOVPE grown GaN epi-layer leads to higher (lower) leakage current (barrier height) despite a low dislocation density. Moreover, Si doping leads to generation of Ga vacancies which act as deep level defects leading to further rise of leakage current and reduction of photo response. In temperature dependent I-V measurements, a sharp change in the value of characteristics tunnelling energy is seen at ~200 K for HVPE GaN, to show the switching of electronic transport mechanism from TE to TFE during the cooling down. On the other hand, TFE is found to be the dominant transport mechanism at all temperature in devices fabricated on MOVPE GaN. The understanding developed here indicates that controlling the density of threading dislocations is not the sole criteria for improving the performance of GaN Schottky PDs, rather one also need to be careful about the density of point defects which can also marginalize the key figure-of-merits. With an aim of improving the device performance further, GaN MOS detector is fabricated by including an oxide layer in the device architecture. The oxide passivated samples show a relatively flat response in shorter wavelength side due to a suppressed surface recombination of photo generated carriers. Moreover, at an optimum ZrO_2 thickness of 3 nm, a high photo responsivity of 27 A/W is achieved along with the fast response of the device with a rise (fall) time of 28 ms (178 ms), respectively. It is also found that the thickness of ZrO_2 layer plays a critical role in controlling the photo-response and transient response of the devices. However, beyond an optimum thickness of oxide interlayer, the device response slows down along with a reduction in responsivity which is mainly governed by the impediment of hole tunnelling across the oxide layer. It is worth to note that the detectivity of PDs with optimized thickness of ZrO_2 interlayer is found to be similar or better than the recently reported state-of-the-art values for visible blind UV GaN PDs with similar dark current.

Fabrication of GaN PIN detector in vertical geometry requires selective spatial etching of the material. In case of GaN, plasma etching is a preferred method since wet chemical etchants are not available. However, during this process, several kinds of plasma-induced damages can lead to the creation of lattice defects and dislocations, ion implantation or formation of dangling bonds on the surface. Impact of RIE induced damage on the optoelectronic properties of GaN epilayers and also on the photoresponse of Schottky PDs is investigated further. The observation of surface morphology of GaN epilayers post RIE confirms a large degradation with increasing energy of the reactive ion beam. More than 70% reduction in the intensity of near band edge PL peak is observed after 250W RF BCl_3 plasma etching which along with the etch insensitive YL band suggests that etch induced non-radiative centres are located rather close to the surface. This observation is further supported by C-V measurements on Au/Ni/GaN Schottky diodes which along with SIMS results confirm that the RIE induced damage is mostly confined within 100 nm from the sample surface. The peak spectral response of PDs also shows up to 90% reduction post plasma etching. A method for the recovery of plasma etch induced damage by O_2 plasma treatment is also demonstrated. A substantial recovery of the spectral and transient response along with an improved deep UV response of PDs is achieved through O_2 plasma treatment. Availability of this knowledge shall be highly beneficial in gaining the required understanding of RIE induced damage and also in the minimization of plasma etch induced degradation in the performance of GaN devices.

One of the major aims of this thesis is to test the performance of devices under high radiation environment. Here, the effect of ^{60}Co gamma irradiation on the electronic transport properties of heavily doped n-type GaN epilayers and Schottky PDs is investigated. A steady rise of carrier concentration with increasing irradiation dose is observed. By considering a 2-layer model, the contribution of interfacial dislocations in carrier transport is isolated from that of the bulk layer for both the pristine and irradiated samples. It is found that no new kind of electrically active defects are generated by gamma radiation even at 500 kGy dose. The irradiation induced rise of carrier concentration is attributed to the activation of native Si impurities that are already present in an electrically inert form in the pristine sample. This observation is found to be unique, especially for highly conducting samples. It is also seen that the irradiation induced nitrogen vacancies stimulate the diffusion of oxygen impurities, leading to the observed increase of the interfacial carrier concentration. Further, the leakage current of GaN PDs is compared with that of GaAs which clearly demonstrates a high radiation resistance of GaN. A fast self-recovery of photo response within a day after irradiation is also demonstrated, which signifies the compatibility of devices for operation in high radiation zones.

In conclusion, it is essential to understand the electronic transport properties of GaN/Sapphire epitaxial layers and the role of charged dislocations lying at the interface, prior to the fabrication of devices. A comparison of the spectral and transient response of PDs fabricated on GaN templates can help the device manufacturers in making a judicious choice of GaN templates. Further, an optimum thickness of ZrO_2 layer is needed for the development of state-of-the-art GaN PDs. Radiation resistant nature of GaN PDs along with a fast self-recovery makes them attractive for possible applications in high radiation zones. The understanding developed in this thesis is useful for the development of high performance radiation hard GaN ultraviolet PDs.

8.2 Scope for future work

The understanding developed in the present thesis can be further strengthened by addressing several unresolved issues in the fabrication and characterization of GaN epitaxial layers and UV detectors that deserve further investigations. In presence of a large density of structural defects and dislocations in GaN, it is really challenging to grow superior quality GaN epitaxial layers on Sapphire. Optimization of the epitaxial growth parameters to achieve low background free carrier density is one of the major requirement to improve the performance of the GaN UV detectors. Controlling the density of defect and trap centres will not only reduce the dark current but also encourage faster response of the device since it will reduce the response delay due to hole trapping at the defect centres. Growth of epitaxial lateral overgrowth (ELOG) GaN epilayers on patterned substrates need to be explored in this context as this is a very promising approach for effective reduction in dislocation density of GaN epilayers. Also conductive atomic force microscopy (C-AFM) surface scan can help in obtaining the information about the electrically active dislocations present at the GaN surface which largely controls the low temperature carrier transport. In device aspect, scaling down the dimension of the MSM electrodes is the necessary requirement to achieve advancement in existing device performance. This will help in reducing the dark current and improve the responsivity and detectivity as well as transient response time of the device. Also a detailed analysis of GaN PIN detector is required to explore the new possibilities that PIN detector offers including detection of very weak signal. In this context, the role of dry etching for the fabrication of PIN detector can be better understood by using ICP RIE technology with which it is possible to decouple ion current and ion energy applied to the wafer, enlarging the process window.

In the radiation hard detector application part, performance evaluation under different radiation environment like neutron, electron, x-rays is necessary to demonstrate versatile applications of the device in the radiation field. Also understanding the role of high temperature annealing for quick recovery the radiation induced damages in these detectors will be highly beneficial for the field applications of these detector devices.

SUMMARY

This thesis deals with the fabrication of high performance GaN based ultraviolet (UV) photodetectors (PDs) for potential application in high radiation environment. Owing to a wide band gap, GaN based optoelectronic devices are capable to operate under high electric field often exceeding 1 kV and at high temperatures up to 600 ^{o}C. However, a large density of dislocations in nitride heterostructures is often proven to be a limiting factor. Thus, a good control on the dislocation formation during epitaxial growth and a knowledge of dislocation behaviour are the two pre-requisite for optimizing the performance of nitride devices. The two issues are addressed in this thesis where 1) results from the epitaxial growth of GaN are presented by highlighting the issues related to dislocation density, and 2) role of dislocations in the performance of GaN based radiation hard UV photodetectors is explored. An indigenously developed nitride Metal Organic Vapour Phase Epitaxy (MOVPE) system is used for the epitaxial growth of GaN epitaxial layers. However, the crystalline quality of GaN layers is found to be rather modest, where a high background carrier concentration makes them unsuitable for photodetector applications. In-depth electronic transport measurements are thereafter performed on commercially available MOVPE and Hydride Vapour Phase Epitaxy (HVPE) grown GaN samples. Presence of a highly conducting interfacial layer is observed in HVPE GaN epilayers. On the other hand, MOVPE GaN epilayers are found to be free from this limitation which makes them attractive for the device development. Metal-semiconductor-metal (MSM) PDs are thereafter made on both the samples where the performance of devices made on HVPE GaN turns out to be better, which is rather surprising. It is explained by citing the difference in doping method of the GaN epi-layers in the two samples. A method to enhance the detector performance is demonstrated by the insertion of a thin layer of ZrO_2 in metal-oxide-semiconductor (MOS) geometry. Here, the role of ZrO_2 layer thickness is found to be rather critical where the specific detectivity of PDs is found to be similar or better than the

state-of-the-art values reported in literature. Further, the role of dry etching in the fabrication of GaN PIN detectors in vertical geometry is discussed where a method to recover the etching induce damage is demonstrated by using post etch O_2 plasma treatment. A few samples are also exposed to a high dose of ^{60}Co gamma rays which proves the radiation resistant nature of indigenously developed PDs along with a fast self-recovery, which signifies their usefulness for possible applications in harsh radiation environment. Systematic electronic transport measurements are performed to understand the fundamental mechanisms associated with current conduction in GaN epilayers and PDs under various experimental conditions. The understanding developed in this thesis is useful for the development of high performance radiation hard GaN ultraviolet PDs.

Chapter 1

Introduction

Recent advances in the research on GaN semiconductors have led to a significant progress in the development of GaN based ultraviolet (UV) photodetectors (PDs) for light detection in the UV spectral range of 220–360 nm [1, 2]. These detectors find several applications including visible blind UV detection, usage in strategic sectors, UV astronomy, medical science, and also in the industry as flame detectors and solar UV monitors [1, 3, 4]. This chapter provides an introduction to GaN, and in particular its applications in UV detectors. Various types of GaN-based PDs, such as p–n junction, p-i-n diodes, Schottky barrier and metal–semiconductor–metal (MSM) detectors are described. Different current transport mechanisms across the metal-semiconductor (MS) junction in these photodetectors are discussed. Further, the advantage of GaN as a radiation hard detector is described in brief. At the end of this chapter, organization of the present thesis is given in brief.

1.1 Progressive development of GaN research

During the last five years, evolution of GaN technology has been phenomenal, however, the research on GaN began in the 1930s when Juza and Hahn first synthesized small needles of GaN by passing ammonia (NH_3) over liquid gallium (Ga) at elevated temperatures [5]. Their purpose was to study the crystal structure and lattice constant of GaN. In 1968, Maruska and Tietjen were the first to grow large area GaN layers on sapphire by hydride vapour phase epitaxy (HVPE) technique [6]. Sapphire was chosen as the substrate material because of its favoured crystal structure, ease of availability, good thermal conductivity and the inert nature since is doesn't react with ammonia. Even today, it remains the most preferred substrates for the fabrication of optoelectronic devices based on GaN and its alloys, irrespective of having a large lattice mismatch of ~14% with GaN. In all the early GaN samples, a very high background dopant density of the order of ~ 10^{20} cm^{-3} was measured by the researchers [6, 7]. Several defect centres were proposed that could give rise to such a high background doping in GaN. Nitrogen vacancy (V_N) was believed to be a responsible candidate behind such observation [6]. However, later oxygen was proposed as the responsible donor on N site, resulting as a single donor in GaN [7]. By this time, researcher also began to demonstrate p-type doping in GaN such that a p-n junction based optoelectronic device could be made [6, 7]. Researchers tried Germanium (Ge), Zinc (Zn) as a potential p-type dopant since it works as an acceptor in conventional III-V semiconductors. However, it was found that heavy Zn doping rendered GaN films to be insulating, and films never became of p-type nature [6, 7]. In 1972, Magnesium (Mg) was proposed to be a better replacement of Ge and Zn for p-type doping by Maruska *et al.* [8] which has remained the choice for p-type doping in all commercial GaN-based optoelectronic devices till date. In the late 1970s, GaN research virtually halted everywhere because of the difficulties in achieving high quality GaN films on foreign substrate, controlling very high back ground doping and difficulty in achieving p-type conductivity. It was the dedicated efforts of Amano *et al*. that eventually resulted in good quality GaN epitaxial layers [9] and also in achieving p-type concavity of GaN in 1989 [10]. In 1986, Amano *et al*. reported high quality GaN film with improved surface morphology, and superior optoelectronic properties grown by metal organic vapour phase epitaxy (MOVPE) on sapphire using a low-temperature (600°C) AlN nucleation layer. GaN epitaxial layer was grown at 1050°C on this nucleation layer [9]. It is also understood that during Mg doping, the shallow acceptor level of Mg was compensated by hydrogen atom forming Mg:H complex which prohibits p-type conduction [11]. However, using high energy electron beam or annealing GaN:Mg films above

750^{o}C in N_2 ambient or vacuum, the complex can be broken converting the material to be of p-type nature [12]. The breakthroughs in GaN research by Amano, Akasaki and Nakamura led to the revival of GaN material research at big scale in early 1990s. A great potential of GaN technology was thereafter realized by the research community which led to the commercialization of many novel devices, thus making GaN the second most sought semiconductor after Silicon.

1.2 Important properties of GaN

There are several applications where conventional III–V semiconductors cannot be used. Traditional silicon and GaAs based detectors are not suitable for operation in UV spectral regime. Further, these materials cannot be used at high temperatures. GaN is particularly suitable for applications in those areas. Due to the direct and wide band gap, GaN has shown enormous potential in the area of solid state lighting. Table 1.1 shows the fundamental properties of some of the most important semiconductor materials for optoelectronic device fabrication [13-16]. A large band gap of GaN enables its operation under high electric field. GaN and SiC have two to three times larger band gap than the conventional semiconductors. They possess very high breakdown fields as can be seen from Table 1.1, typically about an order higher than the conventional semiconductors. Furthermore, it permits the material to withstand greater operating temperatures. The higher radiation hardness of GaN in comparison to Si and GaAs enables its application as radiation hard detector. Though GaN have lower mobility compared to Si, GaAs and InP, the higher electron saturation velocity enables fast response time of the device due to high carrier drift velocity at a considerably large electric fields.

Table 1.1 Comparisons of material parameters of conventional and wide-bandgap semiconductors used for detectors [13-16]

Property	GaN	SiC	Diamond	Si	GaAs	InP
Bandgap (eV)	3.44	3.26	5.45	1.12	1.43	1.35
Electric breakdown Field (MV/cm)	3	3	10	0.3	0.4	0.5
Electron saturation velocity [10^7 cm/s]	2.5	2.0	2.7	1.0	1.2	1.8
Electron mobility ($cm^2/V \cdot s$)	900	700	4800	1500	8500	5400
Thermal conductivity ($W/cm \cdot K$)	1.3-2.1	3.7-4.5	22	1.5	0.5	0.7
Relative Permittivity (ε_r)	9.0	10.1	5.5	11.8	12.8	12.5
Displacement energy (eV)	20/10	35/20	43	13-25	10	3/8

Wide band gap semiconductors are having smaller ε_r, about 20% lower compared to the conventional semiconductors. This allows the active area of a GaN based device to be about 20% larger for a given impedance. Another important parameter of any semiconductor material for device application is its thermal conductivity. A high thermal conductivity ensures that the dissipated power can be easily extracted from the device thus enabling high temperature operation. As can be seen from Table 1.1, the conventional semiconductors like GaAs and InP are poor thermal conductors, on the other hand, SiC and diamond are excellent thermal conductors. However, thermal conductivity of GaN is considerably higher than GaAs and InP, and is comparable to Si. Further, the fact that GaN can tolerate higher temperatures makes the processing of GaN based optoelectronic devices rather attractive.

Although great achievements have been made in GaN based optoelectronic devices, there are several difficulties in growing good quality GaN films. In order to demonstrate electronic devices with superior performance, background free carrier density must be restricted. However, in material like GaN with large density of line and point defects, a proper control of the electrical parameters such as mobility and background carrier density becomes very difficult. The lack of a suitable substrate for GaN growth is the primary obstacle in growing high crystalline quality material. This is because the growth of bulk GaN is limited only at an extremely high pressure of ~15 kbar of N_2 over Ga melt at a temperature of 1400 °C [17]. Although GaN substrates are now commercially available [18], homo epitaxial growth of GaN is not yet that common, which is mainly governed by the cost of GaN substrates. In view of this, an alternate choice of substrate is needed where Sapphire, SiC and Si constitute the major options. Irrespective of large lattice and thermal mismatch with each of the foreign substrates, remarkable developments have already been made [18]. Out of these, Sapphire usually becomes the substrate of choice for the epitaxial growth of GaN layers due to several avdantages compared to other substrates [19].

It is observed that GaN epitaxial layers grown on c-plane sapphire are having a 30° in-plane rotation of the unit cell of GaN about the c axis with respect to the sapphire unit cell [20]. This atomic arrangement is schematically represented in figure 1.1 (a) where the (0001) planes of GaN and sapphire are shown. This leads to about 15 % lattice mismatch between GaN and sapphire [21]. As a result, a large density of threading dislocations originates at the interfacial region between the substrate and the epilayer which propagates all along the growth direction [22]. In general, GaN films contain higher density of dislocations close to the substrate/GaN interface. Some of them terminate within the thick epilayer, while the remaining propagate throughout the film moving towards the film surface. This is schematically shown in figure 1.1 (b). An unintentional n-type doping of GaN occurs due to the incorporation of oxygen (O) and silicon (Si), which act as donor in GaN [23]. Unlike Si, which contributes as a shallow donor, O acts as a localized donor state by substitution on the N site (O_N) of GaN [24]. Carbon incorporated during the growth process acts as a background acceptor level [25].

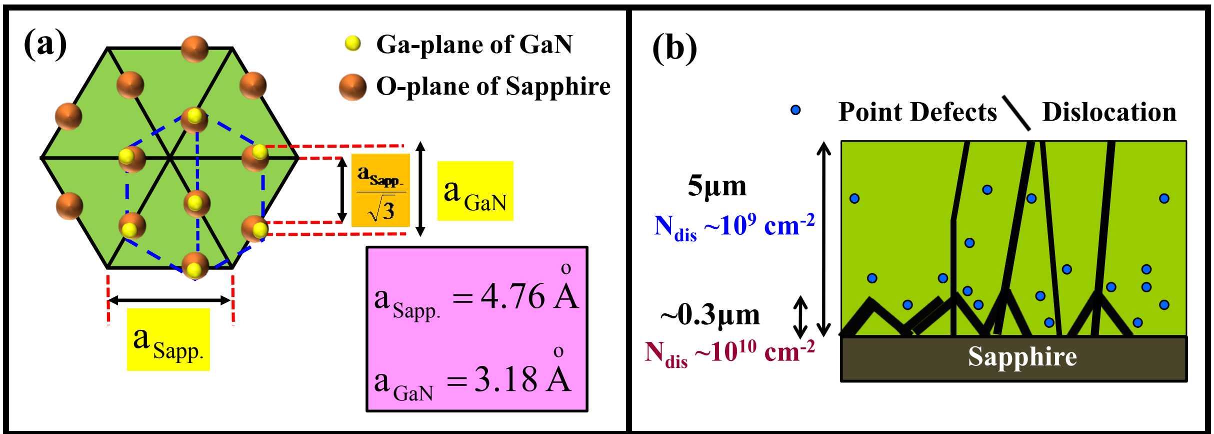

Figure 1.1 (a) Schematic of in-plane atomic arrangement of GaN (0001) grown on sapphire (0001) substrate (b) Schematic cross-sectional view of 5µm thick GaN epitaxial layer grown on sapphire showing typical 0.3 µm interfacial region where dislocation density is typically an order higher than that in the bulk GaN layer.

For intentional n-type doping in GaN, Si (on the Ga site) is the most common choice in different growth methods [26, 27]. Different probable donors and acceptors in GaN are shown schematically in figure 1.2 [22]. Note that the crystal structure close to the GaN/substrate interface is highly defective due to a large density of dislocations which offers a parallel conduction path for the lateral carrier transport [28]. In n-type GaN, these dislocations are negatively charged centres because of the formation of $(V_{Ga}O_2)^-$ complex [22, 29] around the dislocation cores. It is reported that Ga atoms in the dislocation core have high energies, which enhances the probability of V_{Ga} formation [30].

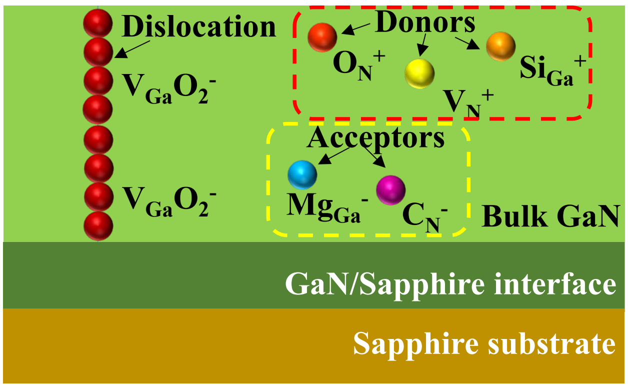

Figure 1.2 Different donors and acceptors present in GaN epilayers [22].

This makes the formation of Ga vacancies (V_{Ga}) energetically favourable at these positions [22, 30]. Since V_{Ga} are triple acceptor (V_{Ga}^{3-}), they form defect complex with oxygen forming $[V_{Ga} O_2]^-$ which act as shallow donor level [30]. The $[V_{Ga} O_2]^-$ complex is highly stable at the dislocation core due to a very low formation energy for the complex. Despite a large density of dislocations and point defects in GaN epilayer, superior performance of GaN UV detectors has been reported by other researchers. For example, a high responsivity of 340 mA/W at 5V bias for GaN photodetectors grown on sapphire substrate with a detectivity (D*) of 1.24×10^{9} Jones and noise equivalent power (NEP) of 2.4×10^{-11} W $Hz^{-1/2}$, which are the key figures of merit for a GaN photodetectors, are already reported. Similarly, a maximum responsivity of 10.5 A W^{-1} at 1V bias, which is the highest among the GaN UV photodetectors on Si substrates along with D* of 2.4×10^{10} Jones is also demonstrated. All such significant developments associated with GaN based photodetectors are discussed in Chapter 5.

Nonetheless, comparing the various unintentionally doped GaN materials, it can be concluded that the MOVPE and HVPE grown GaN samples are having an unintentionally doping level of $\sim1\times 10^{17}$ cm^{-3} which are mostly due to residual Si or high O content in the film as supported by SIMS measurement [31]. Also, the best reported dislocation density in MOVPE and HVPE grown layers are about 10^{8} cm^{-2} [32, 33] which is 1-2 orders of magnitude lower than that for molecular beam epitaxy (MBE) grown GaN epilayers. Moreover, the nature of the various types of defects and the electrical properties of the GaN layer will be largely affected by the respective growth condition of the epi-layer.

1.3 Epitaxial growth techniques of GaN

Conventional crystal growth techniques are not successful for growing bulk GaN crystals due to its high melting temperature and high dissociation pressure. Revolutionary efforts have been made for the bulk growth of GaN [17, 34] leading to the available of GaN substrates. However, an enormous cost of GaN wafers makes them largely unattractive. In view of this, numerous foreign substrates been tried out as discussed earlier. In fact, nearly all the epitaxial growth techniques have been tried to grow high crystalline quality GaN films on various foreign substrates. The three major techniques that are commonly used to grow nitride epitaxial layers are Metal Organic Vapour Phase Epitaxy (MOVPE), Hydride Vapour Phase Epitaxy (HVPE) and Molecular Beam Epitaxy (MBE). Among these, GaN epi-layer grown by MOVPE and HVPE techniques are used in the present study. The two epitaxial techniques are briefly discussed in the next section.

1.3.1 Metal Organic Vapour Phase Epitaxy

MOVPE has become one of the most useful technique for the growth of III/V semiconductors. It offers the promise of large scale production, controllability of thickness of grown layer and formation of abrupt interfaces up to atomic dimension. The fundamental process of MOVPE growth is quite simple. A general overview of MOVPE growth process of III/V semiconductor is schematically shown in figure 1.3. There are four reaction zones as indicated in figure 1.3. In the input zone, the compounds of organometallic molecules like trimethyl-alkyls with Al, Ga, In etc. (R_3III) are injected in to the reactor along with group V hydrides like NH_3. The combination of group III and group V sources are chosen according to the desired III/V semiconductor layer to be grown. First, the gases are injected in such a way that no pre-mixing of group III and V sources occurs prior to the injection zone. Several innovative ways for gas injected have been tried out by the researchers [36, 37], where a showerhead design seems to be the primary choice of MOVPE designers. Next, in the mixing zone, homogeneous gas phase reactions take place leading to adduct formation [35].

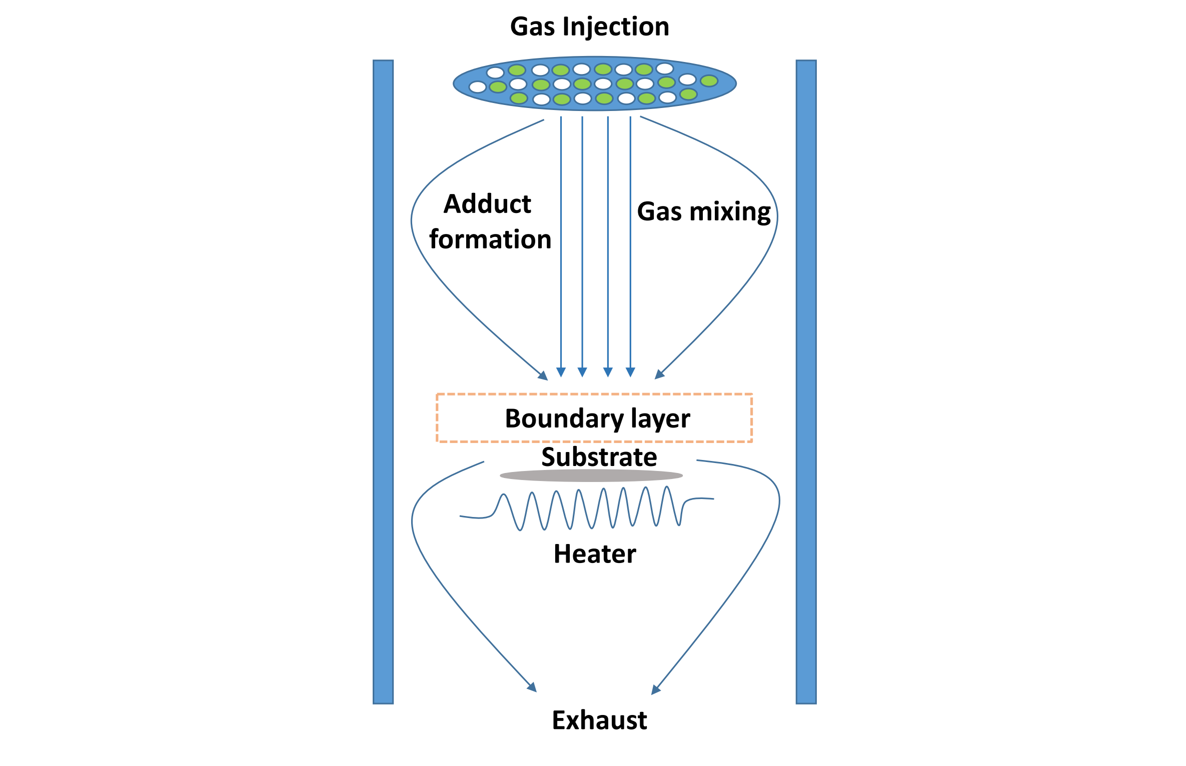

Figure 1.3 Schematic representation of the processes associated with MOVPE growth of III/V semiconductors [35].

In the boundary layer zone, gases become gradually hotter as they diffuse towards the substrate and finally on the substrate surface i.e. growth zone, the actual growth reaction takes place. Considering the growth of GaN using TMGa and NH_3, the overall reaction becomes

$$(CH_3)_3Ga\,(\mathrm{v}) + {}^3\!/_2\,\mathrm{H_2}\,(\mathrm{v}) \rightarrow \mathrm{Ga}\,(\mathrm{v}) + 3\,\mathrm{CH_4}\,(\mathrm{v}) \tag{1.1}$$

which occurs homogeneously in vapour phase (v) and

$$NH_3(\mathrm{v}) \rightarrow {}^1\!/_2\,\mathrm{N_2}\,(\mathrm{v}) + {}^3\!/_2\,\mathrm{H_2}\,(\mathrm{v}) \tag{1.2}$$

which occurs at the solid-vapour interface and

$$Ga\,(\mathrm{v}) + {}^1\!/_2\,\mathrm{N_2}\,(\mathrm{v}) \rightarrow Ga\mathrm{N}\,(\mathrm{s}) \tag{1.3}$$

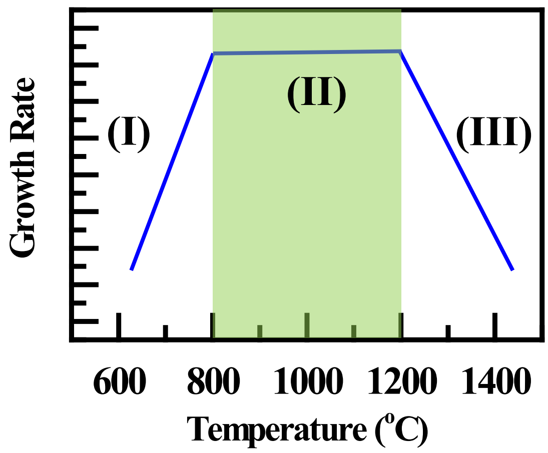

Figure 1.4 Temperature dependence of GaN growth rate in MOVPE process [38].

From the study of growth rate of GaN by several researchers with TMGa / NH_3 as the III/V sources in large temperature range 600°-1400° C, three distinct temperature dependant regions of growth are identified and are schematically represented in figure 1.4. It can be seen from the figure that the growth rate is temperature independent over a wide temperature range from 800 to 1200 °C (region II). High growth temperature greater than 800 °C is required to achieve single crystalline GaN epilayers of good quality. In general, GaN epilayers with the superior optoelectronic properties are grown in the temperature range 1000 -1100 °C. Growth in this region is limited by the mass transport. In MOVPE process, the growth rate is independent of NH_3 flow rate since V/III ratio often exceeds few thousands. The growth rate has a linear dependence on the TMGa flow rate as expected in the mass transport limited growth. At low temperature (region I), the growth rate begins to decrease with decrease in growth temperature. The atoms don't have sufficient energy required to attain minimum energy position. Hence, the good quality epitaxial layers can't be grown in this temperature range. In region III, the growth rate again start decreasing above growth temperature of 1200 °C. When temperature greater than 1200 °C is used, the dissociation of GaN results in voids formation in the grown layer. Though the mechanism is not clearly known, the possible reasons are desorption of group V sources (NH_3) before incorporation, desorption of Ga and also the parasitic reaction in the chamber forming (- RIII–VR$^{/}$ -) complex that deposits on the reactor wall resulting in lower growth rate.

Overall, MOVPE is an excellent method for growing epitaxial GaN films with typical growth rate less than 10 μm/hr. It allows rapid switching between group III precursors which makes it ideal for growing alloy layers of different compositions for device structure growth. However, relatively slow growth rate, and high cost of precursor materials makes it less attractive for the growth of very thick GaN layers, where HVPE is usually preferred.

1.3.2 Hydride Vapour Phase Epitaxy

HVPE is an early technique used back in 1960's for growing GaN epitaxial layers [6, 39]. It is the most suitable method for the growth of thick GaN layers preferably for commercial applications even till date. In this process, metal atoms are transported to the substrate from a reservoir of pure metal and reacted with HCl at 800-900°C, forming a volatile gas-phase metal chloride:

$$\mathrm{Ga}_{\,\text{liquid}} + \mathrm{HCl} \rightarrow G\mathrm{aCl} + \tfrac{1}{2}\mathrm{H}_2 \tag{1.4}$$

Note that by depending on chamber design, reservoir temperature, gas flow rate and residence time, the above reaction may be partially incomplete resulting in an excess of HCl in the GaCl gas stream. The volatile metal compound is then transported to the substrate zone by the carrier gas where the deposition reaction occurs:

$$\mathrm{Ga\,Cl} + \mathrm{NH}_3 \rightarrow G\mathrm{aN} + \mathrm{HCl} + \tfrac{1}{2}\mathrm{H}_2 \tag{1.5}$$

Moreover, above a critical temperature of about 1200 ºC, the growth of GaN becomes thermodynamically unfavourable which results in etching rather than deposition. Note that HCl and H_2 are formed as a product of deposition reaction which are reactive and can etch GaN to produce GaCl and N_2 as given below,

$$HCl + GaN \rightarrow GaCl + \tfrac{1}{2} N_2 + \tfrac{1}{2} H_2 \tag{1.6}$$

HCl either from the deposition end product or from an incomplete GaCl production reaction, can chemically attack the GaN film during growth. Such etching are often preferential with higher etch rates in the strained regions resulting in a textured surface or rough film morphology forming hexagonal shaped hillocks and pyramids. In this context, the end product methane of MOVPE growth of GaN is not that destructive, since it does not interact with the reactor wall, substrate or GaN film. However, HVPE is particularly suitable for commercial growth of GaN epitaxial layers due to its higher growth rate of 10-100 µm/ hr. [28, 40]. Due to the usage of HCl to transport Ga, the chances of carbon incorporation in the growing film becomes considerably low which is an important advantage of HVPE technique. Also a lower cost and availability of high purity precursors make HVPE a superior choice for growing thick GaN epilayers. However, HVPE is not preferable for compositional changes during the growth like MOVPE. This is because GaCl is formed only after HCl flow is initiated and will continue for certain duration even after HCl flow is terminated making it difficult to form abrupt interfaces. Choosing substrates for growing GaN films by HVPE is more constrained compared to MOVPE. It is necessary to ensure that the substrate to be used for the growth should not react with HCl. This is the reason why Silicon, the most preferred substrate in semiconductor industry can't be used in HVPE growth of GaN since both HCl and GaCl readily reacts with Si, forming volatile SiC and gaseous H_2 or liquid Ga as by-products. More stable substrates like SiC and sapphire which are not attacked by HCl or GaCl are the better candidates for the epitaxial growth of GaN by HVPE technique.

1.4 GaN based UV photodetectors

GaN is one of the most technically viable solutions for the UV photo detection when considered among all other semiconductor materials available for such applications. Though the research in GaN based UV detector began more than 30 years ago [41], development of good quality GaN epitaxial layers for such applications have been delayed for several decades due to the absence of lattice matched substrates. Although major thrust behind the research work on III nitride semiconductors had been made for the realization of blue light emitting diodes, lasers, and power electronic devices, these technological advancements have also led to a significant progress in the domain of GaN based UV detectors. Nitrides are often preferred for UV detection applications in the field of UV astronomy, flame detection, furnace control, water purification, UV radiation dosimetry, and military applications etc. [2, 3]. Based on the working principle, GaN based photodetectors can be classified in two categories, photoconductive and photovoltaic ones. Schematic device structures of these photodetectors are shown in figure 1.5.

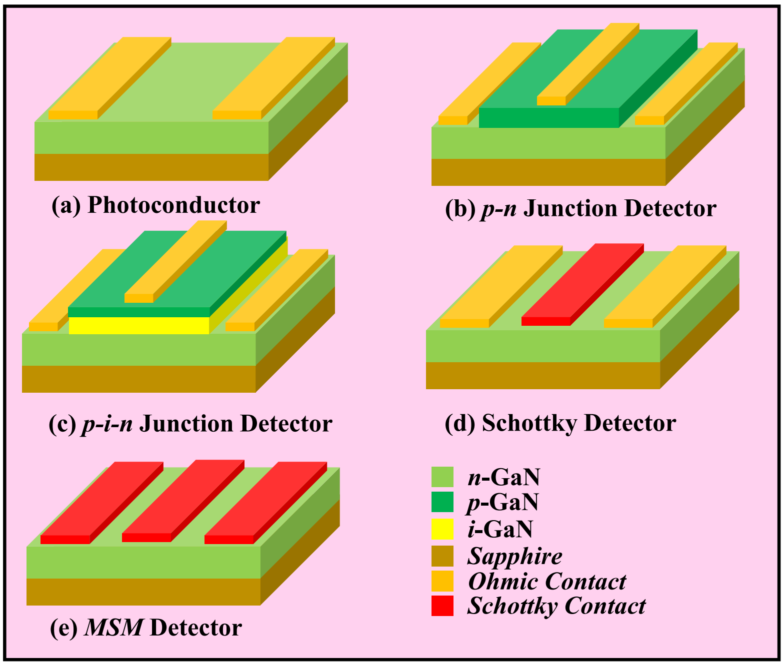

Figure 1.5 Schematic structure of different photoconductive and photovoltaic detectors.

In case of photoconductive detectors, no photoresponse is recorded in absence of bias whereas a measurable response can be observed in photovoltaic detectors even without any external bias. In case of photovoltaic detectors, usually the magnitude of signal can be further enhanced by application of external bias. A particular type of photodetector configuration is chosen as per the requirement of a specific application.

1.4.1 Photoconductive detectors

Photoconductive detectors, also known as photoconductors are the light detectors which work on the principle of photoconductive effect. It requires a piece of semiconductor material having two Ohmic contacts to make a photoconductive UV detector, as shown in figure 1.5 (a). The operation of a photoconductor is shown in figure 1.6. Absorption of light photon with energy (hυ) higher than the band-gap (Eg) of the semiconductor leads to generation of an electron-hole pair which changes the electrical conductivity of the semiconductor. For doped semiconductor with low resistivity, the device is usually operated in a constant current mode as shown in figure 1.6. Here the signal appears as a change in voltage developed across the sample after light exposure.

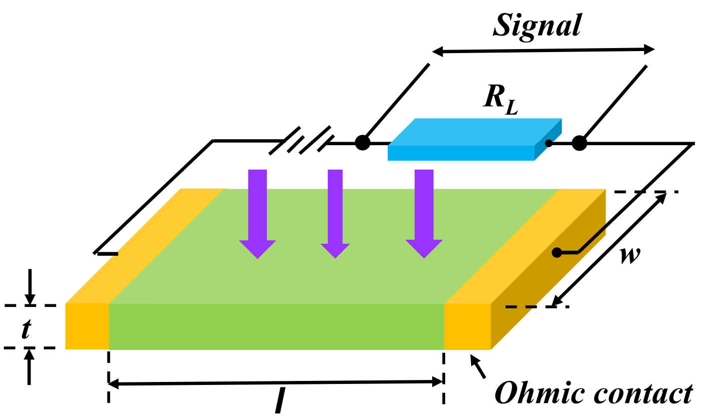

Figure 1.6 Schematic diagram to illustrate the operation of a photoconductive detector.

However, in constant voltage mode for high resistive samples, the signal is detected as a change in current in the external circuit. The basic expression for photoconductivity in semiconductors under equilibrium photo excitation is $I_{ph} = q\,\eta\,A\,\Phi_S\,g$, where Φ_S is defined as the photon flux density incident on the detector with area A, and the quantum efficiency (η) defines the number of electron-hole pair generated per incident photon. The photoconductive gain (g) on the other hand denotes the number of carriers reaching the electrodes due to one pair of carriers generated under photo illumination. It can be expressed as;

$$g = \tau / \mathbf{t_r}\ , \text{ where } \mathbf{t_r} = \ell / \mathbf{v}_d = \ell^2 / \mu_e \mathbf{V_b} \tag{1.7}$$

Here, 'τ' is the excess carrier lifetime and 't_r' is the electron transit time between the Ohmic contacts, 'ℓ' is the spacing between the electrodes, 'v_d' is the carrier drift velocity, 'μ_e' is the mobility and 'V_b' is the applied bias. The value of 'g' can be lower or greater than unity depending upon the value of product '$v_d \times \tau$' with respect to 'ℓ'.

The first high performance GaN photoconductive detector was reported by Khan *et al.* [42] where the active region was about 1 μm thick insulating GaN film grown by MOVPE on sapphire substrate. The device showed a peak response of 10^3 A/W at 365 nm. Photoconductive UV detectors have simple device structures, easy fabrication process and also show a high internal gain. However, slow response and large dark current are their primary limitations.

1.4.2 Photovoltaic detectors

Photovoltaic detectors contain a built-in space charge region which enables their operation even in the absence of applied bias. Such detectors are of several types like p-n junction, and p-i-n junction detectors, Schottky barrier detectors, MSM etc. and are briefly described as follows;

1.4.2.1 P-N and P-I-N junction photodetectors

In photovoltaic detectors, basic photo detection principle is the collection of photo generated charge carriers across a built-in electric field. The charge carriers of opposite sign are swept out in opposite directions due to the built-in electric field resulting a current flow in the circuit. The typical photovoltaic detectors are p-n or p-i-n junction diode which is illustrated schematically in figure 1.5 (b-c). When photons with energy greater than the bandgap of semiconductor are incident on the active region of device, electron-hole pairs are generated in the depletion region. The electrons and holes generated in the space charge region are swept out by the strong electric field at the p-n junction, generating a photo current. Carriers generated within the diffusion length from the junction also contribute in the photocurrent. Since the detector works in reverse bias mode, major change in the current–voltage characteristic will be noticed only in the third quadrant as shown in figure 1.7. Generally, the current gain in a photovoltaic detector like p-n junction is unity. This leads to the expression of photocurrent (I_{ph}) to be $I_{ph} = \mathbf{q}\,\eta\,\mathbf{A}\,\Phi_S$. The dark current in a p-n junction photodiode is mainly governed by the diffusion current. It is consisted of electrons (holes) injected from the n (p) side of the device to the opposite side of the junction. However, in a practical device, several other mechanisms additionally contributes in the overall dark current of device [2]. These are (1) current due to generation–recombination process in the depletion region, band-to-band, trap-to-band and inter trap carrier tunnelling etc. and (2) surface leakage current from the surface states. Some of the mechanisms are schematically shown in figure 1.8. Note that each component has its own individual dependence on applied bias and temperature.

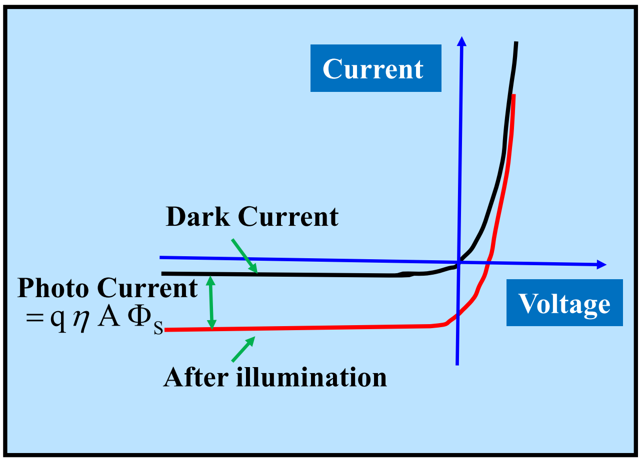

Figure 1.7 Typical current–voltage characteristics of a p-n junction before and after light illumination.

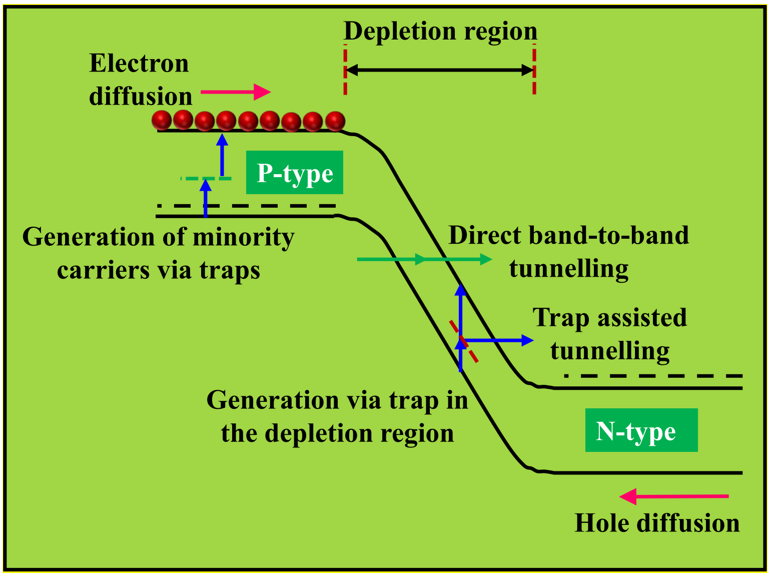

Figure 1.8 Schematic illustration showing key processes which govern the dark current in a p-n junction based photodetector under reverse bias [2].

Photosensitivity and response time of the device can be improved further by inserting an intrinsic (i-layer) layer in between the p and n layers which increases the width of the depletion layer, as shown in figure 1.5 (c). Generally, p-i-n detectors work under either the absence or presence of reverse bias such that the maximum photo current signal can be collected which improves device sensitivity. Further, a high reverse bias widens the depletion width and reduces the junction capacitance. This will not only increase the responsivity of the detector but also enhance response speed of the device [2]. In past, GaN based p-n junction detectors were successfully demonstrated by Chen *et al*. [43]. They had fabricated two types of GaN p-n junction detectors by MOVPE, where 0.5-μm-thick Mg-doped p-GaN (n-GaN) layer was grown on 1-μm-thick unintentionally doped n-GaN (p-GaN) layer. A peak responsivity of 0.09 A/W was achieved in those detectors which is comparable to that of UV enhanced Si PDs. However the response time of those devices was found to be considerably slow, typically of the order of ~ 0.4 ms. In past, many attempts have been made to improve the responsivity and speed of GaN PDs [44, 45].

1.4.2.2 Schottky barrier photodetectors

Schottky barrier photodiodes have been extensively studied and are widely used in semiconductor based UV detectors. A relatively simple fabrication technology, high response speed and capability of operation under zero bias make them attractive for many applications. Schottky contacts to n-type (p-type) semiconductors can be formed by selecting a metal having work function (ϕ_m) larger (smaller) than the work function of semiconductor (ϕ_s) [46]. The energy level diagram of a metal/semiconductor Schottky contact before and after the contact formation is shown in figure 1.9. In figure 1.9 (a), the metal semiconductor junction is not formed and hence the system is not in thermal equilibrium. When the metal and the semiconductor are joined then electron flows from semiconductor to metal since $\phi_m > \phi_s$. This will lead to the realignment of Fermi levels in metal and semiconductor such that it become a constant level throughout the entire diagram as shown in figure 1.9 (b). The ionized donors create a region of positive charges within semiconductor layer near the interface which is called the space charge region or depletion region.

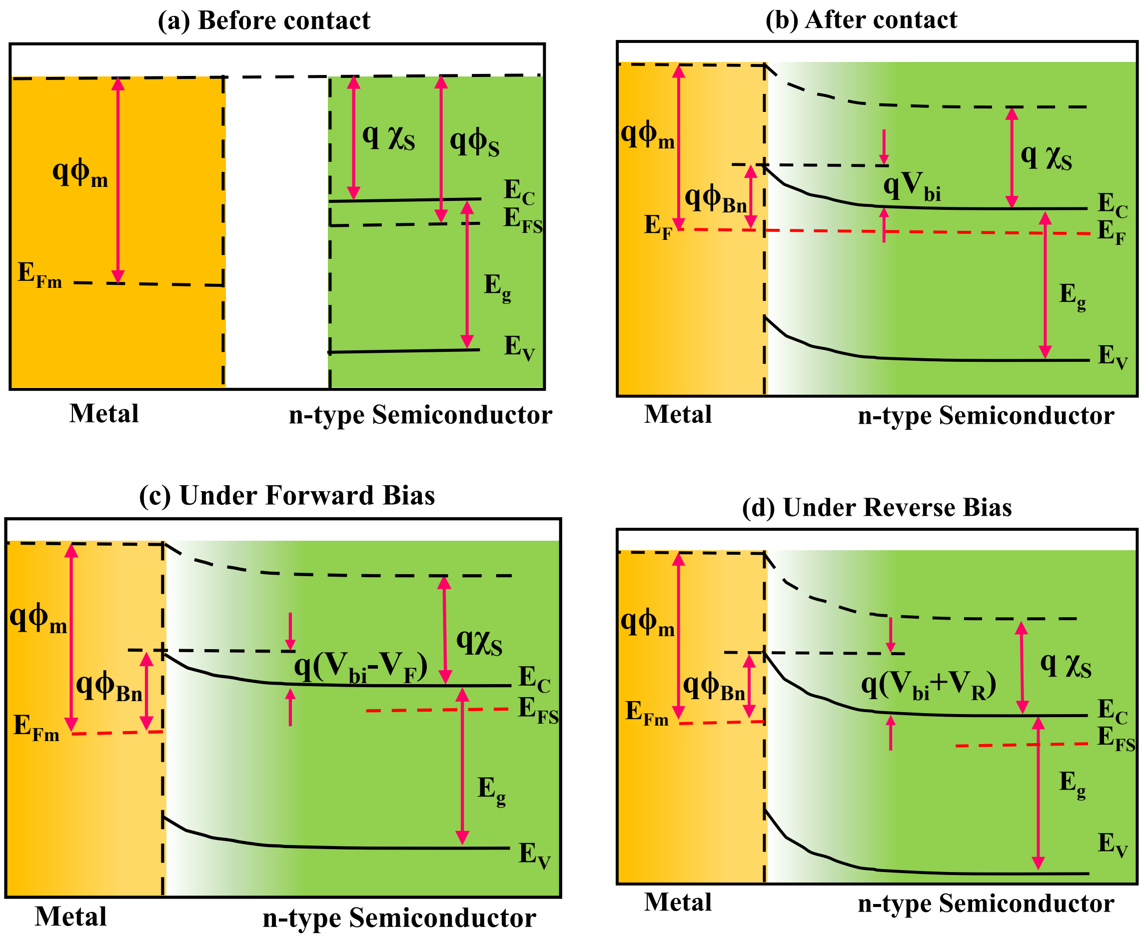

Figure 1.9 Energy band diagram for metal/n-type semiconductor Schottky junction with $\phi_m > \phi_s$ for (a) before contact (b) after contact, under (c) forward bias and (d) reverse bias.

After junction formation, electrons flowing out of the semiconductor to metal encounters a potential barrier, which is the property of any rectifying junction. Expression for the barrier height, $q\phi_{Bn}$, of the contact for an n-type semiconductor is given by,

$$q\phi_{Bn} = q\left(\phi_m - \chi_S\right) \tag{1.8}$$

This is the barrier faced by electrons in metal side while trying to move into the semiconductor layer. On the other hand, V_{bi} is the barrier faced by electrons in the conduction band of semiconductor while trying to move into the metal and is called the built-in potential barrier. When a forward bias (V_F) is applied, semiconductor to metal barrier is reduced, while ϕ_{Bn}

remains essentially constant as shown in figure 1.9 (c). As a result, electrons can easily move from semiconductor to the metal side. On the other hand, applying a reverse bias (V_R) to metal with respect to semiconductor results in an increase in semiconductor to metal barrier, thus making it difficult for the electrons to flow from semiconductor to metal as shown in figure 1.9 (d). It is known that a high barrier will provide lower leakage current and better device performance. In past, Chen *et al.* [47] had reported vertical geometry Schottky barrier UV detectors based on n-GaN/Sapphire. Peak responsivity of 0.18 A/W and decay time of 118 ns was reported by them. Similarly Katz *et al*. [48] had compared the performance of vertical and lateral geometry Schottky detectors and found that vertical detector exhibits two orders higher responsivity due to the reduced effect of dislocations in carrier transport.

1.4.2.3 Metal-semiconductor-metal photodetectors

Among various photovoltaic photodiodes, GaN Metal-Semiconductor-Metal (MSM) PDs have emerged as one of the most successful and popular device structure owing to its fabrication simplicity, high operation speed and easy integration with field-effect-transistor (FET)-based electronics. In the present work, several GaN detectors are fabricated in MSM geometry. The MSM structure was chosen for the following reasons; a low hole mobility of GaN implies that the distance between the two electrodes must be relatively small. This is possible in MSM geometry where holes can be collected quickly. Ideally the separation between the contacts can be reduced down to the order of hole drift length. This not only reduces the collection time of photo generated carriers but also reduces the probability of charge trapping before their collections at the electrodes. Though the electrodes are kept reasonably close, MSM finger geometry ensures that the active region of the device is not significantly compromised. MSM PDs are consisted of two interdigitated Schottky barriers connected back to back. The energy band diagram of such PDs under thermal equilibrium is shown in figure 1.10 (a), where ϕ_{Bn1} and ϕ_{Bn2} are the barrier heights of the two metal-semiconductor contacts. With a condition of $\phi_{Bn1} \cong \phi_{Bn2}$, an MSM device is symmetrical. Under an applied bias, one of the junction is always reverse biased (here junction 1) while the other one is forward biased (here junction 2) as shown in figure 1.10 (b). As a result, the space charge region under the junction 1 will increase and that under the junction 2 will decrease. Since, electrons will flow from the reverse to the forward junction, they will face a barrier ϕ_{Bn1}. As a result, the dark current will be negligible. When the MSM detector is illuminated with UV light, then the photo generated electrons drift in the conduction band towards the forward biased junction 2, which is positively biased and the holes drift towards the reverse biased junction 1, which is negatively biased.

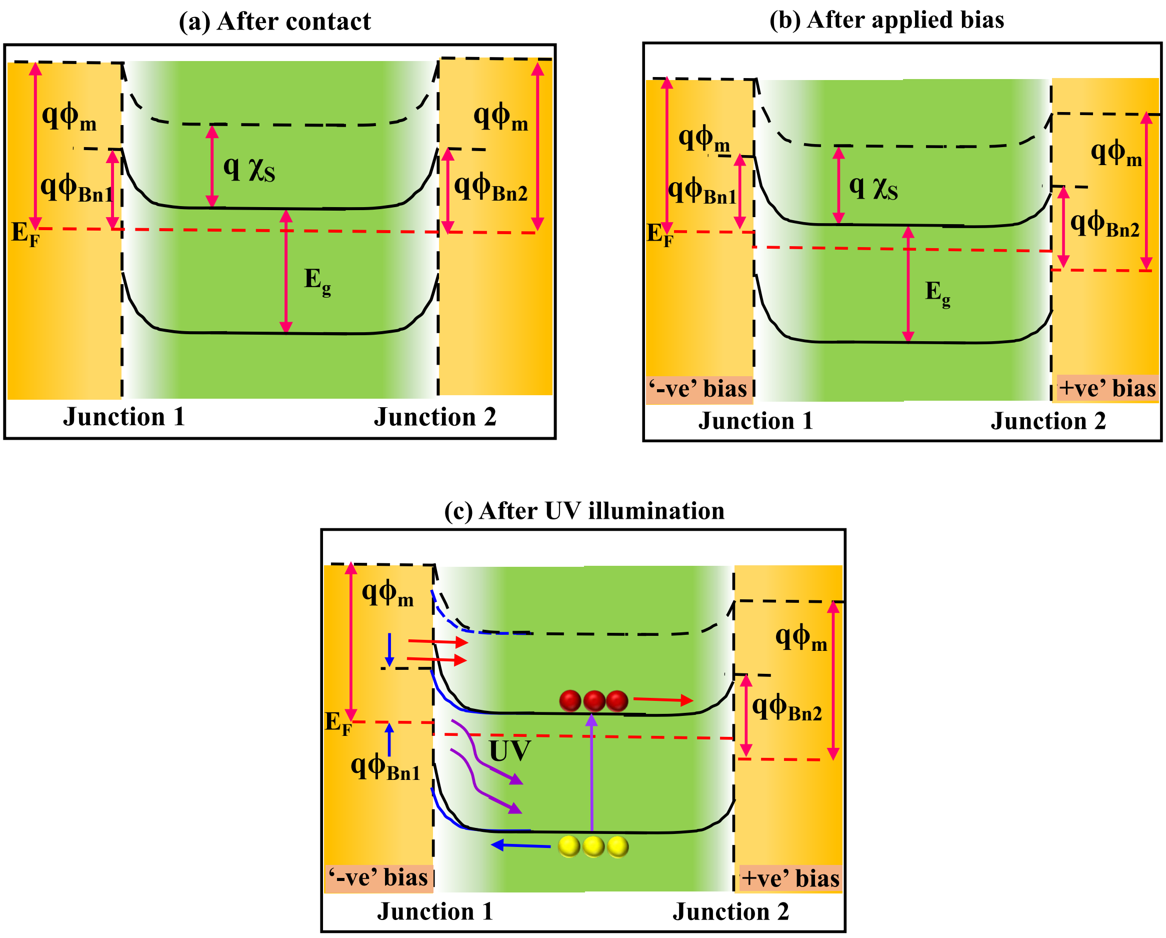

Figure 1.10 Energy band diagram of GaN MSM detector for (a) without applied bias and (b) with applied bias in dark conditions and (c) upon UV illumination.

In presence of hole trapping centres at metal-semiconductor interface, holes might get trapped at junction 1. This will lead to a Schottky barrier lowering and an enhanced current flow across the junction1 leading to an enhancement in the photocurrent as shown in figure 1.10 (c).

In past, high performance GaN MSM detectors were reported by Walker *et. al*. [49] where the interdigitated fingers were made. Those detectors were fabricated on MOVPE grown unintentionally doped GaN and had showed a fast response with response speed < 10 ns. Recently, several large area MSM detectors have been reported with response time varying from 3-60 ms. These devices are grown on unintentionally doped GaN epi-layers [50, 51].

1.5 Current transport mechanisms in GaN Schottky detectors

In presence of threading dislocations and interfacial trap states, there are several current transport mechanisms actively participating in in GaN Schottky photodiodes. The role of a particular conduction mechanism depends on temperature, background dopant density, and the density of interface states. Devices based on metal-semiconductor junctions are majority carrier device whereas those based on p-n junctions are minority carrier devices.

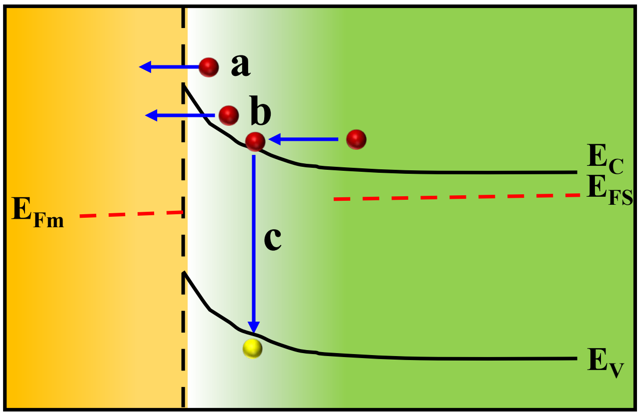

Figure 1.11 Possible carrier transport processes in forward-biased Schottky diode fabricated on an n-type semiconductor.

The different possible ways by which current can be transported under forward bias across a Schottky junction is shown in figure 1.11. These processes are [52], (a) thermionic emission of electron from semiconductor to metal where carriers are able to cross the barrier with the help of thermal energy, (b) thermionic field emission mediate by quantum mechanical tunnelling of electrons, and (c) recombination of carriers in the depletion region. Note that the inverse of these processes also occur under reverse bias.

1.5.1 Thermionic emission mechanism

The thermionic emission (TE) theory proposed by Bethe [53] is the ideal current transport mechanism across metal-semiconductor junction. In TE mechanism, the current is governed by the emission of electrons over the barrier from semiconductor (metal) to metal (semiconductor) under forward (reverse) bias, as indicated by process ‘a’ in figure 1.11. The theory is based on the assumptions that (1) the barrier height q ϕ_{Bn} is much larger than the thermal energy kT, (2) thermal equilibrium is established at the interfacial plane that determines emission, and (3) the equilibrium is not affected by the existence of a net current flow across the junction due to two current fluxes – one from the semiconductor to metal while the other from metal to semiconductor. Since the assumptions are based on the current flow across the metal-semiconductor interface, the shape of barrier profile has no further significance and current flow solely depends on the barrier height. Devices where TE is the dominant current transport process show high responsivity and low leakage current. This normally happens when a high barrier height is achieved via proper selection of metal-semiconductor combination which minimizes the possibility of carrier tunnelling across the junction, thus leaving TE as the most dominant current transport mechanism.

1.5.2 Thermionic field emission mechanism

In most of GaN UV photodetectors, it is found that the I-V characteristics are distinctly different from the theoretically predicted curves based on ideal TE transport model. The magnitude of leakage current is generally found to be much larger than that predicted by TE model. The leakage current also strongly depends on the applied bias and surface treatment which can't be explained by the TE model. Thermionic field emission (TFE) mediated by carrier tunnelling is an obvious alternate choice in such devices as discussed in detail by Padvani and Stratton [54]. In the TFE model, forward bias current transport in the intermediate bias range is dominated by the tunnelling of thermally excited electrons. The tunnelling probability for such a process increases exponentially with the energy since electrons near the tip of the potential profile see a lower and thinner barrier as shown in figure 1.12. On the other hand, the number of such thermally excited electrons fall exponentially at high energy. Eventually, the energy distribution of carriers that contribute in TFE is narrowly peaked, as schematically shown in figure 1.12.

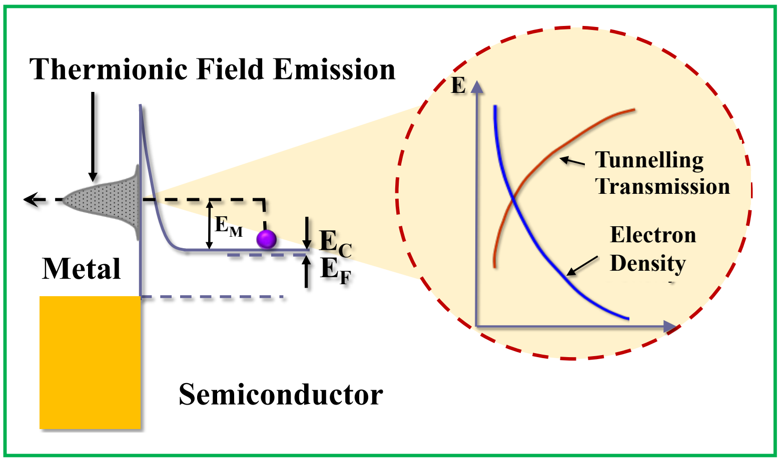

Figure 1.12 Schematic diagram of the TFE process under forward bias; the inset shows the variation of tunnelling probability and electron density as a function of energy where their product gives a sharply peaked energy profile of electrons that can transmit through the potential barrier.

The tunnelling process therefore effectively reduces the height of Schottky barrier under TFE mechanism. The amount of barrier lowering under the tunnelling process depends on the dopant density and temperature. At very low temperature and for heavily doped semiconductors, carrier tunnelling can eventually take place at the Fermi level, leading to the so-called Field Emission (FE) process.

1.5.3 Generation–recombination current

The current transport across an ideal metal/semiconductor Schottky junction is based on the assumption that there is no generation and recombination current in the depletion layer, and electron/hole current is constant throughout the depletion region. However, in practical diodes, none of the above approximations are valid. The main reason behind the deviation is the presence of foreign atoms or crystal defects that give rise to localized energy levels in the band gap which enhances the G-R current in the depletion region. The reverse bias G-R current can be expressed as [2],

$$\mathbf{I_{G\text{-}R} = q\, G_{dep}\, V_{dep}} \tag{1.9}$$

where G_{dep} and V_{dep} are the generation rate and the volume of the depletion region. Further, the generation rate for a mid-gap state can be expressed by considering the Shockley-Read– Hall formula as $G_{dep} = n_i / \tau_0$, where n_i is the intrinsic carrier density and τ_0 is the life time of the majority carrier. Then, the G-R current density in the depletion region can be written as,

$$I_{G\text{-}R} = qA\, n_i\, w_{dep.} / \tau_0 \tag{1.10}$$

As can be seen from equation 1.10, the G-R current is proportional to n_i for a mid-gap state. Also, the $I_{G\text{-}R}$ roughly varies as the square root of the applied bias since $w_{dep.} \propto \sqrt{V}$.

1.6 GaN as radiation hard detector

GaN-based devices are more radiation tolerant compared to Si and GaAs-based devices due to high displacement energy, which is inversely proportional to the lattice constant [55]. The high displacement energy for GaN implies that it will be more resistant to the creation of point defects during irradiation. For example, McPherson *et al.* showed that in case of Si detector, the leakage current increases from 1 nA to 30 μA at 3V applied bias when irradiated by 1 MeV neutrons with fluence of 3×10^{13} n/cm^2 [56]. On the other hand, negligible change in leakage current is reported by Lin *et al.* after irradiation with neutrons of same energy and much higher fluence of 10^{15} n/cm^2 [57]. This clearly demonstrates that GaN detectors are more resistant to radiation damage than silicon. Such radiation hardness of GaN makes it a suitable candidate for applications in harsh radiation environments like nuclear reactors, particle accelerators, and spacecraft. Moreover, a clear understanding of high-energy irradiation induced defects in GaN is necessary for estimating the long-term reliability of GaN based optoelectronic devices in a harsh radiation environment. In general, electron and proton irradiation generates point defects in the nitride lattice [58, 59], whereas response to the gamma irradiation is quite complex. Gamma irradiation generates secondary electrons via Compton scattering which in turn creates electron-hole pair in GaN. On the other hand, Look *et al.* showed that the high energy (0.7-1 MeV) electron irradiation creates V_N and interstitial N_I which behave as donor and acceptor levels [60]. This changes the occupancy of the trap levels present in the material before irradiation and even forms new impurity complex. Exposure of GaN semiconducting layers to high energy radiation leads to the creation of vacancy and interstitial point-defects through the displacement of Ga and N atoms from their respective lattice sites. It introduces new energy levels in the forbidden gap which act as scattering centres and can be donor, acceptor, or recombination centres. Hence, the radiation induced defects significantly influence the electrical transport and optical properties of device material and subsequently the performance of semiconductor device [55, 60, 61]. However, it is also observed that the unstable lattice damages caused by the incoming radiation were removed at room temperature within few days after the irradiation by self-annealing process [62]. These results suggest that GaN has an intrinsically high tolerance against radiation-induced damage in comparison to conventional semiconductor like Si, Ge and GaAs etc.

In this thesis, electrical transport in GaN epitaxial layers is studied with an aim of the fabrication of high performance GaN based UV PDs for potential application in high radiation environment. In **chapter 2**, an introduction of the various experimental techniques that are used during the course of this thesis work for the epitaxial growth of GaN, fabrication and characterization of GaN PDs is given. Results on the epitaxial growth of GaN in indigenously developed MOVPE system are presented in this chapter. It is found that the background carrier concentration of GaN epilayers is quite large which makes them unsuitable for detector applications. In view of this, good quality GaN epilayers grown by the two commonly used techniques i.e. HVPE and MOVPE are procured from commercial sources and the subsequent work in the thesis is carried out on these samples. In **chapter 3**, in-depth electronic transport measurements are performed on commercially procured GaN samples where current transport in HVPE GaN layers is found to be severely affected by parallel conduction. MOVPE GaN samples seems to be better in this aspect and are therefore thought to be a better choice for device fabrication. In **chapter 4**, fabrication of metal-semiconductor-metal (MSM) GaN photodetectors is presented on both types of GaN samples where HVPE GaN turns out to be better. Fundamental reasons behind this observations are investigated and are summarized in this chapter. In **chapter 5**, a method to enhance the detector performance with the insertion of a thin layer of ZrO_2 in metal-oxide-semiconductor (MOS) geometry is demonstrated where excellent device characteristics are recorded. Next, the role of dry etching in the fabrication of GaN PIN detector under vertical geometry is discussed in **chapter 6**, where a method to recover the etching induce damage is also demonstrated by using post etch O_2 plasma treatment. In **chapter 7**, importance of GaN UV detectors for possible applications in harsh radiation environment is demonstrated by exposing few devices to a high dose of ^{60}Co gamma rays. In **chapter 8**, the important results of present thesis are summarized.

Chapter 2

Experimental Techniques: MOVPE Growth, Characterization, Device Fabrication and Testing

2.1 Introduction

After an overview of the fundamental physics issues related to GaN semiconductor technology, the next step is to discuss the experimental techniques related to epitaxial growth, layer characterization, device fabrication and testing. To begin with, a brief introduction of the growth of GaN epitaxial layers in an indigenously developed nitride MOVPE system is discussed in brief. It is then followed by the discussion on high resolution X-ray diffraction technique which is a powerful non-destructive method for determining the crystal structure, lattice constant, strain, and defect density of GaN epitaxial layers. Electrical characterization techniques including temperature dependent Hall, current voltage and capacitance voltage profiling are described afterwards. The next section is dedicated to optical characterization techniques like photoluminescence measurements on GaN epitaxial layers and also the techniques to measure the operational characteristics of UV photodetectors. It is then followed by the discussion on device fabrication techniques including photolithography, metallization, oxide passivation, and rapid thermal annealing which are used to fabricate GaN based UV photodetectors as part of this thesis. Dry etching process, which is a critical device fabrication step in nitrides, is given a special attention. Finally, the chapter ends with a brief discussion of secondary ions mass spectroscopy technique, which is essential for determining the depth profile of impurities present in GaN epilayers.

2.2 MOVPE growth of GaN epitaxial layers

MOVPE is one of the most preferable technique for growing good quality GaN epi-layer and heterostructures. Several critical issues related to the MOVPE growth of GaN epitaxial layers are now well understood, however in reality a lot more is yet to be learnt. Even for the state-of-the-art MOVPE reactors, most of the growth parameters are mandatory to be fine-tuned before the desired layer quality is achieved. Most often the set of growth parameters is specific to a particular reactor design/geometry and the growth recipes cannot be easily transferred from one reactor to another. Moreover, such MOVPE reactors are extremely expensive and are beyond the reach of common researchers. It therefore provide scope for the development of a simple MOVPE reactor which is affordable and can deliver the layers of desired quality. Keeping this in mind, an indigenous MOVPE system is developed in our lab and the same system is used to optimize the quality of GaN epitaxial layers as part of this thesis. Some important details of the indigenous MOVPE system are as follows [63];

A schematic diagram of indigenously developed nitride MOVPE system is shown in figure 2.1. Standard precursors like tri-methyl Gallium (TMGa), tri-methyl Aluminium (TMAl), tri-methyl Indium (TMIn), and Ammonia are adopted for the growth of GaN. For the doping purposes, diluted Silane (2% in Hydrogen) is also included. As shown in figure 2.1, Nitride MOVPE system can be divided into the following sub-systems:

1. Gas supply and Mixing System (GMS) including the gas cabinets
2. Stainless steel reactor with a gas injection shower head and a heater (~1100 ^{o}C)
3. Vacuum system
4. Scrubber unit
5. Ventilation system

6. Control circuitry including computer control of the entire MOVPE system

Photographs of the developed nitride MOVPE system, GMS unit and the MOVPE reactor are shown in figure 2.2. Fabrication of the system was carried out under a clean tent of class 100 specifications in order to avoid any contamination during the fabrication. GMS of nitride MOVPE provides the various precursors in desired proportions and sequence to the MOVPE reactor depending on the requirement of a particular semiconductor material to be grown.

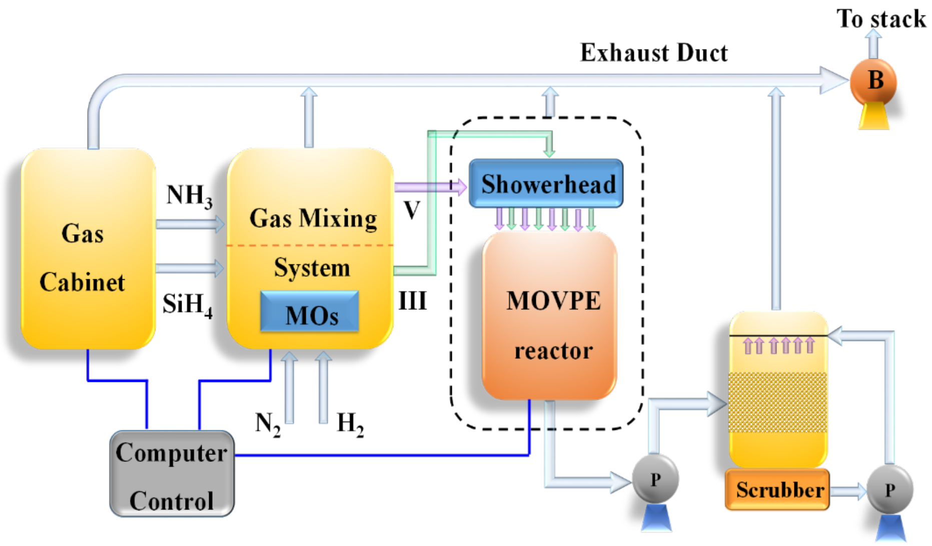

Figure 2.1 Schematic diagram of indigenously developed nitride MOVPE system.

Figure 2.2 Real photographs of **(a)** indigenously developed nitride MOVPE system, (b) gas mixing system, and **(c)** MOVPE reactor.

It is an ultra-high purity (UHP) gas handling system where all the components are carefully selected to ensure their compatibility with UHP gases. No impurities shall be generated in these components. Further, a very high leak tightness is mandatory due to the corrosive and toxic nature of precursors. It is also required for minimizing the impurity incorporation in the grown layer. An indigenously designed shower head of 2-inch diameter is used to feed the gaseous precursors to the nitride MOVPE reactor. Another important concept in MOVPE reactor design is related to the uniform mixing and laminar flow of gases. Recirculation of gases inside the MOVPE reactor needs to be minimized in order to avoid memory effects and also to minimize the resident time of un-reacted precursors. The vertical reactor geometry with gas injection from the top and exhaust port at the bottom helps in maintaining a streamline flow of gaseous precursors. Since the showerhead is mounted on the top flange of the reactor, the buoyancy induced recirculation of gases can be minimized by varying the total gas flow in the reactor up to certain extent. In our design, Hydrogen (H_2) and Nitrogen (N_2) are used as the carrier and purge gases respectively. It is ensured that the purity of H_2 and N_2 gases is of the order of 99.999 % (5N pure). However, in order to grow epilayer of excellent crystalline quality, much higher purity (≥7N pure) is required. This is achieved by using getter based purifiers in the indigenously developed MOVPE system. Ultra-high purity H_2 gas is therefore used to transport the MO precursors into the reactor. For achieving high temperature required for the growth of GaN, an indigenously designed high temperature resistive heater capable of reaching 1100 ^{o}C is also included. The heater and substrate holder are made of high purity Molybdenum metal. Diameter of substrate holder and heater is kept 40 and 35 mm respectively. The substrate holder is kept 2 mm above the heating element. Growth temperature is measured by a K-type thermocouple which is fixed 2 mm below the moly heater. In the present configuration, no provision is currently available for the measurement of surface temperature of the wafer. Therefore, the temperature measured by the thermocouple could be slightly different than the actual surface temperature. However, substrate temperature being one of the parameters to be optimized during MOVPE growth, a small difference in the two values will not affect the final outcome significantly. The substrate holder can carry wafers of 1" square size. The gap between the surface of wafer holder and showerhead is kept about 5 cm.

Safety is a key criteria for the design of an of MOVPE system. Note that the threshold limit value (TLV) of NH_3 is only 25 ppm while H_2 being a highly inflammable gas carries a low explosive limit (LEL) of only 4%. It therefore requires that the necessary safety issues are carefully considered. The first and foremost requirement is to ensure the leak integrity of overall MOVPE system which is better than $2x10^{-10}$ Torr Litre/sec in our case. All the gas handling components are properly enclosed in metallic cabinets and are provided adequate exhaust ventilation. It ensures that the gas cabinets are kept at low pressure with respect to the room under all conditions. Furthermore, online gas monitors for H_2, NH_3 and Silane are installed at key locations inside the MOVPE system. Suitable hardware interlocks to act against gas leak, chilled water failure, exhaust ventilation failure etc. are also incorporated in the system.

2.3 Structural characterization by high-resolution X-ray diffraction

High resolution X-ray diffraction (HRXRD) technique is a powerful non-destructive method for determining the crystal structure, lattice constants, strain, and defect density of GaN epitaxial layers. Characterization of GaN epitaxial layers by HRXRD is challenging due to heteroepitaxial growth which results in unintentional impurity incorporation, point defect, dislocations and lattice mismatch in the grown layer. During the course of this thesis, HRXRD measurements are performed on a Panalytical X'Pert PRO MRD instrument with hybrid four-bounce crystal monochromator which gives Cu $K_{\alpha 1}$ (wavelength = 1.54056Å) output with a beam divergence of ~ 20 arcsecs. The different types of scan geometry used in this work are schematically shown in figure 2.3 (a) and are summarized in Table 2.1. The incident x-ray beam is scattered by the electron cloud around each atom in the crystal. The scattered x-rays interfere constructively when the path difference 'AOB' between them becomes equivalent to '2d sin θ' according to 'Bragg's Law' as shown in figure 2.3 (b). Here,'d' is the separation between the atomic planes which participates in the diffraction phenomenon. The positions and shapes of the diffraction spots produced by each set of crystal plane is inversely related to the separation of crystal planes and size of the crystallites. The diffraction spots constitute the reciprocal space where the crystal planes are associated with the real space. Epitaxial nature of thick GaN epilayers can be confirmed by performing ϕ-scans using HRXRD technique. A representative pattern of ϕ-scan of GaN epilayer grown by indigenously developed MOVPE is shown in figure 2.4 for (105) skew-symmetric reflection of GaN. Observation of six distinct peaks separated by 60° clearly confirms the growth of wurtzite GaN epitaxial layer.

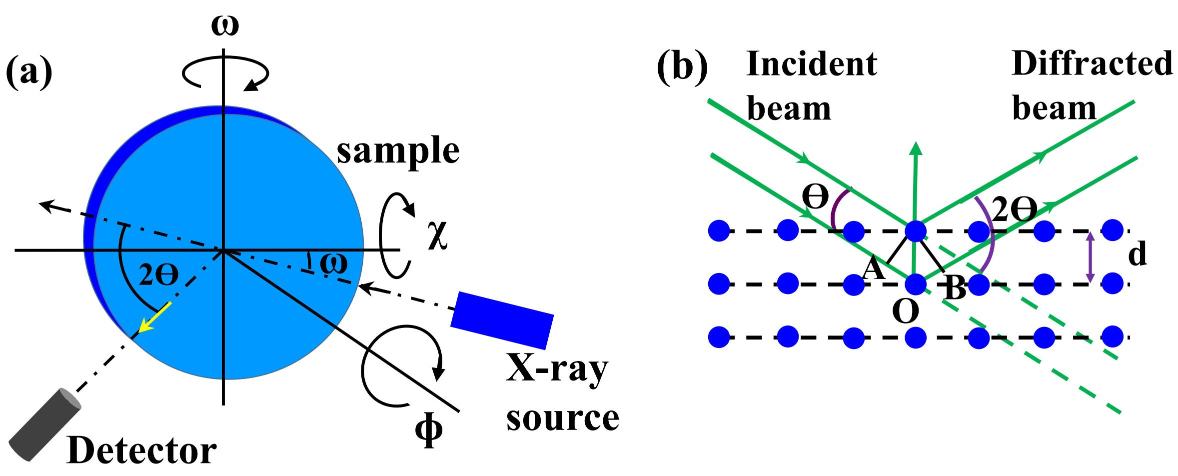

Figure 2.3 (a) Schematic diagram showing different axes of rotation in HRXRD scans. The ω and 2θ are the in plane axes, χ rotates in the plane normal to that containing ω and 2θ. (b) illustration of the conditions required for occurring Bragg diffraction

Table 2.1 Different HRXRD scans used in the present work [64].

Scan Type	Description
ω	Also known as the rocking curve, the detector remains stationary while the sample is rotated about ω axis.
ω-2θ	The sample (or the source) is moved by ω and the detector is moved by 2θ with an angular ratio of 1: 2.
Φ	Rotating the sample about the ϕ axis.
χ	Chi rotates in the plane normal to that containing ω and 2θ.

In order to explore the epitaxial relation between the film and substrate, a similar ϕ -scan for (**$10\bar{1}\bar{0}$**) skew-symmetric reflection of Sapphire substrate is also recorded and the same is shown in figure 2.4. It is observed that the (105) plane of GaN is aligned with the (**$10\bar{1}\bar{0}$**) plane of Sapphire, where the unit cell of GaN is rotated by 30° with respect to that of Sapphire [65]. HRXRD can also be used to check crystalline quality of GaN epitaxial layers as shown in figure 2.5.

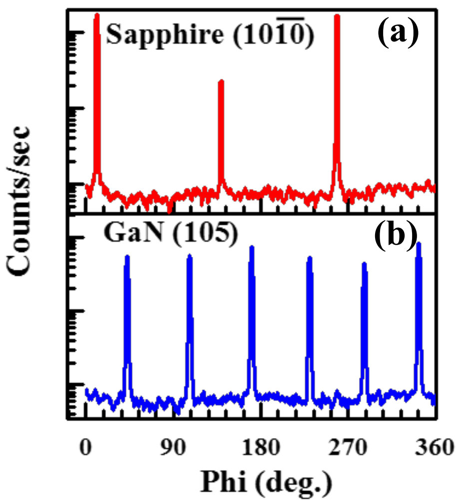

Figure 2.4 (a) Phi scan corresponding to (**$10\bar{1}\bar{0}$**) reflection of Sapphire, (b) (105) reflection of GaN epitaxial layer.

Diffraction peaks corresponding to GaN epitaxial layer are seen at 34.556° and 72.943°, which are labelled as (002) and (004) reflections of wurtzite GaN respectively. It indicates that the film is strongly c-axis oriented. In addition to the peaks corresponding to GaN, two more features are seen in figure 2.5 which are labelled as (006) and (00.12) diffraction peaks of Sapphire substrate. XRD can also be used to dig out information regarding inter planar spacing and defect-related broadening by reciprocal space maps (RSMs). The RSM intensity is actually the projection of 3D intensity of diffraction spot onto a 2D plane. RSM can be acquired by recording a series of ω–2θ scans at different ω values.

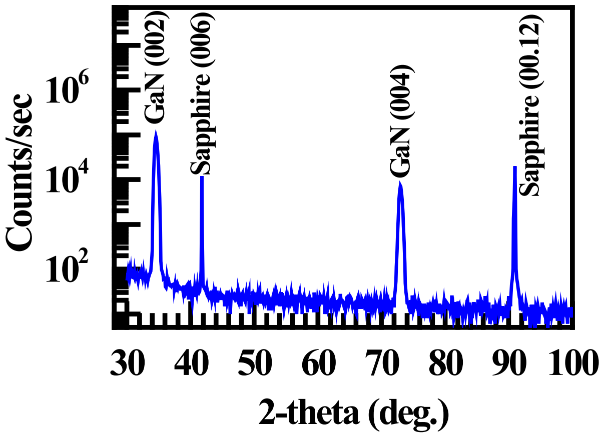

Figure 2.5 XRD pattern of GaN shown over a broad angular range.

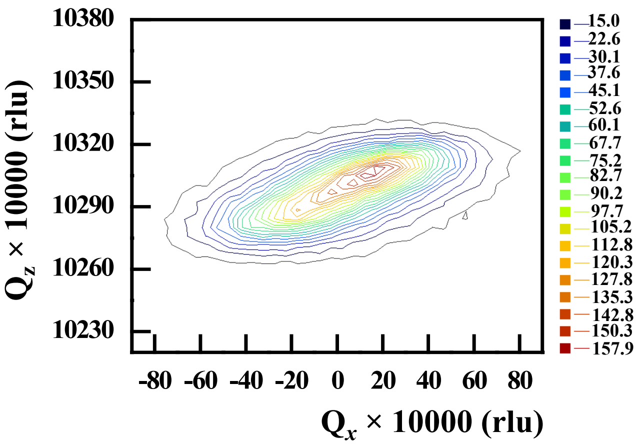

Figure 2.6 Reciprocal space map of GaN sample for (105) reflection.

In order to obtain such plot, the angles ω and 2θ in real space need to be converted into the reciprocal lattice units (1 rlu = 1Å^{-1}) using the following relations [64, 66],

$$q_x = \left(\frac{1}{\lambda}\right)[\cos\omega - \cos(2\theta - \omega)] \tag{2.1}$$

$$q_z = \left(\frac{1}{\lambda}\right)[\sin\omega + \sin(2\theta - \omega)] \tag{2.2}$$

Here, λ is the incident x-ray wavelength, ω is the angle made between the incident beam and the sample surface, and 2θ is the angle between the incident and diffracted beam. Figure 2.6 shows the RSM of GaN sample grown in indigeneously developed nitride MOVPE for (105) reflection where sharp contours corresponding to GaN layer are observed. It clearly shows that the in-plane broadening of layer is larger than the out-of-plane broadening, which is usually observed in case of GaN epitaxial layers grown on foreign substrates [67].

Further, HRXRD can provide a very important information regarding the density of threading screw and edge dislocations present in bulk GaN. For this, a set of symmetric (002) and asymmetric (102) ω-scans are need to be recorded where the formation of defects/dislocations causes significant broadening in both the symmetric and asymmetric diffraction patterns. For example, the (002) and (102) ω-scans of four samples grown in indigenously developed nitride MOVPE are plotted in figure 2.7 whose dislocation density need to be compared. The samples are grown at 1020 °C with V/III ratio of 4273 and thickness of 1 μm. Thickness of GaN buffer layer grown at 550 °C is varied by changing the growth duration from 2-12 min as shown in Table 2.2. As can be seen from figure 2.7, the formation of defects/dislocations causes significant broadening in both the symmetric and asymmetric diffraction patterns for sample T1 where the values of FWHM for the two patterns are 1416 and 1550 arcsec, respectively.

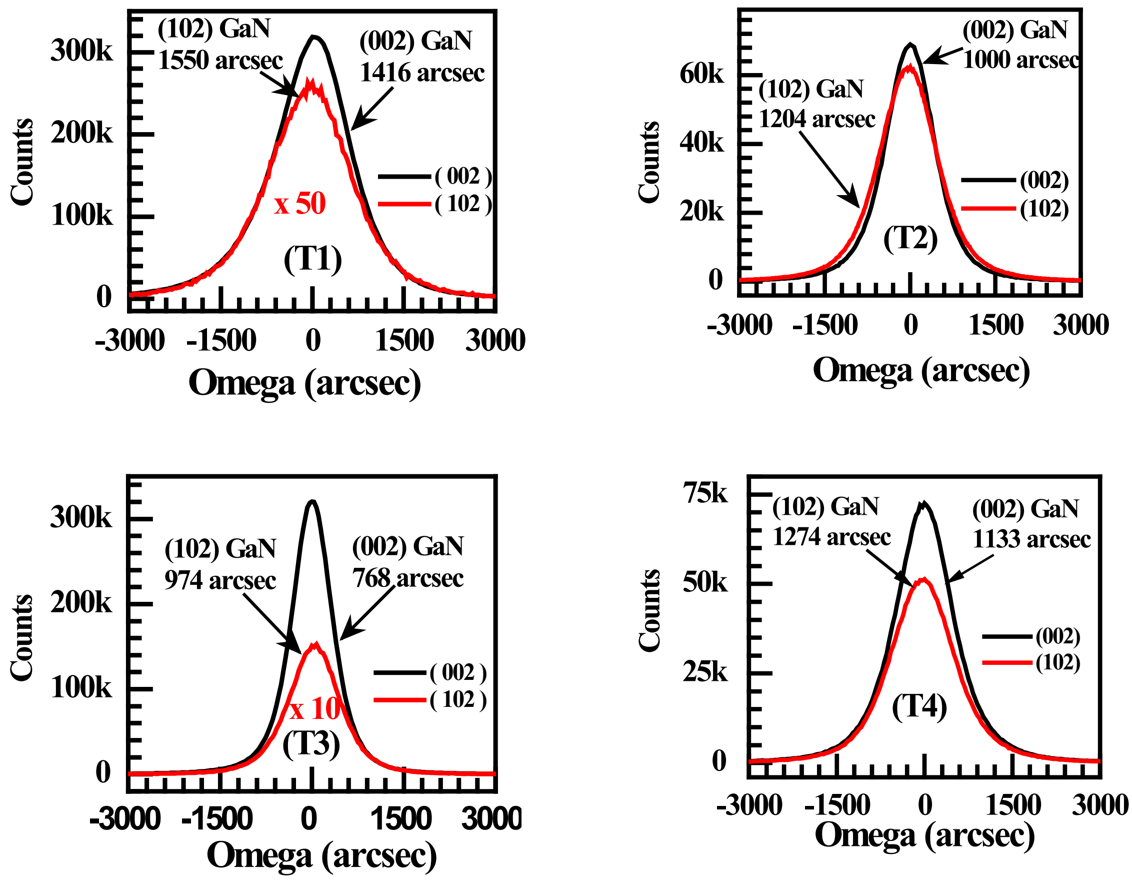

Figure 2.7 Symmetric (002) and asymmetric (102) HRXRD diffraction patterns of MOVPE grown GaN epitaxial layers.

Table 2.2 Growth duration and thickness of GaN buffer layer used in the growth of bulk GaN

Sample No.	Buffer growth time (min.)	Buffer layer thickness (nm)
T1	12	48
T2	06	24
T3	04	16
T4	02	08

It is obvious from figure 2.7 that the crystalline quality of GaN layer improves when the buffer layer deposition time is reduced from 12 to 4 min. However, a further reduction of the growth duration to 2 min. leads to a significant degradation of the crystalline quality of GaN layer in case of sample T4. In case of sample T3, the lowest value of FWHM of symmetric and asymmetric diffraction patterns are recorded. It clearly indicates a considerable reduction in both the edge and screw dislocation density. Moreover, the evident broadening of asymmetric reflection compared to the symmetric one indicates the dominance of pure edge dislocations in GaN epilayers. Note that in ω-scans, the symmetric diffraction peak is broadened mainly by screw or mixed dislocations whereas edge dislocations are known to affect the broadening of asymmetric scans. From the values of FWHM for symmetric (002) and asymmetric (102) reflections, the dislocation density can be estimated as follows [64, 68],

$$D_{screw} = \frac{\beta^2_{(002)}}{9b^2_{screw}}, D_{edge} = \frac{\beta^2_{(102)}}{9b^2_{edge}} \quad (2.3)$$

$$D_{dis} = D_{screw} + D_{edge} \quad (2.4)$$

Here, D_{screw} & D_{edge} are the screw and edge dislocation density, β stands for the FWHM of corresponding diffraction pattern, and b is the Berger vector length (b_{screw} = 0.5185 nm, b_{edge} = 0.3189 nm). The screw and edge dislocation density estimated from HRXRD measurements for all samples are extracted using equation 2.3 and are plotted in figure 2.8.

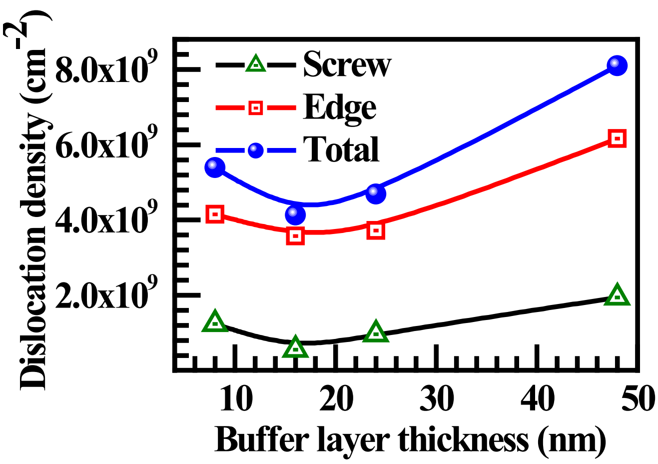

Figure 2.8 Edge, screw and total dislocation density for GaN epilayer plotted as a function of buffer layer thickness.

The minimum value of dislocation density is found to be ~ 4.2×10^9 cm^{-2} which indicates about the reasonable crystalline quality of GaN epitaxial layers [69]. Further improvement in the crystalline quality of the grown layers is therefore needed to achieve superior quality GaN epilayers required for several device applications.

2.4 Electrical characterization techniques

In this section, the various electrical characterization techniques that are used to understand the electronic transport in GaN epitaxial layer are discussed. It is already known that the electronic transport in GaN epilayer and across Schottky junctions is considerably affected by the defects having energy levels in the band gap, which practically limit the performance of a device. These defect levels can trap carriers, allowing them to either recombine with/without emitting radiation, or to generate carriers that add to a detector's current without absorbing radiation, resulting in generation-recombination dark current. Defects also restricts the transient time of photodetectors by reducing carrier mobility, which is proportional to the scattering time. The characterization procedure includes investigation of mobility and carrier concentration by Hall measurements, whereas leakage current, barrier height and ideality factor are determined by current-voltage measurements. Further, depth profiling of carrier concentration is performed by capacitance-voltage measurement technique.

2.4.1 Hall measurements

Hall Effect provides the rich information about the electronic transport properties in semiconductors. It provides a direct evaluation of the carrier type and concentration which in conjunction with the resistivity yields the information about carrier mobility. Since the carrier concentration in GaN is largely affected by unintentional doping due to impurity incorporation, defects and dislocations, a careful measurement of carrier concentration by Hall technique becomes very useful in evaluating the properties of GaN epilayers.

A Hall voltage is generated when a current carrying conductor is placed in a magnetic field perpendicular to the direction of current flow. In the absence of magnetic field, the current in the conductor is consisted of a stream of charged particle drifting under the influence of applied electric field. However, under application of magnetic field, the charge carriers experience Lorentz force = $\mathbf{q}\left(\vec{\mathbf{v}} \times \vec{\mathbf{B}}\right)$, where v is the drift velocity and B is the magnetic field. Hence, the charge carriers are swept towards the edge of sample as shown in figure 2.9. This process continues until the non-uniform charge distribution exerts an equal and opposite force against the deflecting force exerted by the magnetic field i.e.

$$q\,\vec{E}_H + q\left(\vec{v} \times \vec{B}\right) = 0 \tag{2.5}$$

where E_H is the Hall field across the semiconductor. A solution of the above equation yields, $\vec{E}_H = -(\vec{v} \times \vec{B})$. It is therefore obvious that E_H is proportional to the product of current density (J) in the sample and the applied magnetic field B, the constant of proportionality is called the 'Hall coefficient (R_H)'. Mathematically this can be expressed as follows: considering the current density $\mathbf{J} = \mathbf{nqv}$ with 'n' being the carrier density and using the relation in equation 2.5, the expression of E_H can be re-written as

$$E_H = -R_H\, J\, B \tag{2.6}$$

where R_H can be expressed as, $R_H = 1/nq$. For a rectangular sample of width 'a' and thickness 'b' and considering an uniform distribution of current, equation 2.6 can be rewritten in terms of the total current I, the Hall voltage V_H, and the sample dimensions as,

$$E_H = \frac{V_H}{a} = -\frac{R_H I B}{ab} \tag{2.7}$$

Hence, the Hall voltage can be written as, $V_H = -\frac{R_H I B}{b}$. Using the expression of the Hall voltage V_H and the sample thickness b, the carrier concentration in the sample can be calculated as, $n = \frac{IB}{qV_H b}$. Also note that the equipotential lines are no longer normal to the current flow after the application of external magnetic field, rather rotated through an angle θ, called the 'Hall angle' as shown in figure 2.10 (a).

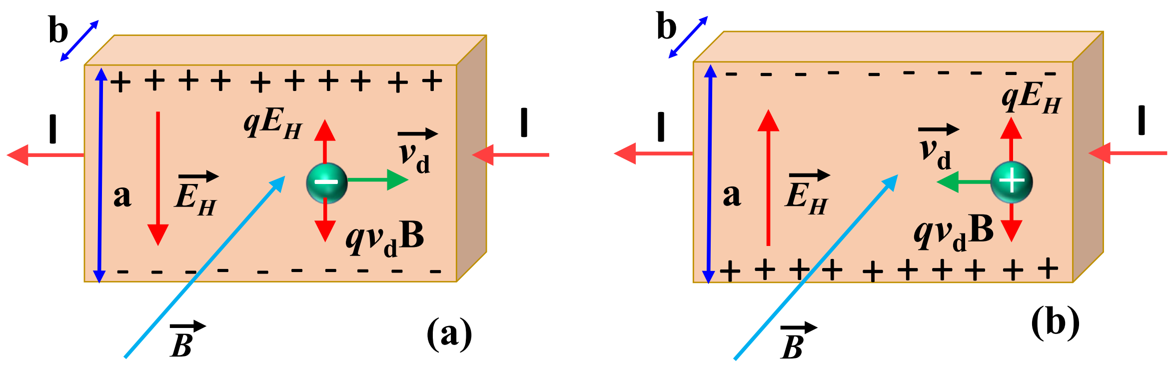

Figure 2.9 Schematic of Hall effect in (a) n-type and (b) p-type semiconductor

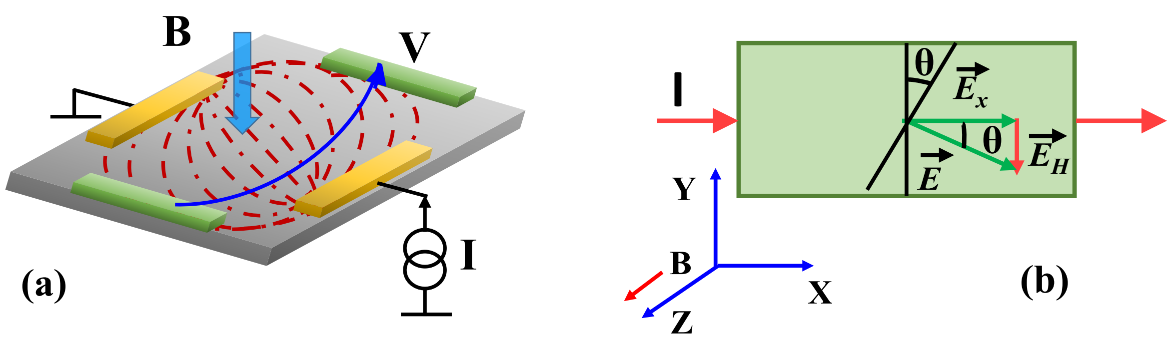

Figure 2.10 (a) Rotation of equipotential lines due to Hall effect since they no longer remains normal to the current flow (b) Hall effect vector diagram where the Hall angle θ is the angle of rotation of the equipotential lines due to external magnetic field.

From the vector diagram of the fields shown in figure 2.10 (b), it is clear that the Hall angle can be determined by the following relation: $\tan\theta = {E_H}/{E_x} \cong \theta$, for small angles. Here, E_x is the drift electric field. Considering $E_H = -R_H J B$ and $E_x = J/\sigma$, where σ is the conductivity, the Hall angle can be written as, $\theta = R_H B \sigma$.

In general, several parasitic contributions like misalignment voltage, thermomagnetic and galvano-magnetic effects namely the Ettingshausen effect, the Seebeck effect, the Nernst effect, and the Righi-Leduc effect [70] sometimes significantly limit the capabilities of Hall experiments where even the measurement of carrier type in some samples becomes doubtful. The major parasitic contributions from the measured Hall voltage can be eliminated by a systematic averaging procedure over the current and magnetic field, detail of which is discussed in [70].

In the present work, the temperature dependent Hall measurements are performed using two Keithely 236 source/measure units and one 2361 trigger controller unit over a wide temperature range using Helium based close cycle refrigerator. All the SMUs used are interfaced to a PC. The schematic of electronic transport measurement setup is shown in figure 2.11 (a). As shown in the figure, the measurement units are interfaced with PC through IEEE GPIB cards. The measurement system consists of an electromagnet providing a static magnetic field with a peak field capability of 1.5 Tesla as shown in figure 2.11 (b). For Hall measurements to be performed under van der Pauw geometry, the sample is mounted in config-1 as shown in figure 2.11 (c). The sample is mounted on Sapphire which helps in efficient heat transfer to the cold head of CCR and also ensures a perfect electrical isolation.

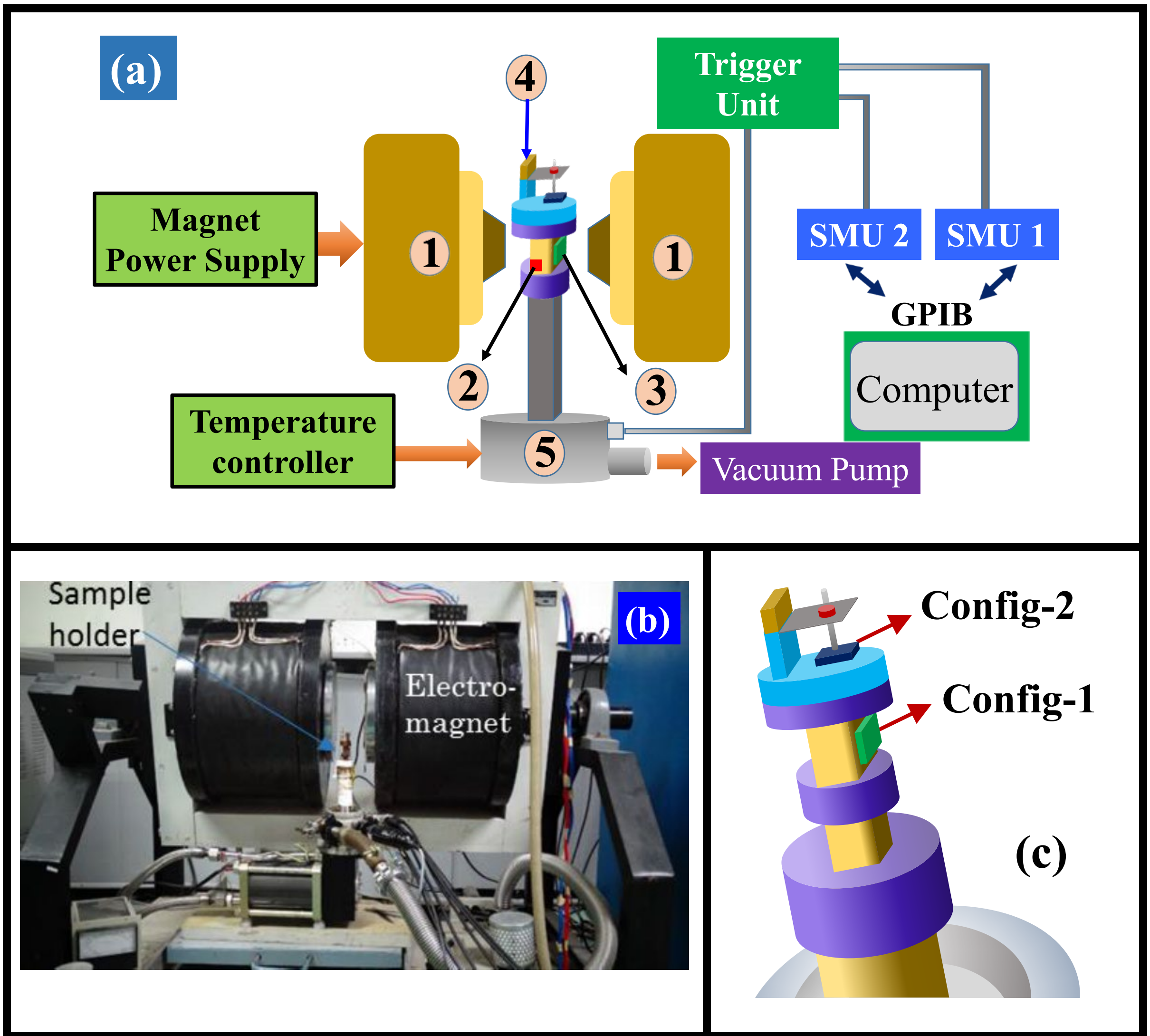

Figure 2.11 (a) Schematic diagram of the experimental set up showing 1) magnet pole pieces, 2) sample heater, 3) sample, 4) sample holder, 5) cryo-cooler, (b) photograph of Hall set up and (c) schematic of sample holder with two different mounting configurations.

The electrical contacts soldered with indium on sample surface are taken out from the cryostat and are connected to Triac connecters which are further connected to source measure unit (SMU). The SMUs can source and measure voltage in the range of ±100 µV to ±110 V and current in the range of ±10 fA to ±100 mA. For performing temperature dependent measurements, heater cartridge of 50 W is used as a resistive heater, whose power is controlled through a Cryocon 32B temperature controller. The temperature is measured with calibrated PT-1000 temperature sensors and the enamelled copper wire is used for internal wiring. The operating principle of the cryocooler is based on Gifford McMohan Refrigeration Scheme, where He gas is used as refrigerant. This Cryocooler is indigenously made by the cryogenic laboratory, RRCAT and works in the temperature range of 40-300K.

2.4.2 Capacitance-Voltage measurement

Capacitance voltage (C-V) is a unique measurement technique which provides information of charged carrier concentration near the surface region of bulk semiconductors. The capacitance measured at the edge of the depletion provides the information about the net density of ionized dopants (donor or acceptors) at the edge of depletion width ($\mathbf{N_d^+}$), along with its depth dependence while varying the applied reverse bias [71]. This is in contrast to the Hall transport measurement which offers the information related to density of free charge carriers along with their mobility. The capacitance associated with depletion region is called the depletion capacitance which depends on the distributed fixed charge density of ionized donors in the depletion region. For a small increase in reverse bias voltage of dV, if dQ is the change in fixed charge per unit area, then the capacitance associated with the depletion width can be written as,

$$C = \mathrm{A}\left(\mathrm{dQ}/\mathrm{dV}\right) \tag{2.8}$$

Where A is the diode area. The incremental charge dQ due to an increase in reverse bias voltage of dV is associated with the increment in the depletion width dW by the following relation,

$$dQ = \mathrm{q\,A\,N_d^+\,dW} \tag{2.9}$$

This region can also be modelled as a parallel plate capacitor with capacitance,

$$C = \varepsilon_{\mathrm{o}}\,\varepsilon_{\mathrm{r}}\,\mathrm{A}/\mathrm{W} \tag{2.10}$$

Combining equation 2.10 with the expression of C in equation 2.8 leads to the expression of carrier density profile as,

$$N_d\,(\mathrm{w}) = 2\Big/ q\,\varepsilon_0\,\varepsilon_r\,\mathrm{A}^2\,\frac{d}{dV}\left(\frac{1}{C^2}\right) \tag{2.11}$$

Thus, a plot $1/C^2$ versus V will generate a straight line, slope of which will give the value of the ionized donor density.

Practically, while performing experiments, the differential capacitance measures the incremental variation in charge at the edge of the depletion width as probed by the applied ac voltage. When a small ac voltage $V_{ac}=V_0\,e^{i\omega t}$ is applied to the depletion region having a capacitance C, then the expression for current flow is,

$$I_C = \frac{\mathrm{dQ}}{\mathrm{dt}} = \mathrm{C}\frac{\mathrm{d}}{\mathrm{dt}}(\mathrm{V_{ac}}) = \mathrm{i}\,\omega\,\mathrm{C}\,\mathrm{V_{ac}} = \omega\,\mathrm{C}\,\mathrm{V_0}\,\exp(\omega\,\mathrm{t}+\pi/2) = \mathrm{I_0}\,\exp(\omega\,\mathrm{t}+\pi/2) \tag{2.12}$$

where, $i = e^{i\pi/2}$ and $I_0 = \omega\,C\,V_0$. This expression indicates that current is 90° out of phase with voltage. In reality, there exists some leakage of charge through the capacitor, which gives rise to the leakage current of the form

$$I_L = \frac{\mathrm{V_{ac}}}{\mathrm{R}} = \mathrm{V_{ac}}\,\mathrm{G} \tag{2.13}$$

where R is the resistance and G is the conductance. Therefore the expression for total current becomes $I=I_0+I_L = (i\omega C_0+G)\,V_{ac}$. Thus, by measuring the current and voltage with their respective phases, one can obtain the capacitance (imaginary part) and conductance (real part). Hence, in practical case, every diode can be represented by a junction capacitance (C) in parallel with the junction conductance (G) due to leakage current through the Schottky junction and a series resistance (R_S), which can be modelled by the equivalent circuits as shown in figure 2.12.

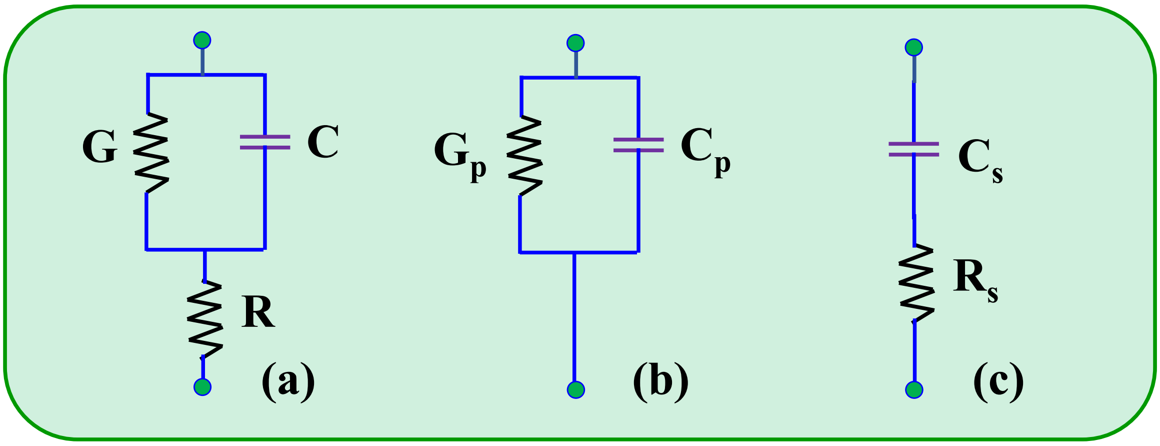

Figure 2.12 (a) actual circuit (b) parallel, and (c) series equivalent circuit of Schottky diode.

Here, C_s (G_s) are the capacitance (conductance) in series equivalent circuit, and C_p (G_p) are the capacitance (conductance) when they are in parallel equivalent circuit. Generally, parallel (series) equivalent circuit is preferred depending on smaller (larger) impedance of the device. In present study, parallel equivalent circuit is chosen due to higher doping of GaN epitaxial layers leading to lower impedance.

In present work, temperature dependent C-V measurements are performed using Keithely 590 C-V Analyzer. The system offers the flexibility to select the required measurement frequency from 1 MHz and 100 kHz. It can measure capacitance up to 20 *nF* (at 100 kHz) to test large, leaky, or forward biased devices with a sensitivity of 0.1 *fF* to test small devices. It has built-in test setup and facility for data storage, analysis, and plotter control to minimize computer programming. The system also offers correction for transmission line errors due to device connections.

2.4.3 Current-Voltage measurement

Current voltage (I-V) measurement is a very useful electrical characterizing technique for evaluating the rectifying properties of Schottky barrier diode [72]. Various Schottky junction parameters like barrier height, ideality factor and saturation current can be measured using this technique. In determining these parameters, it is assumed that the current transport is dominated by the thermionic emission mechanism. The current flowing across the Schottky junction can be expressed using this model as

$$I_F = I_{SF} \exp\left(\frac{qV}{\eta_F kT}\right) \tag{2.14}$$

where I_F, η_F and V factor are the diode current, ideality factor and applied voltage under forward bias, *q* is the electronic charge, and I_{SF} is the forward bias saturation current given by, where $I_{SF} = A\,A^*\,T^2 \exp\left[-\left(q\,\phi_{B0}\,/\,k\,T\right)\right]$ is the saturation current, A is the Schottky junction area, A* is the Richardson constant and ϕ_{B0} is the zero bias barrier height, k is Boltzmann's constant. Figure 2.13 shows the I-V characteristic of an ideal and practical Schottky barrier diode. Note that, for an ideal diode, the value of η_F is unity. However in presence of defects, trap levels, generation-recombination centres, η_F assumes a value higher than unity. The expression of I_{SF} can be rearranged to extract the value of A* and ϕ_{B0} as,

$$\ln\left(I_{SF}\,/\,A\,T^2\right) = \ln A^* - q\phi_{B0}\left(1\,/\,k\,T\right) \tag{2.15}$$

The slope of ln (I_{SF}/AT^2) versus 1/ kT plot will give the value of ϕ_{B0} whereas the intercept will provide A*. Note that the theoretical Richardson constant with units of A cm^{-2} K^{-2} is given by [46],

$$A^* = \left(4\,\pi\;q\;m^*\;k^2/h^3\right) = 120\;\left(m^*/m_0\right) \tag{2.16}$$

where *h* is Planck's constant, m* is the majority carrier effective mass, and m_0 is the mass of electron. Considering the electron effective mass in GaN to be 0.222 m_0 [73], the Richardson constant for *n*-type GaN is found to be 26.9 A cm^{-2} K^{-2}.

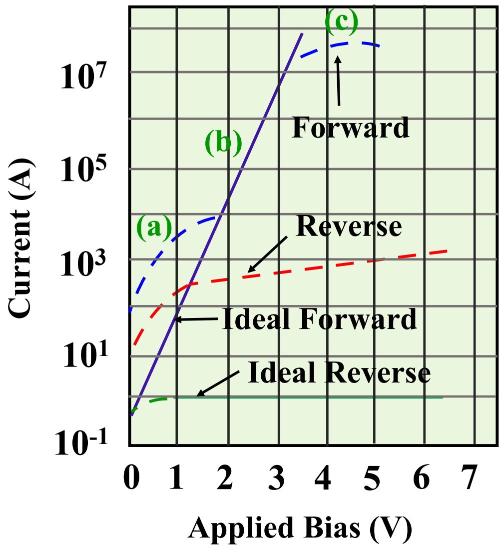

Figure 2.13 I-V characteristics in forward and reverse bias of an ideal and real diode.

In case of practical Schottky junction based devices, the forward current across the Schottky diodes is having three distinct regions: (a) the generation-recombination current region, (b) diffusion current region and (c) region effected by series resistance as shown in figure 2.13 [72]. The ideality factor can be extracted from the region (b) and is expressed as

$$\eta_F = \frac{q}{kT}\left(\frac{dV}{d\ln I_F}\right) \tag{2.17}$$

The series resistance is determined from the region (c) of figure 2.13 where the voltage is high.

In case of Schottky junction diodes, tunnelling of carriers may occur at the interface between metal and semiconductor. It is of immense importance to measure the leakage current since a high value of the same may lead to the device failure. As can be seen from figure 2.13, reverse bias leakage current in ideal diode is much lower in magnitude and depends very weakly on the applied bias in compare to the practical case. This is very important since it largely affects the responsivity and transient response as well as detectivity of any photo detector which are the major figure of merit.

2.5 Optical characterization techniques

In this section, interaction of light beam with semiconductor material is discussed. When a light beam propagates through a semiconductor material, a fraction is reflected back from the front surface while the remaining part is either absorbed within the layer or is transmitted. The part of the incident light absorbed in the media injects electron-hole pairs which may recombine to give either luminescence or heat. Optical characterization provides unique information about the band gap, impurities and defect levels present in the semiconductor material.

2.5.1 Photoluminescence measurement

Photoluminescence (PL) spectroscopy is a powerful emission based non-destructive technique for the optical characterization of semiconductors. In this technique, optical response from the semiconductor sample is analysed by measuring the energy distribution of emitted photons subsequent to optical excitation. Traditionally, optical excitation of semiconductor sample is done with a laser, which has the photon energy greater than the band gap of layer. This process is called photo excitation which creates electron (hole) in conduction (valance) band. During the de-excitation process to the equilibrium states, electrons first loses their excess energy via interaction with phonons. This process mainly takes place in the pico-second or sub-picosecond scale depending upon the kinetic energy of photo generated electrons and is non-radiative in nature. Once electrons reach the conduction band minima, they recombine with holes and the energy released may or may not lead to emission of light depending on the dependence of radiative or non-radiative recombination mechanism. In case of radiative recombination, the energy of PL signal is related to the bandgap of material. Various downward optical transitions that are possible to measure by PL are shown schematically in figure 2.14.

Several possible recombination processes are (1) band-to-band, (2) excitonic transition between shallow donor and valence band, (3) conduction band-to-shallow acceptor (4) donor acceptor pair and (5) between shallow donor and deep trap states as schematically shown in figure 2.14.

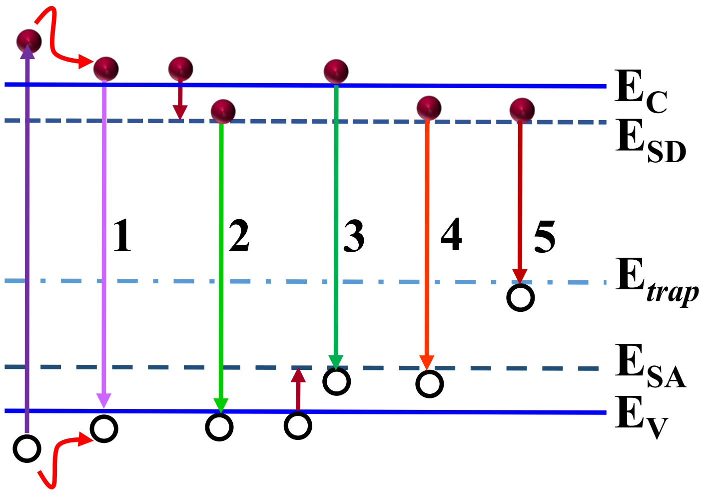

Figure 2.14 Schematic diagram showing different PL transitions in semiconductor.

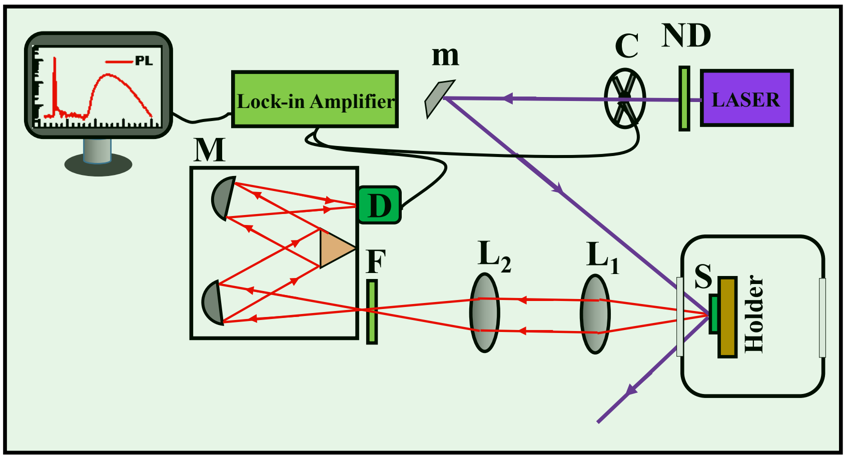

Figure 2.15 Schematic representation of a PL measurement setup where symbols ND, C, m, M, D, L and S stand for neutral density filter, mechanical chopper, mirror, monochromator, detector, lens and sample respectively.

The experimental setup for the PL measurement is shown in figure 2.15. A 325 nm He-Cd CW laser is used as an excitation source. The monochromatic light from the laser is chopped with a certain frequency by a mechanical chopper. This makes the photo luminescence signal periodic with frequency equal to that of chopper. The ac output signal, even very weak, can be detected with the help of a lock-in amplifier. The lock-in amplifier multiplies the input signal with the reference signal and integrates it over a defined time, usually from milliseconds to a few seconds. As a result, in the output DC signal, any other contribution which is not at the same frequency as the reference signal is cancelled. The lock-in amplifier supports the phase-sensitive detection of PL signal and enhance the signal-to-noise ratio significantly. The samples are mounted on a copper holder placed in a closed cycle Helium cryostat for low temperature measurement down to 10 K. After that the photons emitted by the sample are collected and focused by a set of plano-convex lenses. This arrangement reduces possible chromatic aberration in the measurement. The photon signal is transferred to ihr550 monochromator. An appropriate long pass filter is used to block the laser before it gets into the monochromator. The dispersed luminescence is then read with the help of a photomultiplier tube/Si photodiode. PL measurements were performed on all the four in-house grown GaN samples and the spectra are shown in figure 2.16. It is known that the residual stress in film modifies the band gap of a semiconductor. A compressive stress is known to increase the band gap of a semiconductor material. It is seen that the PL peak of all the samples appear at high energy when compared with the band gap of bulk GaN at room temperature. Hence, all the grown layers are under compressive stress which is in good agreement with the HRXRD results [63].

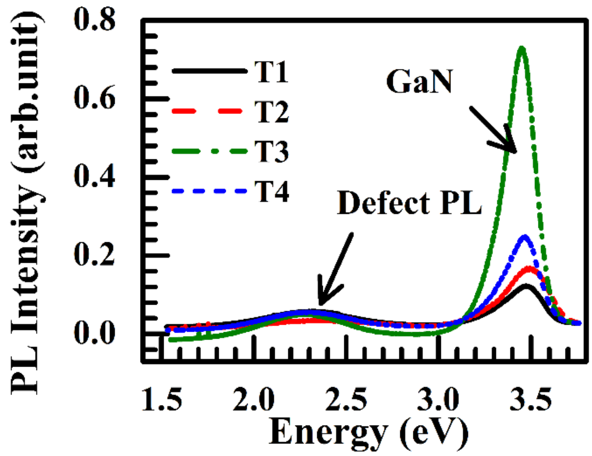

Figure 2.16 Room temperature PL spectra of GaN epitaxial layers grown by using the indigenous MOVPE system

Furthermore, the PL peak of T3 sample appears at the lowest energy which confirms the observation made from HRXRD measurements where the particular sample is seen to possess the minimum compressive stress. PL intensity (FWHM) is measured to be the highest (lowest) in case of sample T3 respectively.

2.5.2 Spectral response measurement

When a photo detector is illuminated with optical radiation having energy higher than its band gap, electron-hole pairs are generated as discussed in the previous section. The carriers are then swept out by the built-in voltage in the depletion region of the detector. Also the carriers generated within minority carrier diffusion length, diffuse into the space charge region before recombination and are swept out to the respective regions. Thus the resulting photo current is contributed by both the carrier diffusion and drift. The various detector parameters are estimated from the spectral response measurements like responsivity, quantum efficiency etc. Schematic experimental setup used for spectral response measurements is shown in figure 2.17.

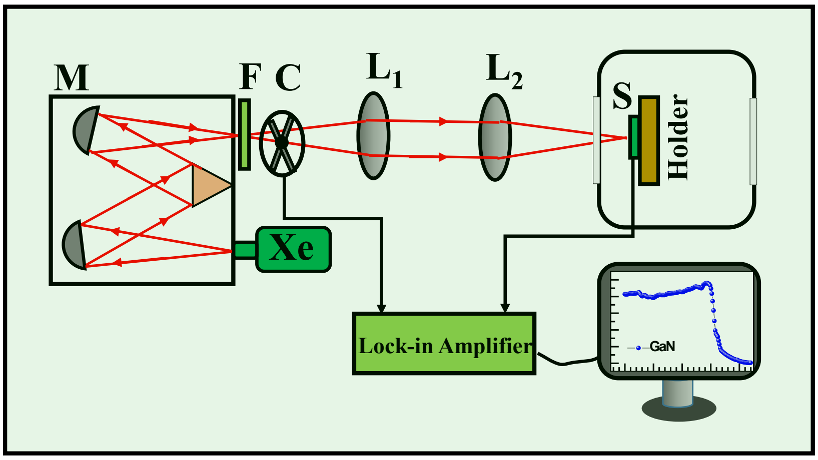

Figure 2.17 Schematic representation of spectral response measurement setup where symbols C, F, M, L and S stand for mechanical chopper, filter, monochromator, lens, and sample respectively.

A 100W Xenon lamp is used as tuneable light source, which is directly connected to a Horiba ihr320 monochromator. The monochromator is used to disperse the incident illumination. The incident monochromatic light is modulated using an optical chopper and is directed onto the photo detector from top. The photocurrent is recorded using a dual channel lock-in amplifier of Stanford Research Systems make. An indigenously designed Labview user interface is used to automate the measurements over a large wavelength range. The program communicates with the connected equipment digitally which are monochromator and lock-in amplifier. At the beginning of the measurement, monochromator adjusts its gratings to the pre-defined wavelength, and the lock-in records the current 9 times in a row and the data is averaged for each incident wavelength. After that the monochromator is set to the next wavelength. This loop continues until the final wavelength is reached. The recorded photo current data is calibrated using the spectral response of the measurement setup.

The performance of a detector is described in terms of certain figures of merits which can be measured from the spectral response measurement. These are discussed on the next page [74].

Responsivity (R): Responsivity of a detector is defined as the ratio of the photo generated output voltage or current (I) of the photo detector to the input radiant power (P) in Watt.

$$R = I/P \tag{2.18}$$

The unit of responsivity is amperes/watt.

The responsivity of a photo detector depends on several factors, like wavelength of detection, size and geometry of detector, and internal gain (if any). Power density of incident radiation is kept low to ensure that it doesn't saturate the detector.

Quantum Efficiency (η): It is defined as the ratio of the number of photoelectrons generated to the number of incident photons per second.

$$\eta_e = \frac{\text{No. of electrons produced}}{\text{No. of incident photons}} \times (100\%) = \frac{I/q}{P/h\upsilon} = 1240\frac{R}{\lambda(\text{nm})} \tag{2.19}$$

Noise Equivalent Power (NEP): It is the minimum incident optical power that a detector can distinguish from the noise.

$$\text{NEP} = (A\,\Delta f)^{1/2}/D^* \tag{2.20}$$

where A is the effective device area in unit of cm^2, Δf is the electrical bandwidth in Hz, and D* is the detectivity of the device in Jones.

Detectivity (D*): It is the figure of merit of the device and describes the lowest limit of radiation to which the photo conductor can respond. Large detectivity means the detector can measure the signal current in presence of a very low radiation level.

$$D^* = (A\,\Delta f)^{1/2}\,R/I_n \tag{2.21}$$

where the responsivity (R in A/W) should be measured under the same conditions as the noise current (I_n in amperes). There are four major factors for the noise current that limit D*, these are shot noise from dark current, Johnson noise, dark current noise and 1/f noise [74].

Johnson noise (I_{nJ}): It is associated with the fluctuation in thermal velocity of free charge carriers in any resistive element and is also called thermal noise. The noise current is proportional to the absolute temperature T and can be expressed as

$$I_{nJ} = \sqrt{4\,k\,T\,B\,/\,R_s} \tag{2.22}$$

where R_s is the resistance and B is the band width.

Shot Noise (I_{ns}): Shot noise is generated due to the statistical nature of generation of the electron hole pairs due to photon excitation. It is associated with the photo current itself and can be expressed as

$$I_{ns} = \sqrt{2\,q\,I_{ph}\,B} \tag{2.23}$$

where I_{ph} is the signal photo current and B is the band width.

Dark Current Noise (I_{nd}): It is defined by the contribution in detector current that is present in absence of any photo excitation. Since the carrier generation process is of statistical nature similar to shot noise, the dark current noise can also be treated as white noise and can be expressed as

$$I_{nd} = \sqrt{2\,q\,I_S\,B} \tag{2.24}$$

where I_S is the reverse bias saturation current in dark and B is the band width.

1/f Noise: The term 1/f noise represents several different types of noise that are present at low modulation frequency. It originates at the semiconductor interfaces where the surface states play a crucial role in the trapping and de-trapping of charge carriers.

$$I_{nf} = \sqrt{I^2 B/f} \tag{2.25}$$

The 1/f noise can be reduced by operating the detector at considerably high frequency.

2.5.3 Transient response measurement

In transient response measurements, the change in conductivity of photo detector due to the generation of photo current is measured as a function of time. The decay profile of photocurrent transient manifests the recombination time and trapping properties of the material. Figure 2.18 shows the experimental set-up used for the transient photo current measurements. The excitation source used in this case is He-Cd laser of 325 nm wavelength. It is passed through Nd filter to vary the optical power of the laser. The photo-response of the device is recorded using Keithley 2450 source measure unit. A mechanical shutter interfaced with the computer using Labview user interface is used to automate the measurements over a long period of time. The rise and decay curves are fitted using the exponential rise and decay equations given as follows [75]:

$$\text{Rise equation}: I_r(t) = I_{dark} + A\left[1 - \exp\left\{\frac{-(t - t_{on})}{\tau_1}\right\}\right] + B\left[1 - \exp\left\{\frac{-(t - t_{on})}{\tau_2}\right\}\right] \tag{2.26}$$

$$\text{Fall equation}: I_r(t) = I_{dark} + A\left[\exp\left\{\frac{-(t - t_{off})}{\tau_1}\right\}\right] + B\left[\exp\left\{\frac{-(t - t_{off})}{\tau_2}\right\}\right] \tag{2.27}$$

where I(t) is the photocurrent at time t, I_{dark} is the dark current, A and B are scaling constants, τ is the time constant, and $t_{on(off)}$ is the time of switching the lamp on (off).

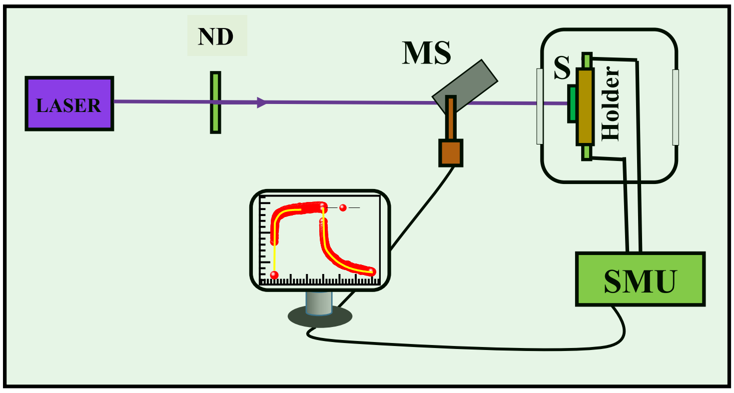

Figure 2.18 Schematic representation of transient response measurement setup where symbols ND, MS and S stand for neutral density filter, mechanical shutter and sample respectively.

2.6 Sample details

PL and HRXRD measurements confirmed that the crystalline quality of the samples grown in the in-house developed nitride MOVPE system needs further improvement. Also the free carrier density obtained from Hall measurement is about 1×10^{20} cm^{-3}, making them unsuitable for device applications. Keeping this in mind, commercially available GaN epitaxial layers are used for further investigations. The samples are 5 µm thick and are grown by HVPE and MOVPE technique on Sapphire substrate. The sample details are given in Table 2.3. Note that the sample A and C are grown by HVPE and possess similar free carrier density but are from different batch of same vendor.

Table 2.3 Electrical transport parameters of GaN Samples used in the present work.

Sample No.	Growth Technique	Free carrier concentration (cm^{-3})	Mobility (cm^2/V-s)
A	HVPE	$(2 \pm 0.1)\times10^{18}$	84 ± 4
B	MOVPE	$(2 \pm 0.1)\times10^{18}$	270 ± 10
C	HVPE	$(2 \pm 0.1)\times10^{18}$	130 ± 4

Sample C is having slightly higher mobility than sample A. Most of the studies in the present thesis are reported on sample A. Sample C is used only in chapter 5 for studying the role of oxide interlayer on the device performance.

2.7 Fabrication techniques

In this section, the fabrication technology of GaN photodetectors is discussed. This includes chemical cleaning for the removal of organic, and metal ion contaminants followed by optical lithography for defining Schottky contact on GaN sample, metallization by thermal evaporation technique, rapid thermal annealing, and oxide layer deposition by e-beam evaporation technique. Further, a dry etch process of GaN is also discussed in this section.

2.7.1 Chemical cleaning of GaN surface

Removal of surface contamination is extremely important prior to the fabrication of a semiconductor device. There are two primary objectives behind a chemical cleaning step. The first is to remove the surface contaminates such as metal ions and organic compounds. The second is to remove the native oxides to expose the substrate for further processing such as fabrication of metallic contacts. GaN wafers might be contaminated with the organic vapours present in the air even if they are exposed only for a short duration. The organic cleaning procedure adopted in this thesis is as follows. In first step, the samples are boiled in Tri Chloro Ethane (TCE), acetone and methanol and then rinsed with deionized water (DI) to remove metallic ions. Note that pure DI water can easily dissolve metallic ions. The cleaned surface is then dipped into a solution of hydrochloric acid (HCl) and water in the ratio of 1:1 for 10 sec. to remove the thin layer of native oxides from GaN surface. Finally, the samples are rinsed with DI water again and dried using nitrogen gas.

2.7.2 Optical lithography

Photolithography is a very critical step for device fabrication at microscopic level which helps in defining the device geometry, electrode dimension and separation between the contacts. It uses UV light to transfer a specific device pattern from an optical mask to a photoresist coated wafer. In the present work, an indigenously developed mask-less photolithography system using a digital projector and an optical microscope is used for the fabrication of GaN photodetectors [76]. The system is highly appropriate for the device fabrication with minimum feature size ~ 20 μm, over a surface exposure area of 6×8 mm^2. Generally, the sequence of processing steps follows as spin coating of photoresist, pre bake, exposure to UV radiation, and then dipping in the developer. This sequence is schematically shown in figure 2.19 and a brief discussion of each step is given below.

Step 1: Spin coating of Shipley 1813 positive photoresist (PR) and Microchem lift-off resist LOR 5A. The parameters for spin coating are:

i) Coating LOR 5A at an rpm of 4000 for 30 sec.

ii) Coating S1813 at an rpm of 3500 for 30 sec.

The use of a two-layer scheme based on LOR resist allows to form a negative slope of the resist walls after development which facilitates the process of post metallization lift-off.

Step 2: Prebaking of samples necessary for drying the photoresist after spin coating to reduce the excess solvent content. There are four major consequences of pre bake of photoresist film: (1) reduction of film thickness, (2) changing post exposure bake and development properties, (3) improving adhesion and (4) achieving films that are less susceptible to particulate contamination. Typical prebaking results only 3-8 percent residual solvent present in the photoresist which is sufficient to keep the film stable during subsequent lithography processing. The parameters for prebake are:

i) Baking at 120 ^{o}C for 1 min. for LOR 5A -1st layer

ii) Baking at 95 ^{o}C for 1 min. for S1813 resist -2nd layer

Step 3: Photolithography for pattern transfer. In some cases, standard photolithography system of Quintal, USA make is also used where alignment of optical mask and exposure of resist coated sample to UV radiation is carried out. Here, the UV light is allowed to pass through an optical mask which fall on the resist coated sample surface. However, one requires a new set of masks for photolithography, in case a change in the geometry of detector element is needed. It not only requires extra funds and efforts but also discourages newer developments. In view of this, a low cost mask-less photolithography setup is used in the development of photodetectors during the course of this thesis work. Nevertheless, the basic principle of photolithography remains the same. Here, UV exposure is required to change to solubility of the resist in a developer upon exposure to light. The photo active compound in resist which is not soluble in aqueous base developer is converted to a carboxylic acid on UV exposure in the range of 350-450 nm for 7 sec. The carboxylic acid product is highly soluble in the basic developer.

Step 4: Development of UV exposed sample in developer solution, MF-CD 26, for 1 minute at 80 ^{o}C temperature. The developing process is performed in two steps. In first step, 1 min. development removes the exposed regions of S1813 resist. In second step, the sample is baked at 120 ^{o}C for 1 min. This is followed by another development of the sample in MF-CD 26 for 1 min. which helps in achieving sufficient undercut profile.

Step 5: Metallization and lift-off for achieving desired metal contact geometry necessary for detector application. The metal coated sample is dipped in PG remover chemical kept at about 80 ^{o}C for the lift-off purpose. The sample is further washed using DI-Water for 1 minute and dried using a nitrogen jet.

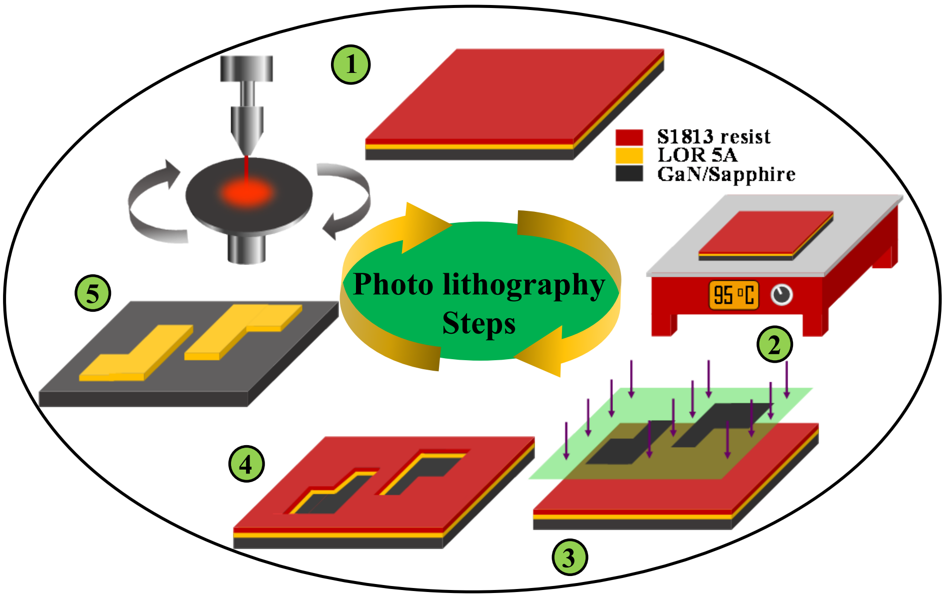

Figure 2.19 Schematic flow chart of optical lithography process showing various steps.

Figure 2.20 Photograph of (a) thermal (right) and (b) e-beam (left) coating unit used in present work.

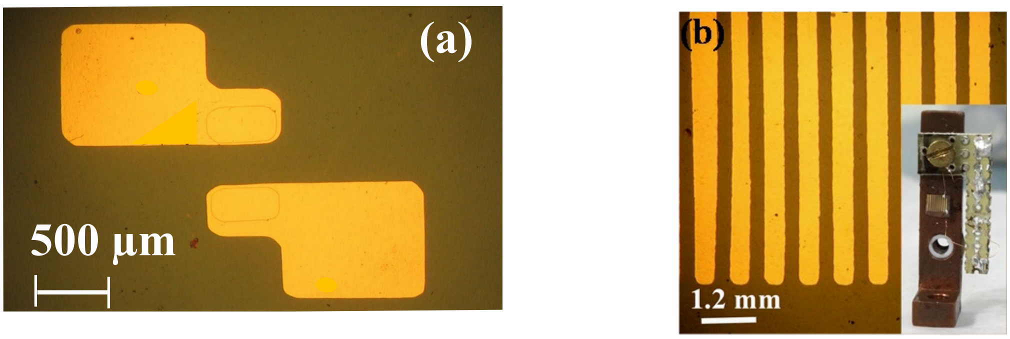

Figure 2.21 (a) Real image of the MSM fingers of 500 µm long and 250 µm wide with a separation of 300 µm, (b) image of MSM device fabricated with metal mask with contact width of 500 µm, and separation of 200 µm.

2.7.3 Metallization by thermal evaporation technique

It is needed to deposit metal onto substrates that have been patterned using lithography techniques for the fabrication of optoelectronic device. The simplest method of metal thin film deposition is thermal evaporation technique in which metals are heated on a filament wire or in a boat/crucible. This method produces good quality Schottky contact since the deposition is carried out under high vacuum (~ 5×10^{-6} bar) which avoids the possible degradation of device performance by the impurity contamination. The vacuum coating unit (Make: HINDHIVAC, Model: 12A4D) based on thermal evaporation process is used for the deposition of metal film and the setup is shown in figure 2.20 (a). Using this system, Au(250 nm)/Ni(50 nm) bi-layer metal-semiconductor-metal (MSM) Schottky contact pads are fabricated on GaN through a maskless lithography processed sample as shown in figure 2.21 (a). Also MSM contacts are fabricated by depositing Au/Ni using shadow mask technique as shown in figure 2.21 (b).

2.7.4 Oxide passivation by e-beam evaporation technique

Electron beam (e-beam) evaporation is a physical vapour deposition technique in which the electron beam produced by a charged tungsten filament is refracted by a strong magnetic field through 270° and is incident on the surface of oxide target. The e-beam evaporates the oxide material and convert the same to gaseous phase leading to deposition on the sample surface. Hind High Vacuum make e-beam evaporation system, shown in figure 2.20 (b), is capable of depositing multiple oxide layer without exposing the sample to atmosphere. The evaporation is performed under a base pressure of ~ $5\text{x}10^{-6}$ mbar to attain considerable flux at significantly low temperature and to reduce possible contaminations. Real time thickness monitoring of the deposited layer is performed with the help of a quartz crystal thickness monitor. The rate of deposition is kept at about 1-2 Å/sec. This is a low energy deposition process where the sample is kept at a considerable distance from the oxide source material resulting in better uniformity with a sharp oxide/semiconductor interface.

2.7.5 Rapid thermal annealing

Rapid Thermal Annealing (RTA) is a primary step for the formation of Ohmic contact in GaN PDs. Ti/Al/Ni/Au multi-layer contacts are deposited on the sample using thermal evaporation technique and are annealed at 850 ^oC for very short duration, typically less than 1 min. to achieve low resistance Ohmic contacts. The mechanism behind this is to form a heavily doped metal/GaN interfacial region during annealing [77]. Here, Ti enhances the rate of out diffusion of N from GaN lattice. As a result, V_N defects accumulate near the interface region which acts as shallow donor in GaN. This leads to the formation of heavily doped region near the metal/GaN interface which enhances carrier tunnelling across the junction [77].

Ecopia RTP-1200 model used in the present study is shown in figure 2.22 (a). The system works on the principle of radiation heat transfer. This is effectively achieved by lamp based heating system in which the process chamber is securely isolated to achieve optimum heating. The system can quickly increase the temperature of the sample to a very high value upto 1200 ^oC with maximum heating rate of 100 $^oC/s$ using four tungsten-halogen lamps of power 150W each with a temperature accuracy of ± 1 ^oC. The system can operate for heating samples at low pressure with an ultimate vacuum of about 10^{-3} mbar inside the chamber and also in presence of several purge gas like Argon, N_2 etc. The system is air cooled and offers fast cooling with cooling rate greater than 50 $^oC/s$ in the temperature range of 1000 to 400 ^oC.

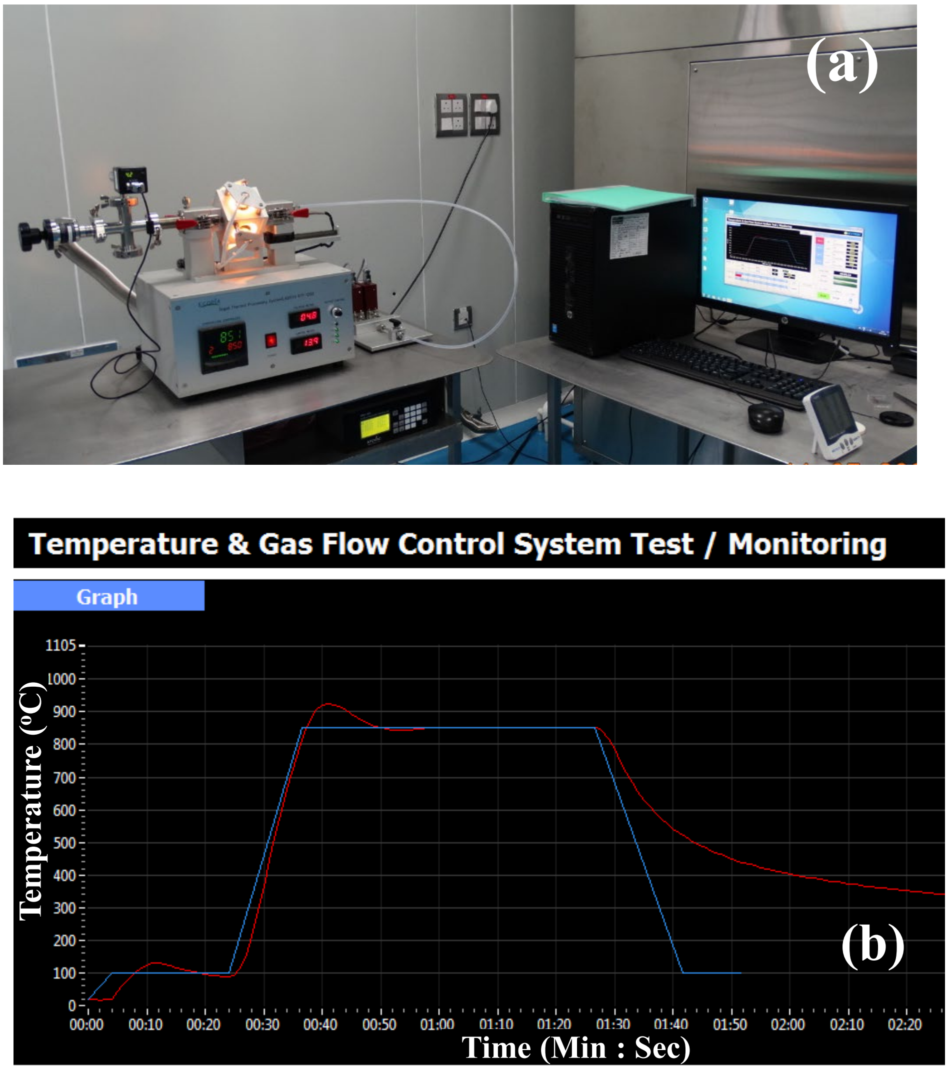

Figure 2.22 (a) Photograph of Ecopia RTP-1200 system (b) temperature profile of the RTA process where the blue line indicates the set value and the red line indicates the process value.

Accurate temperature control is possible using PID controller and the annealing temperature, time, flow rate of purge gas and other parameters are computer controlled. The temperature profile of the RTA process can be monitored online and a representative temperature profile is shown in figure 2.22 (b) for annealing GaN epi-layer at 850 °C for 45 s.

2.7.6 Reactive ion etching technique

Dry etching is an essential step for the fabrication of GaN based photodetectors with vertical device geometry. The reactive ion etching (RIE) process comprises of both chemical and physical etching mechanism to achieve anisotropic etch profile with selectivity better than wet chemical etching. Due to their inertness towards harsh chemical environments, there are no reliable wet etchants for III-nitrides. Precise pattern transfer during the fabrication of optoelectronic devices therefore involves dry etching methods which require bombardment with high energy ions for breaking relatively strong Ga-N bonds (8.92 eV/atom). A major step in the entire RIE process is the reaction between the ionized gases created in the plasma with GaN substrate surface. It produces a gaseous/volatile by product which can be removed from the chamber with the help of residual gas flow. The heavy ions in plasma react with GaN surface in a highly directional manner by applying appropriate DC bias which makes RIE a highly selective and anisotropic etching process. There are different processes occurring during the plasma formation inside plasma chamber as described next. In the first step called ionization, collision of electron with stable atoms/ molecules present in plasma chamber creates reactive positive ions and electrons. In second step, the reactive species are then diffused to the substrate surface by means of DC bias and sheath at plasma-substrate interface. These are then adsorbed on the substrate surface and take part in the chemical reaction with the sample atoms. In next step, the volatile etch product formed due to the chemical reaction is desorbed from the substrate surface. Dry etching is balanced between chemical and physical etching processes where former takes care of materials selectivity, volatile end products and reduced surface damage whereas the later provides better etching anisotropy and is insensitive to surface and geometry. Selection of reactive gas for dry etching is found to be a limiting factor. When GaN reacts with the reactive gas, the typical limiting products are the gallium-containing compounds like GaF_3 and $GaCl_3$, the latter being more volatile. This is the reason why chlorine based system is the choice for dry etching of GaN.

HIND HIVAC plasma etching system is used in the present study with 13.56 MHz RF Power Supply. The system is shown in figure 2.23. Boron tri-chloride (BCl_3) is used as the reactive gas in present study with nitrogen (N_2) additive gas which results in higher etch rate as charge exchange takes place between N_2^+ and the reactive gas species increasing the ionization efficiency of reactive gas. The reactor chamber at the extreme left has several ports as shown in figure 2.23. The chamber is having several ports for serving individual purposes. The pump port connects the chamber to the turbo-molecular pump via a throttle valve. The loadlock port isolates the reactor chamber from the loadlock chamber during the standby mode. The viewport with quartz window is attached to the chamber for observation during the sample transfer and processing. A high speed vacuum system is integrated with necessary piping, valves and interconnections, and is operated manually for high gas throughput handling and to produce high vacuum (6×10^{-8} torr) in the chamber. All the electrical components and process controls are housed in the main control unit.

Figure 2.23 Photograph of HIND HIVAC make Reactive Ion Etching Unit at RRCAT

2.8 Secondary ion mass spectroscopy techniques

In order to gain a good insight into the chemical constituents of GaN epitaxial layers, and correlating that to the electrical transport properties, Secondary Ion Mass Spectroscopy (SIMS) technique is also used during this thesis. The basic operation principle of SIMS is as follows: the secondary ions formed due to the sputtering of GaN surface with energetic primary ion beam are collected from the sample and are analysed using a mass spectrometer. SIMS measurements are performed on a IONTOF (Model: TOF-SIMS 5-100P), GmBH, Germany instrument which is shown in figure 2.24. Impurity profile as a function of time is obtained with continuous sputtering of sample surface which is further transformed into depth profile. The instrument can provide a depth profile of the possible impurities with a resolution of 1 nm. Cs^+, O_2^+ and Ar+ ions of energies between 1-2 keV are used as the primary bombarding ions and Bi^+ at 30 keV as the analysis gun for obtaining the impurity profile. Ion yields depend on the sputtering species, for example, electropositive Cs^+ ions provide higher yield for electronegative species in the specimen.

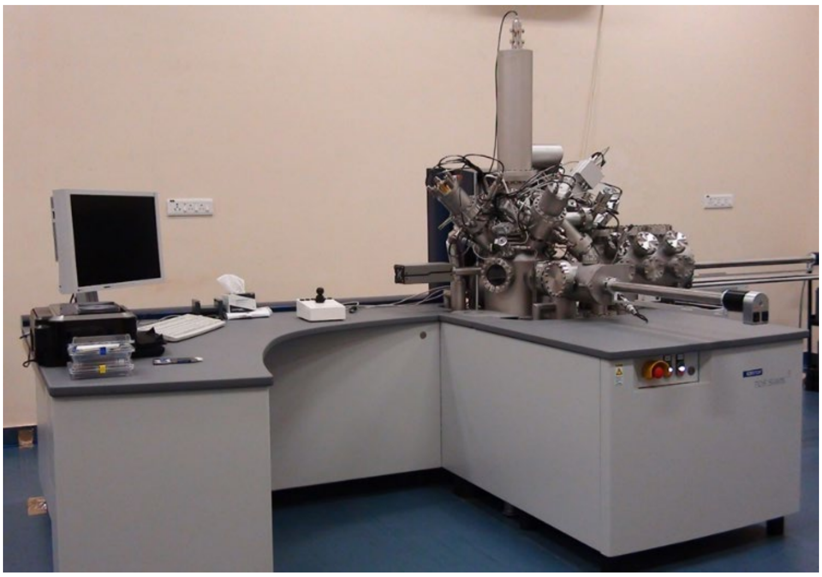

Figure 2.24 Photograph of IONTOF (Model: TOF-SIMS) SIMS instrument at RRCAT.

There are several restrictions in the SIMS measurement technique which are as follows. The detection limits for most of the impurities are between 10^{12} to 10^{16} atoms/cc. Sensitivity to several residual gases like oxygen, carbon and hydrogen which are present in the vacuum system are limited by the background. As a result, the background levels measured by SIMS for C, O and H species are of the order of low 10^{16}, high 10^{16}, and high 10^{17} cm^{-3} respectively.

Note that SIMS technique provides the depth profile of impurities and is insensitive of their electrical nature. Hence one should be careful while comparing the impurity profile in any specimen with that of the free carrier concentration measured by Hall technique. Also, the dopant species will not be detected by SIMS measurement, if it is not a foreign impurity, but rather a stoichiometric defect.

Chapter 3

Electrical Transport in GaN Epitaxial Layer and Across Au/Ni/GaN Schottky Barrier

3.1 Introduction

Hetero epitaxial growth of GaN on sapphire substrate leads to a considerably large lattice mismatch of ~ 14% [78, 79] which results in a high density of threading dislocations in the range of ~ 10^8–10^{11} cm^{-2} in GaN epitaxial layers [80, 81]. Hence, incorporation of a low temperature buffer layer [9] becomes a mandatory criteria for minimizing the density of threading dislocations in GaN. However, growth methodology of GaN buffer layers for achieving high quality thick GaN epilayer is really tricky and tiresome. As already discussed in the previous chapter, GaN epilayers grown in the indigenously developed nitride MOVPE are having large background carrier density due to the presence of a huge density of dislocations and defects making them unsuitable for device applications. In view of this, GaN epilayers or templates procured from commercial vendors are taken for further studies. Usage of such templates is generally preferred by epitaxial growers since it significantly reduces the epitaxy time of nitride heterostructures. Most of GaN templates are grown on sapphire substrates by using either HVPE or MOVPE technique. In fact, procurement of n+ GaN epitaxial layers with identical dopant density grown by either of the two techniques is possible. However, the electronic transport properties of the epilayers might vary depending upon the change in growth conditions. As a result, selection of commercial GaN epilayers might become the limiting factor in deciding the overall performance of any optoelectronic device grown on top of them. Even the dislocations originating from GaN-sapphire interface can propagate through further layers grown on top of GaN templates and can affect the current transport across the metal/GaN Schottky junction. Understanding the role of defects and dislocations in the electronic transport in GaN templates therefore becomes necessary. Availability of this knowledge can help epitaxial growers in making appropriate selection while choosing a particular GaN template for a given optoelectronic device.

In this chapter, a detailed analysis on the electronic transport of 5 μm thick GaN/Sapphire epilayers grown by HVPE and MOVPE is presented. Presence of a highly conducting interfacial region is identified in HVPE grown epilayer and influence of this layer on the electronic transport is discussed. A 2-layer model is used to extract the appropriate values of carrier concentration of HVPE grown samples from Hall measurements. Further, the impact of dislocations on the electronic transport properties of Au/Ni/GaN Schottky diodes fabricated on HVPE GaN templates is also evaluated. Role of dislocation-assisted carrier tunnelling in the temperature dependent electronic transport properties of Metal/GaN Schottky junction is investigated.

3.2 Experimental details

The first key process step for electrical transport measurements, after sample preparing and chemical cleaning, is the formation of Ohmic contacts. The purpose of Ohmic contact is to provide a current path into and out of the semiconductor with minimum resistance. Low resistance Ohmic contacts are fabricated on the GaN samples by depositing Indium (In) metal at the four corners of the sample in Van der Pauw geometry as shown in figure 3.1 and subsequent annealing at 375 ^{o}C for 30s under nitrogen ambient [70]. The Ohmic contact should have negligible resistance against the flow of current with only a minimal voltage drop, which is very small compared to the voltage drop across the active region of device. Hence it is very important to note if there are any contributions to the I-V characteristics that arise from the Indium contact, especially at low temperatures. The I-V characteristics with the two Indium contacts measured at 300 K and 70 K are shown in figure 3.1 (b) & (c). It is obvious that Indium contacts remain Ohmic over the entire temperature range irrespective of the expected changes in the series resistance of bulk GaN layer. Thereafter, Schottky contacts are fabricated on GaN by depositing Au(250 nm)/Ni(150 nm) bi-layer using thermal evaporation technique at a base pressure of 4 $\times 10^{-6}$ mbar using a metal mask of circular dots of 0.8 mm diameter.

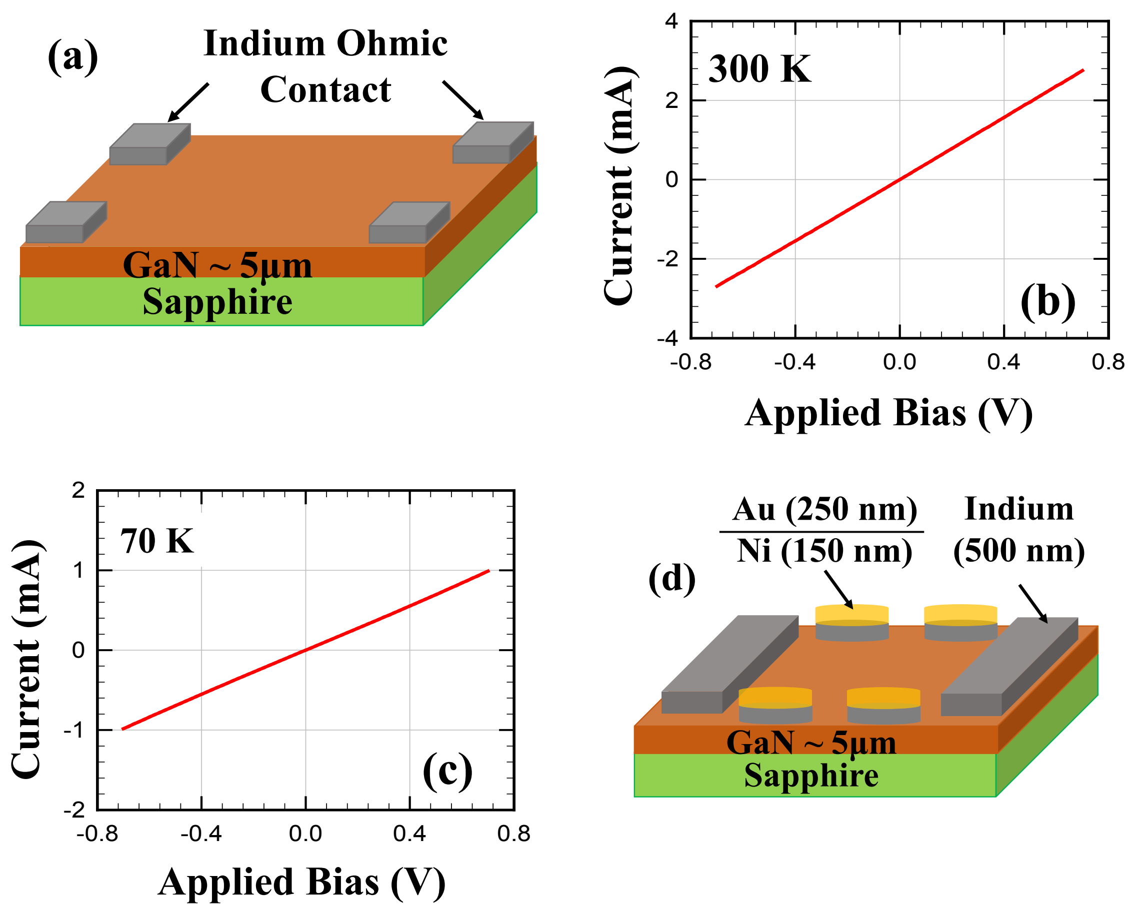

Figure 3.1 (a) Schematics layer structure of GaN with Indium Ohmic contact, I-V characteristics with Indium contacts on the sample at (b) 300 K, and (c) 70 K and (d) Schematics diagram of Au/Ni/n-GaN Schottky diodes.

Since sapphire is non-conducting, both the Ohmic and Schottky contacts are fabricated on the top GaN surface as shown in figure 3.1 (d). Note that, while selecting metal for Schottky contact with GaN, two points must be taken in to consideration. Firstly, the metal should have a single work function and it should be transparent to UV light. Keeping this in mind, Ni/ Au are chosen for the Schottky metal since they have high work function of 5.15 eV (5.10 eV) [82]. Since electron affinity of n-GaN is 4.11 eV, these metals will form higher barrier with GaN with barrier height of about 1eV. Also they are transparent to UV radiation. Also Au serve the purpose as a capping layer since Ni can get oxidize easily.

3.3 Electrical transport in GaN epitaxial layers

Temperature dependent carrier concentration data obtained from Hall and C-V measurement for sample A (HVPE) and sample B (MOVPE) GaN epilayer is shown in figure 3.2. As can be seen from the figure, the room temperature carrier concentration is found to be of the order of 10^{18} cm^{-3} which is similar to that provided by the commercial vendors. However, the carrier concentration obtained from C-V measurements is found to be about two orders of magnitude lower than the value measured by Hall technique in case of sample A as shown in figure 3.2 (a). On the contrary, sample B shows an opposite trend where the carrier concentration obtained from C-V is a bit higher than that estimated from Hall measurements. Hence, it is of great importance to understand why a two order difference in the value of n is observed when measured by Hall and C-V which are two complementary techniques. On the other hand, only a minor difference is observed in case of sample B. For better understanding of this point, one need to look at the temperature dependent Hall data plotted in linear scale in the respective insets of figure 3.2.

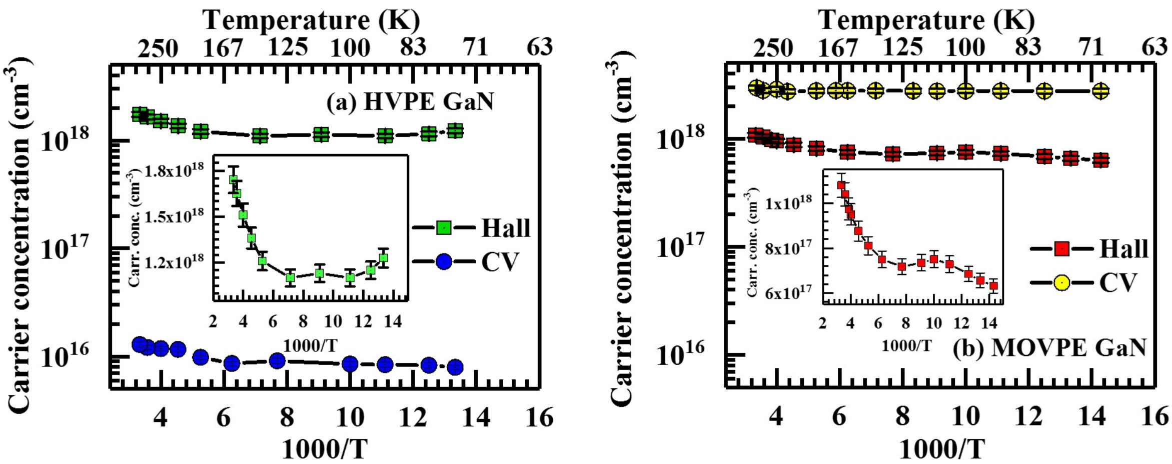

Figure 3.2 Temperature dependent carrier concentration estimated by Hall and C-V technique for (a) sample A, and (b) sample B respectively. Respective inset figures represent the carrier concentration values obtained from Hall measurements plotted in linear scale with inverse of the temperature. The data points are plotted with 5% error bars which include both instrumental and statistical errors.

As can be seen from the inset of figure 3.2 (b), the carrier concentration increases with temperature in the low temperature range below 100K for sample B and tends to saturate at a certain value (N_D-N_A) that is mainly governed by the number of electrons provided by the donor atoms. Here, N_D and N_A stand for the concentration of donors and acceptors respectively. Carrier concentration increases sharply with further rise of temperature showing an onset of the conventional intrinsic behaviour of semiconductors [19, 46]. Though, the two samples behaves in a similar fashion in the intermediate and high temperature regime, sample A shows an unusual behaviour at temperatures lower than 80K. The carrier concentration of sample A becomes almost independent of temperature in the low temperature region. In order to probe it further, the temperature dependence of electron mobility (μ) of the two samples is measured where a mobility plot for sample A is shown in figure 3.3. On cooling down process, the mobility increases with temperature up to 200 K due to the reduced phonon scattering. Afterwards the mobility starts to decrease because of a significant contribution from the ionized impurity and charged dislocation scattering.

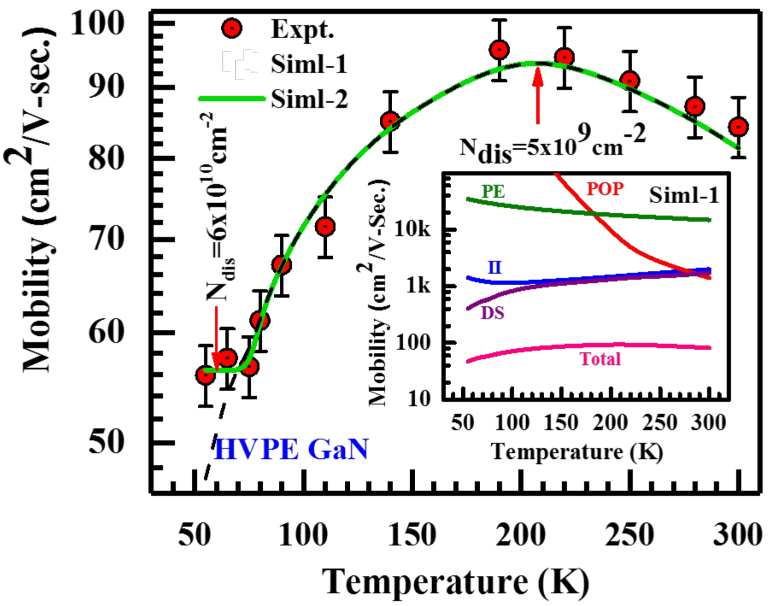

Figure 3.3 Hall mobility as a function of temperature for sample A. Siml-1 (Siml-2) shows the theoretical curve using non-degenerate (degenerate below 80 K) expressions for the mobility components. Inset shows the simulation of mobility (labelled as total) of GaN epilayers using Matthiessen's rule, the temperature dependence of various components of mobility is also shown where symbols II, POP, DIS, and PE stand for the ionized-impurity scattering, polar optical phonon scattering, dislocation scattering, and piezo-electric scattering mechanism, respectively.

However, similar to the variation of carrier concentration shown in the inset of figure 3.2 (a), even the mobility remains almost constant in the low temperature range below 80 K. On the other hand, no such observation is made in case of sample B, where mobility keeps decreasing with temperature up to 50K (not shown here). From literature survey, it is found that Look and Molnar [83] also reported a flat temperature dependence of the carrier concentration and mobility for HVPE GaN below 30 K. They argued that a flat characteristic is a signature of a degenerate layer, which is formed at the layer-substrate interface due to the clustering of impurities at dislocation sites leading to the formation of a thin impurity band at the interface [84]. Electronic nature of the impurity band depends on the donor or acceptor like behaviour of the impurities. For example, in case of unintentionally doped n-type GaN, a localized donor state is formed by oxygen impurities occupying the nitrogen site [24]. At low temperatures, charge carriers freeze at their parent donors while the energy of carriers occupying the charge dislocation sites remains independent of temperature. Interfacial region therefore provides a low resistive path for the electronic transport and dominates the low-temperature electrical characteristics in sample A [60]. In view of the occurrence of a degenerate impurity band at the layer-substrate interface, Look *et al*. [60, 83] proposed a two layer model for the extraction of carrier concentration for HVPE grown GaN epilayers from Hall experiments. However, contrary to the present observations they claimed that the carrier concentration obtained from the two methods, i.e., Hall and C-V was more or less the same [60, 83]. The two layer model of Look and Molnar [83] is therefore adopted where a degenerate layer of about 0.3µm is assumed to be formed at the layer-substrate interface as shown in figure 3.4. Such an interfacial layer has been observed in transmission electron microscopy images by several researchers [22, 28, 84, 85]. In this model, the epilayer is considered to have two layers of distinct mobility and carrier density with abrupt boundaries as schematically represented in figure 3.4. The top (bottom) layer is considered to have carrier density n_2 (n_1) and mobility μ_2 (μ_1) respectively. Then the transport properties of the top layer can be extracted from the experimentally measured Hall carrier density (n_H) and mobility (μ_H) using this model as,

$$n_H = \frac{n_{Hs}}{d} = \frac{1}{eR_s d} = \frac{\sigma_s^2/d^2}{eR_s\sigma_s^2/d} = \frac{\left(\mu_1 n_{s1}/d + \mu_2 n_{s2}/d\right)^2}{\mu_1^2 n_{s1}/d + \mu_2^2 n_{s2}/d} \tag{3.1}$$

$$\mu_H = R_s\sigma_s = \frac{\sum_i R_{si}\sigma_{si}^2/d}{\sum_i \sigma_{si}/d} = \frac{\mu_1^2 n_{s1}/d + \mu_2^2 n_{s2}/d}{\mu_1 n_{s1}/d + \mu_2 n_{s2}/d} \tag{3.2}$$

Where σ_{si} and R_{si} are thermal conductivity and Hall coefficient of i^{th} layer and the symbol 's' denotes a sheet concentration (cm^{-2}), rather than a volume concentration (cm^{-3}). Here, for plotting purpose, both the layers are normalized to the bulk thickness i.e. $n_1 = n_{s1}/d$ and $n_2 = n_{s2}/d$.

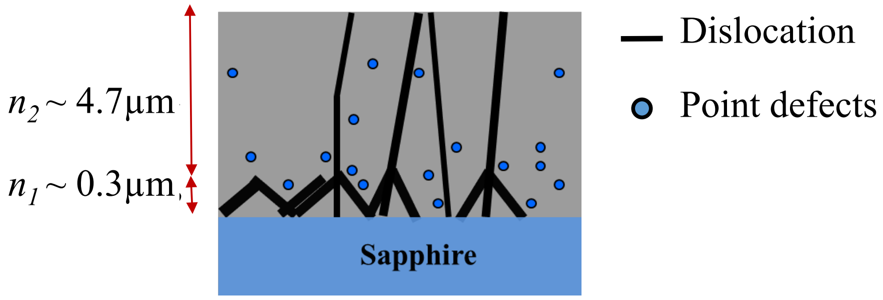

Figure 3.4 Schematic representation of the two layer model to describe the parallel layer conduction in HVPE grown GaN epilayers.

The corrected values of carrier concentration for the bulk GaN layer which are free from the influence of interface are extracted using the above equations and are plotted as function of temperature in figure 3.5 along with C-V and uncorrected Hall values. Degenerate interfacial layer affects the carrier concentration in sample A throughout the entire temperature range. Furthermore, although the corrected Hall plot has a regular shape, [46] the corrected Hall values are still 2 orders larger than the C-V values at room temperature for sample A.

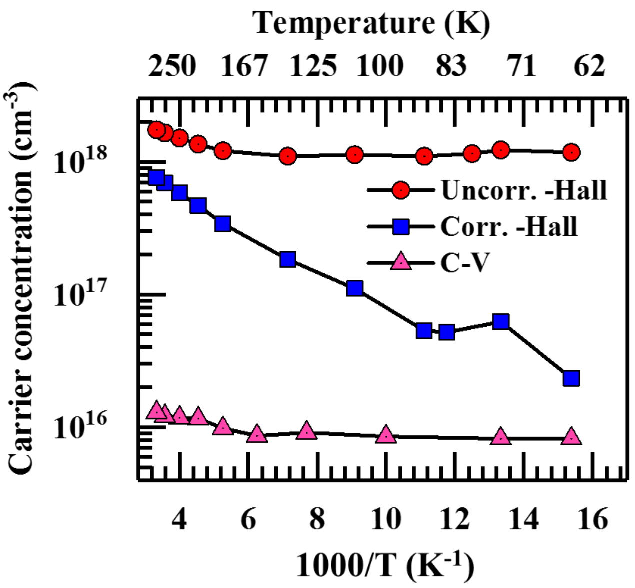

Figure 3.5 Carrier concentration values (corr-Hall) extracted by using the two layer model for sample A. For comparison, uncorrected Hall and C-V values are also plotted in the same graph.

Goetz *et al*. [85] also studied HVPE GaN epitaxial layers by Hall and C-V techniques where they found one order difference between the carrier concentrations values for 13 and 7 μm thick GaN layers. Further, a difference of ~3 orders was observed by them for 1.2 μm thick GaN layer. Nevertheless, it is not clear why one finds a reasonable match between the carrier concentration values measured by Hall and C-V techniques only under some special cases? In order to understand this point, the carrier concentration values measured by several researchers are plotted along with the values for sample A in figure 3.6. Here, trends are clearly observed where the difference between carrier concentration values measured by the Hall and C-V techniques reduces at large thickness of GaN epilayer. Degenerate layer formed at the layer-substrate interface dominates the Hall measurement results even in case of thick GaN epitaxial layers grown by HVPE. One may get a decent match only in some special cases depending upon the growth conditions [83]. It is therefore of immense interest to learn about the optimum thickness of GaN epilayer such that the effect of degenerate interfacial layer on the transport properties is minimized.

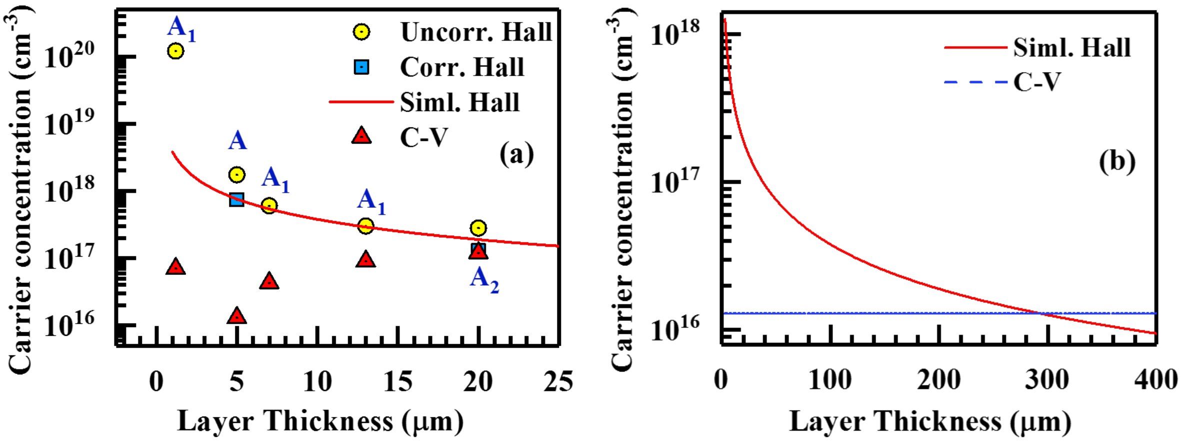

Figure 3.6 (a) Carrier concentration values obtained from conventional Hall (Uncorr. Hall), two layer model (corr. Hall), and C-V measurements are plotted as functions of layer thickness for HVPE grown GaN template where A (5 μm): this work, A_1 (1.2, 7, and 13 μm): Ref. 85, and A_2 (20 μm): Ref. 83. For comparison, carrier concentration values that are extrapolated by using the two layer model (Siml-Hall) are also shown as function of layer thickness (b) a comparison of the numerically calculated Hall values with the carrier concentration measured by C-V technique for sample A.

Keeping this in mind, we extrapolated the carrier concentration of GaN template as a function of layer thickness using the two layer model of Look and Molnar [83] by using the parameters of our sample as shown in figure 3.6 (a). The extrapolated values are surprisingly in reasonable agreement with the Hall measurements of several researchers irrespective of possible variations in the properties of interfacial layers. Furthermore, it is learnt that one need to grow ~300 μm thick GaN layer by HVPE in order to minimize the effect of interfacial layer on the transport properties as obvious from figure 3.6 (b). Beyond 300 μm thickness of HVPE GaN, the transport properties of layer are going to be determined mainly by the dopants incorporated during the epitaxial growth. Below this thickness, transport properties of epilayer will be severely limited by the dislocations lying at the layer-substrate interface. From figure 3.6 (b), it is also obvious that the limit on HVPE GaN thickness can be reduced either by increasing the dopant density or by lowering the dislocation density. Note that a decent match between Hall and C-V results was obtained by Look and Molnar [83] for ~ 20 μm thick HVPE GaN epilayer. It was due to the usage of a slightly large dopant density of 1.2×10^{17} cm^{-3} as measured by them using C-V technique, which is strongly supported by figure 3.6 (b).

From the aforementioned discussion, it can be understood that the density of threading edge and screw dislocations at the layer-substrate interface is the key parameter for determining the transport properties of HVPE grown GaN epilayers. Some information about the quantitative estimation of the dislocation density is thus desired. Dislocation density of GaN template is therefore obtained by fitting the temperature dependence of electron mobility following Matthiessen's rule where the temperature dependence of relevant scattering mechanisms, i.e., ionized-impurity (ii) scattering, polar optical phonon (pop) scattering, dislocation (dis) scattering, and piezo-electric (pe) scattering is taken into account [29, 84, 86, 87]. Inset in figure 3.3 shows the temperature dependence of various components of μ along with the total mobility. The same curve is also plotted in figure 3.3 where the fitted data is normalised with respect to the experimental value of μ for sample A at 80 K. The best fit is obtained with donor concentration (N_D) of $7 \pm 0.5 \times 10^{17}$ cm^{-3} and dislocation density (N_{dis}) of $6 \pm 0.5 \times 10^9$ cm^{-2}. The calculated mobility curve is in reasonable agreement with the experimental plot; however, it considerably deviates in the low temperature (< 80 K) regime where the contribution from the degenerate interfacial layer is dominant. Around room temperature, polar optical-phonon scattering is the dominant scattering mechanism whereas at low temperatures, the ionized-impurity scattering and scattering from charged dislocations are the dominant scattering mechanisms. The limitation of mobility simulation procedure by considering the non-degenerate scattering mechanisms in the low temperature regime is explained by Look *et al*. [84] who developed a general scattering theory for low-temperature, degenerate electrons assuming the dislocation scattering and ionized point-defect/impurity scattering as the only two important mechanisms. Following Look's model, [84] a modified curve (Siml-2) of mobility is shown in figure 3.3, which is in reasonable agreement with the experimental plot throughout the entire temperature range. The low temperature mobility is measured to be ~ 55 cm^2/V-s by taking $N_{dis} = 6 \times 10^{10}$ cm^{-2}, which is also in reasonable agreement with the published values in literature [22, 84]. This value of dislocation density is an order higher than the values estimated at temperatures higher than 80 K.

Nowadays, the usage of GaN templates for the epitaxial growth of nitrides is often preferred where device structures are grown on a template that is grown by either HVPE or MOVPE technique. The importance of the results presented here is therefore critical where dislocations might limit the charge transport in nitride devices grown on such epilayers as schematically shown in figure 3.7. One might assume that the charge transport mainly occurs via path-1 through the GaN epitaxial layer. Such an assumption is though sensible for the commercially available MOVPE grown templates but might be totally inappropriate in case of HVPE grown GaN templates.

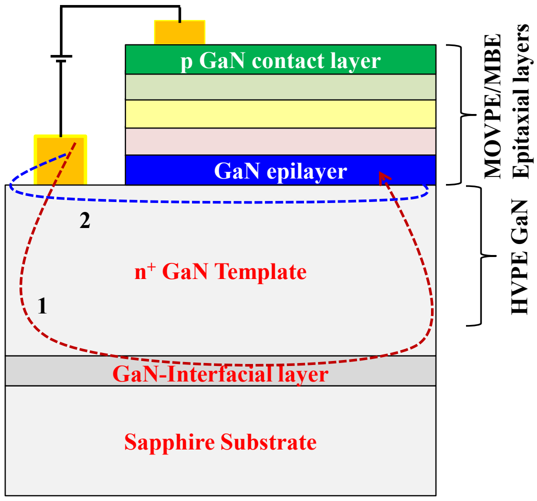

Figure 3.7 (a) Schematic layer structure of a nitride device labelled as MOVPE/ MBE grown on top of HVPE GaN templates where the conduction paths 1 and 2 describe the usual and dislocation limited current transport, respectively, p GaN and n^+ GaN represent p-type and heavily doped n-type GaN layers, respectively.

In case of commercial HVPE grown epilayers, the charge transport predominantly occurs via path-2 as schematically shown in figure 3.7, and it is going to be severely limited by the dislocations present in the degenerate layer lying at the layer-substrate interface. On the other hand, the incorporation of a low temperature buffer layer in MOVPE growth helps to minimize the number of charged dislocations at the layer-substrate interface [87]. Williamson Hall analysis of sample A and B also reveals that sample B is having one order lower dislocation density in comparison to sample A. More details about it are presented in Chapter 4 of this thesis. Note that the free carrier concentration measured by the Hall technique for sample B is little less than the apparent carrier concentration estimated by the C-V technique as shown in figure 3.2 (b), which is usual for nitride semiconductor materials. Hence, the carrier concentrations values are largely governed by the dopant density in case of commercially available MOVPE grown GaN epilayers. HVPE grown epilayers are though cheaper than the MOVPE grown ones but these might limit the performance of a device grown on top of them. Epitaxial growers therefore need to make a judicious selection of GaN epilayers for respective applications.

3.4 Electrical transport across GaN Schottky diode

Investigation of electrical transport is not only challenging in GaN epitaxial layers, but considerable complexity is also involved in carrier transport across the metal/GaN Schottky junction. Fabrication of metal/GaN Schottky contacts with large barrier height and considerably low leakage current is one of the major technological concerns in UV detector applications [88]. Realization of superior rectifying contacts with reproducible Schottky junction parameters is still a primary technical hurdle [89, 90]. It is obvious that a low values of barrier height results into a considerably high reverse leakage current, which is detrimental for the operation of GaN photodetectors.

In order to characterize the Schottky contacts, temperature dependent current-voltage measurements are performed as shown in figure 3.8. One can measure the Schottky junction parameters like the barrier height and ideality factor from such a plot. As obvious from figure 3.8, lnI-V plots are linear over a wide range of current and the I-V curves gradually shift towards higher voltage with decreasing temperature. Such behaviour of Schottky diodes is generally interpreted as an indication of TE mechanism of carrier transport [46, 72] and can be analysed with the help of the equations 2.14-2.17.

Note that there are three linear regions observed in the forward bias lnI-V curves in figure 3.8. The second linear region shown in figure 3.8 is chosen which clearly shifts towards higher voltage with lowering temperature. Another linear region seen on the lower voltage side is ignored since the conduction across Schottky barrier can have substantial recombination component in the depletion region for region 1 [below 0.2V (0.45 V) at 300K (70 K), respectively]. Furthermore, it is necessary to avoid the parasitic effects by measuring the contact resistance (Indium) and also the series resistance of the GaN epilayer, since these can severely affect the overall analysis.

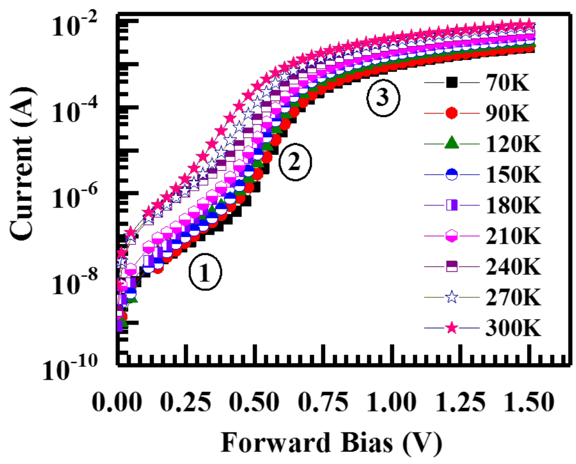

Figure 3.8 Forward bias I-V characteristics of Ni/n-GaN Schottky diode in the temperature range of 70-300K.

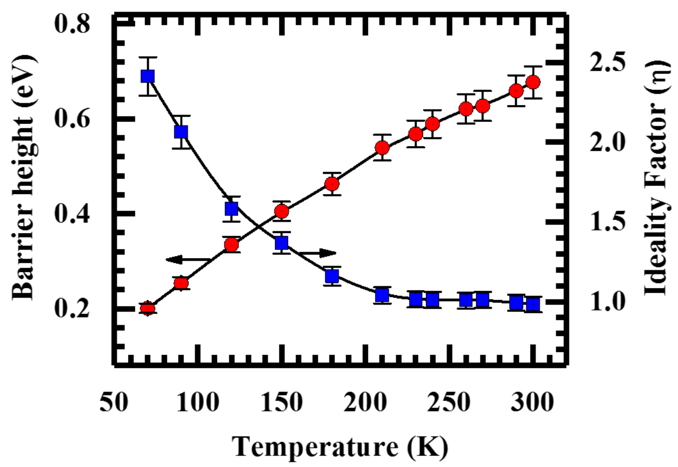

Figure 3.9 Temperature dependence of Schottky barrier height and ideality factor determined from the current-voltage characteristics. The data points are shown with 5% error bar that includes both the statistical and instrumental errors.

The values of series resistance of the GaN epilayer are found to be varying from 108 to 303 Ω in the temperature range of 300–70 K. The series resistance is measured from the linear portion of the lnI-V characteristics at high forward bias (region 3) shown in figure 3.8. Although lnI-V is plotted in figure 3.8, the series resistance of GaN is measured from linear I-V plots. The average voltage drop across the bulk GaN remains below 1% (2%) of the applied voltage at 70K (300 K) temperature, respectively. Furthermore, the value of Indium contact resistance is expected to be negligible in this sample. That is why, the contribution of bulk GaN resistivity and contact resistance is ignored in the evaluation of junction parameters. We measured the room temperature values of barrier height and ideality factor as 0.67 eV and 0.98, respectively. It is obvious that the measured value of barrier height is much lower than the Schottky-Mott barrier height of Ni/ n-GaN contact [82]. A similar deviation of the measured values of Schottky junction parameters from the ideal characteristics is already reported by several authors [82, 91]. For example, Guo *et al*. [92] has reported a 0.88 eV barrier height of the Ni/GaN Schottky diode at room temperature whereas the same is reported to be only 0.66 eV by Yu *et al*. [91]. To investigate this point further, the temperature dependence of barrier height and ideality factor of Ni/n-GaN Schottky contacts is performed and the data is shown in figure 3.9.

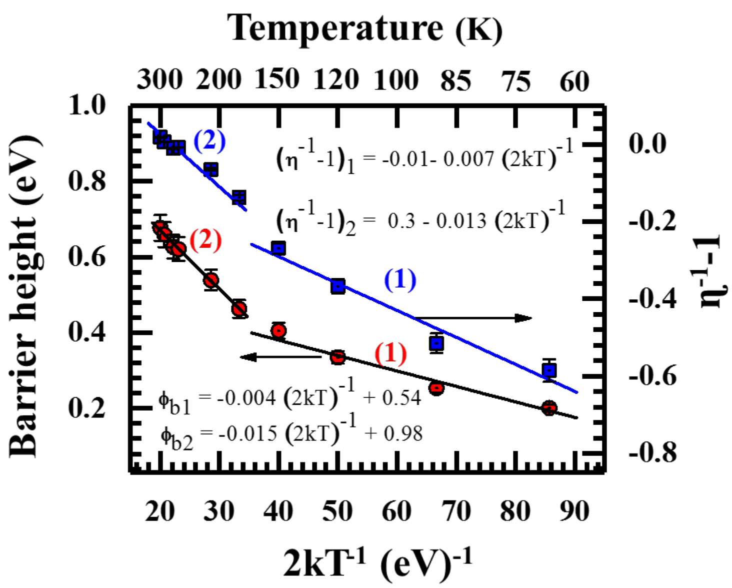

Figure 3.10 Apparent barrier height (filled squares) and ideality factor (filled triangles) versus 1/(2kT) for the Ni/n-GaN Schottky contacts, where straight lines show a fit of the experimental data according to double-Gaussian distribution of barrier height. The data points are shown with 5% error bars that include both the statistical and instrumental errors. Labels “1” and “2” correspond to the two current transport mechanisms (channels), namely, the dislocation-assisted tunnelling and TE, respectively.

Such an anomalous variation of Schottky junction parameters is already reported by several researchers, [89, 93-96] where it has been associated with the presence of non-uniform distribution of barrier height. Under such conditions, electronic transport across the Schottky barrier is described by considering TE as the primary conduction mechanism. Here, a Gaussian distribution of apparent barrier height is assumed which is given by the following expression; [93, 95, 96]

$$\phi_{ap} = \overline{\phi}_{bo} - \frac{\sigma_{so}^{2}}{2kT} \tag{3.3}$$

where $\overline{\phi}_{bo}$ is the mean barrier height at zero bias, σ_{so} is the zero bias standard deviation of the barrier height distribution. Even in case of Au/n-GaAs Schottky diodes, where inhomogeneity issues are less dominant compared to GaN, such a distribution of barrier height is recently report by Özerli *et al.* [97]. However, the apparent barrier height is always found to be lower than the mean barrier height since the lateral length scale of barrier inhomogeneity and the interaction among adjacent regions having different barrier heights is ignored.

Under this model, the temperature dependence of apparent ideality factor (η_{ap}) is given by [93, 94];

$$\left(\frac{1}{\eta_{ap}} - 1\right) = -\rho_2 + \frac{\rho_3}{2kT} \tag{3.4}$$

where ρ_2 and ρ_3 are the voltage coefficients of mean barrier height and standard deviation respectively. Hence, we plot the measured ϕ_{ap} and $(1/\eta_{ap}-1)$ versus 1/2kT as shown in figure 3.10. It is obvious that the variation of ϕ_{ap} and $(1/\eta_{ap}-1)$ cannot be fitted with a single straight line. We rather need to consider two straight lines of different slopes to fit the data in two temperature regimes where the transition occurs at ~170 K.

The intercept and slope of ϕ_{ap} versus 1/2kT plot gives the values of $\bar{\phi}_{bo}$ and σ_{so} as 0.54 ± 0.02 eV and 0.063 ± 0.002 eV in the temperature range of 70-170 K (distribution 1) while 0.98 ± 0.06 eV and 0.122 ± 0.004 eV in the temperature range of 170-300 K (distribution 2) respectively. Such a situation is often encountered by researchers [93, 94, 98] where it is interpreted by assuming TE as the main conduction mechanism with two Gaussian distributions of barrier height over different temperature ranges. However, such an interpretation might not work in GaN where charged dislocations are expected to affect the conduction mechanism over the entire temperature range [87]. Under such cases, thermionic field emission (TFE) mediated by threading dislocations might play a critical role in current conduction especially in the low temperature range where the contribution of thermionic emission is feeble. Therefore, the two sets of $\bar{\phi}_{bo}$ and σ_{so} parameters for Ni/n-GaN Schottky diode might be related with the two different conduction mechanisms dominating in the respective temperature ranges. In fact, Yıldırım *et al.* [93] have already indicated that the two values of barrier height, as measured by us, might correspond to the two current transport mechanisms namely TE and TFE mediated by trap-assisted tunnelling which dominate in high and low temperature regime respectively [93]. It is well known that GaN epilayers have a high dislocation density which can be of the order of 10^{10}cm^{-2} and a large fraction of those reach the sample surface. It is already discussed in the previous section that the charge transport in HVPE grown GaN epilayers is significantly affected by such dislocations where the current conduction is dominated by the charged dislocations at low temperatures [87]. One cannot completely discard their role in the conduction process even at room temperature. The conduction occurs via these dislocations where a large fraction of charge carriers travel via a thin layer lying at the layer-substrate interface [87]. It is plausible that this process dominates the evaluation of barrier height of Ni/n-GaN Schottky diodes at low temperatures and the same is labelled as channel-1 in figure 3.10. Another process that governs the values of barrier height in the high temperature range is labelled as channel-2 in figure 3.10. Note that the measured value of mean barrier height for channel-2 is 0.98 eV which is close to the Schottky-Mott barrier height of Ni/n-GaN contact. Even the value of ideality factor at room temperature is close to unity as shown in figure 3.10. Hence, it is confirmed that the channel-2 is mainly governed by the thermionic emission of electrons across the Ni/n-GaN Schottky barrier. Furthermore, a continuous lowering of the apparent barrier height with falling temperatures within the temperature range of 200-300K can be understood by considering a Gaussian distribution of barrier height as given by Eqn. (3.6). On the other hand, it is learnt that the channel-1 might be responsible for the observation of large barrier inhomogeneity in Ni/n-GaN Schottky diodes. Note that the value of ideality factor is relatively large for channel-1 as shown in figure 3.10. The charged dislocations reaching the sample surface might enhance the tunnelling probability of carriers across the Schottky barrier. Though this kind of tunnelling mechanism is not well known, the phenomenon can still be quantified by estimating the characteristic tunnelling energy (E_{00}) from the current-voltage characteristics. The forward I-V characteristic in presence of tunnelling can be expressed as [54, 93];

$$I_F = I_{SFE}\left[\exp\left(\frac{qV}{E_o}\right)\right] \tag{3.5}$$

where I_{SFE} is the saturation current and the parameters E_o, and forward ideality factor η_F are given by;

$$E_o = E_{oo}\coth\left(\frac{E_{oo}}{kT}\right) \tag{3.6}$$

$$\eta_F = \frac{E_{oo}}{kT}\coth\left(\frac{E_{oo}}{kT}\right) \tag{3.7}$$

Here the characteristic tunnelling energy E_{00} is defined as,

$$E_{oo} = E_{oo}(N_D) = \frac{\hbar q}{2}\sqrt{\frac{N_D}{m^* \varepsilon_s \varepsilon_0}} \tag{3.8}$$

where $\hbar$ is Plank's constant, N_D is the donor density, m^* is the effective mass, ε_s is the dielectric constant of GaN, and ε_0 is the permittivity of vacuum. Effect of tunnelling on the carrier transport across the Schottky barrier can be understood by fitting the temperature dependence of ideality factor with equation 3.7 as shown in figure 3.11.

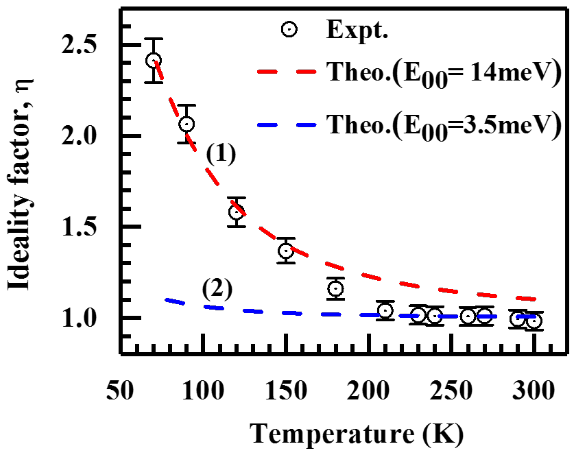

Figure 3.11 Ideality factor plotted as a function of temperature. The red and blue dotted lines show the numerically calculated curves using the two values of characteristic tunnelling energy (E_{00}). Curves "1 and 2" correspond to the two current transport mechanisms, namely, trap assisted TFE and TE, respectively. The experimental data points are shown with 5% error bars that include both the statistical and instrumental errors.

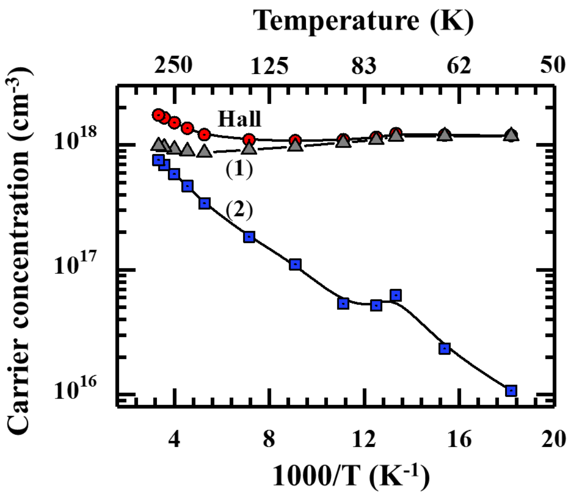

Figure 3.12 Carrier concentration values obtained from conventional Hall measurements (filled green squares) and those estimated using the two layer model of Look and Molnar (Ref. 83) are plotted with temperature. Curves "1" and "2" correspond to the carrier concentration values estimated for the thin defective layer lying at the layer-substrate interface and the bulk n-GaN layer, respectively.

One can easily estimate the value of E_{00} from such an exercise. However, similar to the observations made in figure 3.10, the ideality factor cannot be reproduced by using a single component. One needs to consider two components in equation 3.7 with two different values of E_{00} to represent the temperature dependence of ideality factor over the complete temperature range as shown in figure 3.11. The two values of E_{00} are estimated to be 14 ± 0.5 and 3.5 ± 0.5 meV corresponding to the two parallel conduction channels, as described earlier, that dominate over the temperature ranges of 70-170 K and 170-300 K respectively. It is of considerable interest to correlate the two values of E_{00} with some physical mechanisms that can be associated with the electronic transport of carriers across the Ni/n-GaN Schottky diodes. More information about the two electronic transport mechanisms can be obtained by estimating the dopant concentration of GaN epilayer using equation 3.8 and then by comparing the same with the carrier concentration values obtained from Hall experiments. Such a comparison for Ni/n-GaN Schottky diode is not available in literature. Using equation 3.8, the two values of E_{00} corresponds to the dopant concentration of 1.3×10^{18} and 8×10^{16} cm^{-3} for the low and high temperature regime respectively. In order to corroborate this information, temperature dependent Hall measurements are performed on the same sample for extracting the carrier concentration of GaN epilayer and the results are summarised in figure 3.12. Since the Hall measurements reveal highly conducting GaN layer of n-type, the dopant density can be inferred from the saturation region where $N_D \approx N_D\text{-}N_A \approx n$ by considering the complete ionization of shallow donors. Following this approach, the dopant density is found to be ~ 1.2×10^{18} cm^{-3} which provides the value of E_{00} as 13.3meV using equation 3.8.

It is in reasonable agreement with the value of E_{00} extracted from the forward bias I-V characteristics in the low temperature regime. In this temperature range, the dislocation-assisted tunnelling of carriers is expected to dominate the current transport across the Ni/n-GaN Schottky diode. However, the measured value of E_{00} for the other component (channel-

2) in figure 3.11 is only 3.5 meV which cannot be supported by the Hall results. A careful observation of the Hall data in figure 3.12 reveals that the dislocations are contributing in the electronic conduction at low temperatures. Note that the carrier concentration slightly increases with cooling below ~100K and thereafter becomes almost flat in the low temperature region. As already reported in the section 3.3, the values of carrier concentration and mobility of HVPE grown GaN epitaxial layers remain constant below 80K [87] which is a known signature of a degenerate layer that is formed at the layer-substrate interface. Curve-2 represents the temperature dependent bulk carrier concentration obtained from two-layer model as already shown in figure 3.5. Following this approach, the dopant density of bulk GaN is estimated to be ~ 6×10^{16} cm^{-3} by considering the saturation region in curve-2 of figure 3.12. The dopant density of this magnitude provides a value of E_{00} as 3 meV following the equation 3.8. It is in reasonable agreement with the value E_{00} for the channel-2 in figure 3.11. Hence, Hall measurements are in excellent corroboration with the forward bias I-V-T experiments over the complete temperature range. However, it is necessary to understand why the carrier density increases by about an order for chanel-2 above 100K in figure 3.12. More than one reasons are responsible for such an observation. The first one is related to the point defects that can provide free carriers at elevated temperatures. Second factor is related to some other donors which might be activated at higher temperatures. For GaN, the presence of more than one donor is already reported by several researchers [85, 99]. However, it is reasonable to assume that the majority of shallow donors that contribute in the current transport across Schottky diode are ionized at about 100K.

Another option to validate the proposed model is to obtain the value of carrier density from the C-V measurements which can also be used to estimate the values of E_{00}. As already shown in figure 3.2, the measured values of N_D vary between 1-2 $\times 10^{16}$ cm^{-3} over the entire temperature range of 70-300K. It provides a value of E_{00} about 2 meV which is a bit lower than the value estimated from the Hall results. This is because the ionized dopant density obtained from C-V is measured at the edge of depletion width which is very close to the GaN surface, whereas N_D obtained from channel-2 of Hall data is averaged over the entire bulk GaN layer. As already discussed in the previous section that the layer quality improved with increasing thickness of bulk layer, the N_D obtained from C-V shows little less value than that from Hall.

These results suggest that the magnitude of current passing through the Schottky barriers at low temperatures is mainly governed by the TFE of carriers mediated by the threading dislocations which propagates to the sample surface from the GaN-sapphire interface as shown schematically in figure 3.13 (a). This is the mechanism which governs the large variation of barrier height and ideality factor especially at low temperatures. In the bulk of GaN materials, carriers tend to freeze at their parent donors at low temperatures which therefore yield a high value of E_{00} ~ 14 meV, thereby confirming the involvement of a conduction mechanism which is significantly different from the TE model. The dominance of such a conduction mechanism through Hall technique as discussed in the previous section 3.3 is hereby confirmed by performing I-V-T measurements on Ni/n-GaN Schottky diodes. On the other hand, the value of E_{00} switches to ~3 meV once the temperature exceeds 170K which indicates about the dominance of TE at elevated temperatures as obvious from figure 3.11. Thus, the present analysis suggests that the dislocation-assisted tunnelling of carriers (Channel-1) strongly influences the temperature dependence of parameters of Ni/n-GaN Schottky diodes at low temperatures. TE of carriers (Channel-2) on the other hand dominates the high temperature I-V characteristics as clearly shown in figure 3.11. Though the dominant conduction mechanisms above 170K is TE but the TFE mediated by dislocation assisted tunnelling cannot be completely ignored in this range. It also affects the value of apparent barrier height which might be another reason behind a continuous variation of barrier height between 200 -300 K.

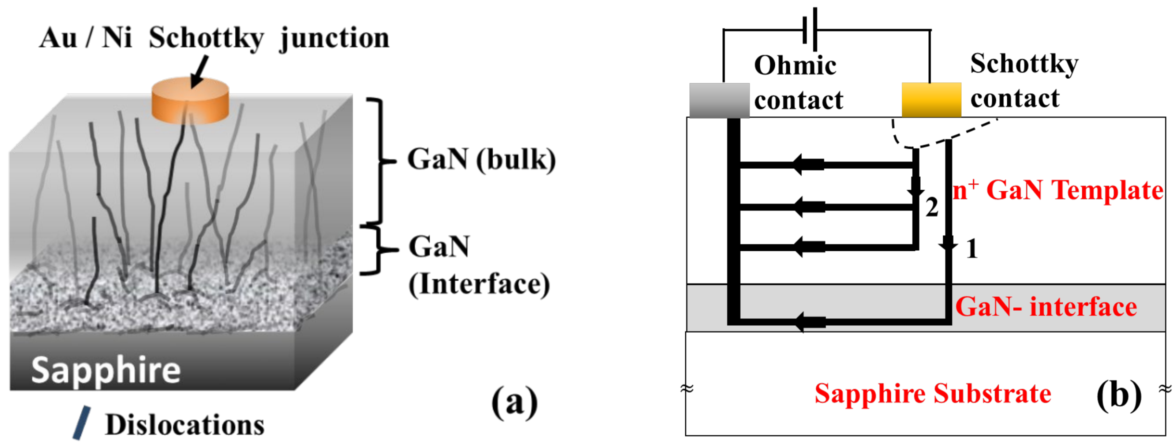

Figure 3.13 (a) Schematic diagram to describe the carrier transport across the Ni/n-GaN Schottky barrier through the charged dislocations leading up to the sample surface (channel-1) and through the bulk of the GaN epitaxial layer (channel-2). (b) Schematic diagram showing the parallel conduction paths for the Ni/n-GaN Schottky diode.

More insight of the parallel conduction mechanisms across Ni/n-GaN Schottky diodes can be obtained from figure 3.13 (b) where the involvement of two conduction channels is schematically shown. Under forward bias, electrons are pushed from Ohmic contact to the GaN layer where the current flows along the two parallel conduction paths as shown in figure 3.13 (b). After reaching the edge of the depletion region, the electrons will travel across the barrier due to either the TE or TFE mediated by dislocation assisted tunnelling. However, it is obvious that the carriers travelling to the Schottky contact via the dislocation assisted tunnelling, channel-1 of figure 3.13 (b), will traverse through the least resistance path. Hence, the observation of a large value of ideality factor and a low value of barrier height in Schottky diodes confirm the presence of a large number of charged dislocations in GaN layer which might encourage the growers to further improvise the interface quality of GaN/Sapphire epilayers.

3.5 Conclusion

In conclusion, GaN templates grown by HVPE and MOVPE techniques are investigated by using complementary Hall and C-V techniques. It is observed that the carrier concentration measured by Hall for HVPE grown epilayers is two orders larger than the value provided by the C-V technique. Such a large difference in carrier concentration values is associated with the formation of a degenerate layer at the layer-substrate interface, which consists of a large density of threading screw and edge dislocations. A two layer model is also used to extract the appropriate values of the carrier concentration of HVPE grown epilayers from Hall data. It is learnt that there exists a critical thickness of HVPE GaN epilayers below which the electronic transport properties of layers grown on top of them are severely limited by the interfacial charged dislocations. On the contrary MOVPE grown samples are found to be free from such limitations, which makes them attractive for device fabrication. Further, the impact of dislocations on the electronic transport properties of Au/Ni/GaN Schottky diodes fabricated on HVPE GaN template is evaluated. It is found that one needs to consider the activation of two donors operating in the two separate temperature ranges for understanding the temperature dependence of ideality factor. The two donors correspond to the fundamental mechanisms associated with 1) TE of carriers from bulk donors that dominates at high temperature, and 2) TFE associated with charged dislocations that dominates at low temperature. The understanding developed in this chapter is expected to be useful in the development of GaN PDs, especially for the cases, when charge transport is severely affected by the presence of a degenerate layer at GaN/Sapphire interface and dislocations lines pierce through the Schottky junction to enable the tunnelling of carriers.

Chapter 4

Fabrication of Metal-Semiconductor-Metal GaN Photodetectors

4.1 Introduction

III-nitride based optoelectronic devices such as photodetectors (PDs) and light emitters are becoming increasingly popular due to their wide range of applications in strategic sectors, medical science, astronomy and commercial domain [1, 4, 100, 101]. Due to their solar blind nature, radiation-resistance and thermal stability, these devices offer several advantages over conventional photomultiplier tubes and Si-based ultraviolet (UV) detectors, for example less operational complexities including the elimination of various filters [102-104]. Several types of GaN-based PDs, such as p-i-n diode [105], Schottky barrier [106], p–n junction [107] and metal–semiconductor–metal (MSM) [108] PDs, have been reported during the past few years. Among them, MSM PDs are generally preferred due to their fabrication simplicity and easy integration with the field-effect-transistor based technology [109]. Although a remarkable progress has been made in the GaN material growth and device fabrication technology, there are several issues inherent to nitride based PDs which needs further investigations. For example, high-performance PDs demand a low dark current across the device since it sets a limit on the smallest measurable signal for a PD [110]. However, the mechanisms responsible for the generation of leakage current in GaN based UV PDs are still under debate. Extensive work is currently being carried out for identifying the origin of leakage current in GaN, where several possible sources like surface and interface traps [111-113], point defects [114-116] and threading dislocations are proposed to be the major contenders [90, 117, 118]. Among them, threading dislocations are assumed to be the primary source of leakage current in GaN. The influence of dislocations in the electronic conduction in GaN epilayers is already discussed elaborately in the previous chapter. Researchers have reported that screw dislocations cause a sharp increase in the dark current of GaN UV PDs [119]. From scanning capacitance microscopy, Iucolano *et al*. [95] had shown that the core of threading dislocations behave as highly n-type doped regions. Due to this, a local lowering of Schottky barrier height takes place in those regions which triggers the onset of TFE of carriers across the junction leading to a considerable increase in leakage current. Moreover, several kinds of point defects such as N and/or Ga vacancies, interstitial and substitutional defects are also present in GaN, which along with threading dislocations are understood to make a substantial contribution to the leakage current [114-116]. Another key figure-of-merit of GaN PDs is their response to UV radiation. However, it is already known that threading dislocations considerably increase the recombination probability of photo-generated electron-hole pairs which leads to a significant reduction of the responsivity of GaN-based UV PDs [116]. Similar to their adverse effect on the leakage current, point defects are also known to reduce the photocurrent of GaN PDs by capturing the photo generated carriers [116]. Threading dislocations and point defects are expected to play a critical role in determining the overall performance of GaN UV PDs where a low density is generally preferred.

With the knowledge of the electronic transport properties of GaN epilayers discussed in the previous chapter, an in-depth characterization of GaN MSM UV detectors is carried out in this chapter with an aim of understanding the role of threading dislocations and point defects in device performance. MSM photodetectors are made on MOVPE and HVPE GaN epilayers for comparison purpose. The impact of threading dislocations and point defects on the performance of MSM UV photodetectors is carefully estimated by performing systematic electronic transport measurements in this chapter. Key factors affecting the performance of UV

PDs and associated charge transport mechanisms are discussed by comparing the characteristics of devices fabricated on GaN epilayers grown by HVPE and MOVPE techniques.

4.2 Device fabrication details

GaN MSM UV detectors are fabricated on GaN epilayers grown by HVPE (sample A) and MOVPE (sample B) techniques. The samples are obtained by cutting the GaN templates into square pieces of 5×5 mm^2 size. Proper organic cleaning of the samples is carried out as already mentioned in the section 2.7.1 of chapter 2. Further, GaN MSM UV PDs are fabricated by the two step mask-less photolithography [76, 120]. A schematic diagram showing the device geometry is given in figure 4.1 (a) along with a cross-sectional view in figure 4.1 (b).

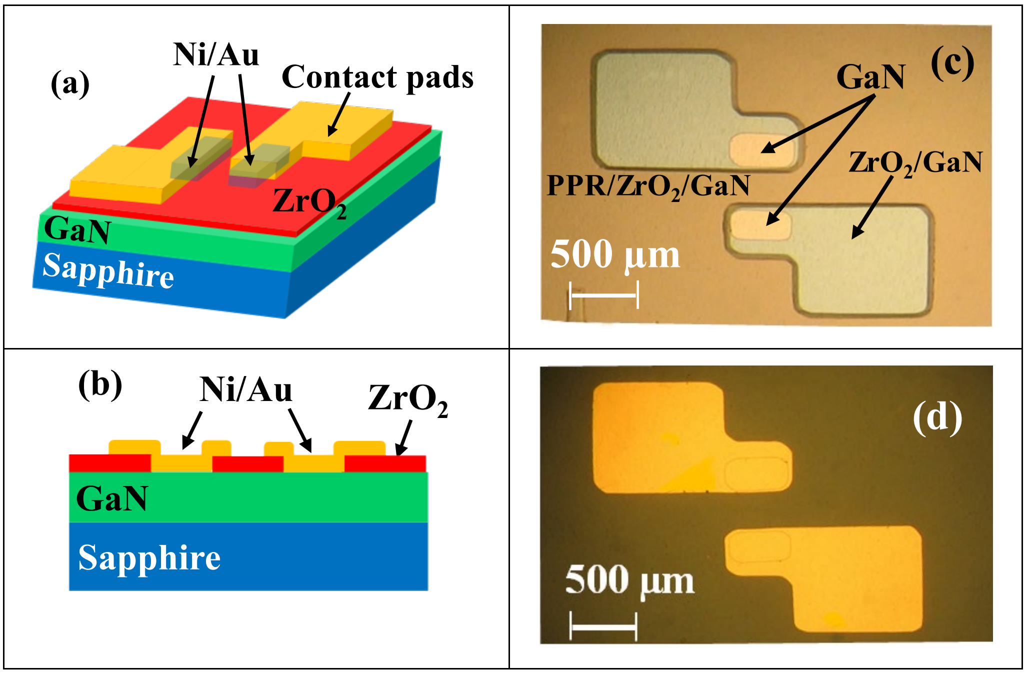

Figure 4.1 (a) Schematic diagram showing the device structure, (b) cross-sectional view of the device, (c) optical microscopic image of the device after second step of photolithography prior to metallization where PPR stands for the positive photoresist, and (d) final device subsequent to the metallization and lift-off procedure.

Here, in the first step, a ZrO_2 oxide layer of 80 nm thickness is deposited by electron-beam evaporation under a base pressure of 5×10^{-6} mbar. The oxide layer is then patterned by photolithography and selectively etched by buffer HF solution for fabricating fingers of 500 μm length and 250 μm width along with a separation of 300 μm as shown in figure 4.1 (c). In second step, realignment and patterning is performed again for metallization and lift-off to obtain the final device with Ni/Au metal contact connecting the active device area with the large area contact pads on oxide layer as shown in figure 4.1(d). The oxide layer serves for the purpose of contact isolation and surface passivation.

4.3 Role of dislocations and point defects on detector performance

In order to investigate the role of threading dislocations and point defects on the device performance, it is necessary to evaluate the crystalline properties of the two GaN samples. The density of dislocations in epitaxial layers can be estimated by HRXRD technique, which is usually preferred since one can access the layer quality rather quickly by simply comparing the full width at half maxima (FWHM) of corresponding diffraction peaks of respective samples. All types of dislocations are supposed to broaden the diffraction peaks and a low value of FWHM of HRXRD pattern is considered to be an evidence of good crystalline quality. FWHM of HRXRD patterns for (002) and (102) reflections of the two samples are listed in Table 4.1, where a low value is recorded for sample B. The values of tilt and twist are obtained from Williamson Hall analysis of ω-scans of symmetric (0 0 l) and skew symmetric (where either h or k ≠ 0) set of (h k l) reflections and the corresponding values of dislocation density (N_D) are obtained by using the following relation [64, 66,120, 121]:

$$N_D = \frac{\beta^2}{4.35\, b^2} \tag{4.1}$$

where β is the tilt (twist) value for screw (edge) dislocations and b is the Burgers vector length (b_{screw} = 0.5185 nm, b_{edge} = 0.3189 nm). The density of screw and edge dislocations in the two GaN samples estimated from the Williamson Hall analysis is also shown in Table 4.1. It is found that the density of screw and edge dislocations is slightly higher for sample A, which confirms that the crystalline quality of sample B is better.

Figure 4.2 shows the photoresponse of MSM PDs fabricated on both the samples over the spectral range of 300–390 nm at an applied bias of 4V. It is surprising to see that the peak spectral response is enhanced by ~3 times for sample A in comparison to sample B. It is established that the edge dislocation lines provide acceptor traps and form negatively charged scattering centres in n-GaN [122]. It is reasonable to believe that the recombination probability of photo generated electron-hole pairs can be enhanced by the dislocation-induced acceptor levels which leads to a reduction in the responsivity of GaN PDs. Therefore, it is obvious to expect that the responsivity of GaN-based PDs should improve by reducing the dislocation density. Contrary to this, a low value of responsivity is recorded for sample B despite its low dislocation density as obvious from figure 4.2.

Table 4.1. Microcrystalline properties of the two samples estimated from HRXRD measurements.

Sample	FWHM (arcsec)		Tilt (Degrees)	Twist (Degrees)	Screw dislocation density (N_{SD}) in cm^{-2}	Edge dislocation density (N_{ED}) in cm^{-2}
	(002)	(102)				
A	346	700	0.08	0.25	1.65×10^8	4.3×10^9
B	252	363	0.06	0.13	8.76×10^7	1.16×10^9

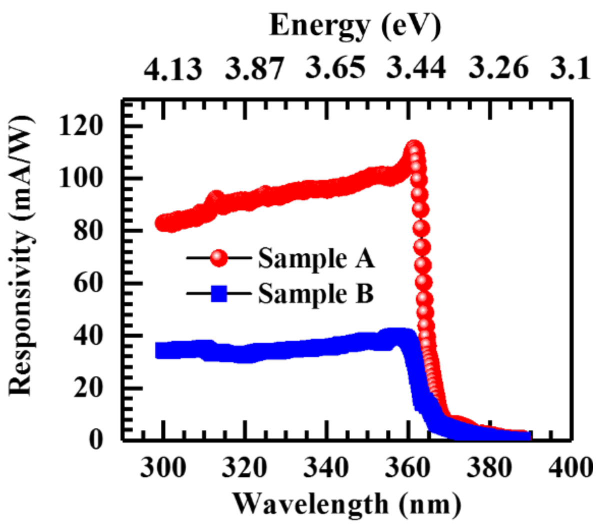

Figure 4.2 Room temperature spectral response of GaN MSM PDs.

It seems plausible that the factors other than the dislocation density might determine the magnitude of photo-response in these devices. In order to gain more information, transient response of the two devices is recorded as shown in figure 4.3 and the rise and decay curves were fitted using the exponential rise and decay equations as given below [123] ;

$$\text{Rise equation}: I_r(t) = I_{\text{dark}} + A\left[1-\exp\left\{\frac{-(t-t_{\text{on}})}{\tau_{r1}}\right\}\right] + B\left[1-\exp\left\{\frac{-(t-t_{\text{on}})}{\tau_{r2}}\right\}\right] \quad (4.2)$$

$$\text{Fall equation}: I_f(t) = I_{\text{dark}} + A\left[\exp\left\{\frac{-(t-t_{\text{off}})}{\tau_{d1}}\right\}\right] + B\left[\exp\left\{\frac{-(t-t_{\text{off}})}{\tau_{d2}}\right\}\right] \quad (4.3)$$

where I(t) is the photocurrent at time t, I_{dark} is the dark current, A and B are scaling constants, τ_r (τ_d) are the time constants, and t_{on} (off) is the time of switching the lamp on (off).

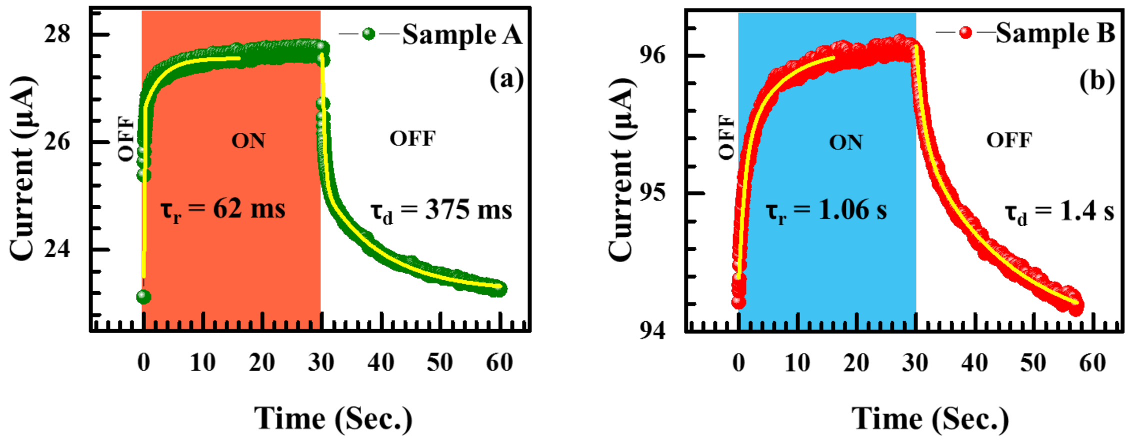

Figure 4.3 Transient photoresponse of GaN MSM PDs made on a) Sample A, and b) Sample B, where yellow solid lines represent an exponential fit of corresponding part of the experimental data.

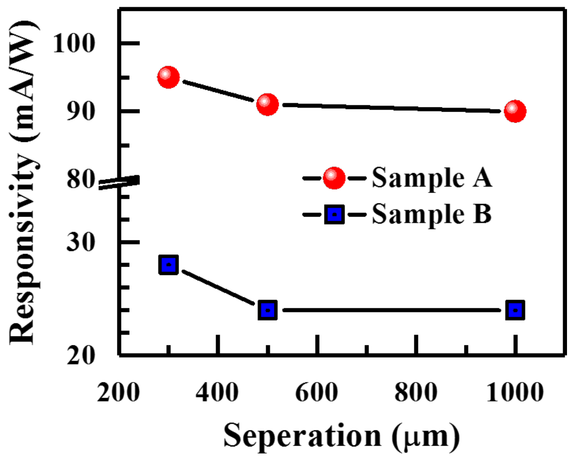

Figure 4.4 Responsivity of GaN MSM PDs plotted as a function of separation between the two contacts, error bars in the data are smaller than the size of symbols.

A fast transient response of PDs made on sample A is observed where the faster component of rise (fall) times of 62 ms (375 ms) are measured in comparison to 1.06 s (1.40 s) for sample B. It therefore confirms that the devices made on sample A are superior. Also the responsivity remains nearly the same for both the samples with varying separation over a range of 300 to 1000 μm between the contact pads as shown in figure 4.4. It therefore confirms that the photo response of HVPE based PDs (sample A) is few times larger than that of the MOVPE based devices (sample B), irrespective of the device size.

It is important to know if the observations made so far are consistent as a function of applied bias and excitation power. The outcome of such an exercise is shown in figure 4.5. The responsivity increases linearly with applied bias up to 2.5 V and tends to saturates thereafter as shown in figure 4.5(a). Such a behaviour of GaN PDs in already known [124, 125]. Further, the photocurrent increases linearly with optical power at a constant bias under low excitation conditions, which leads to a constant value of responsivity as shown in figure 4.5(b). Similar trends are already reported by other researchers under low power excitation conditions [126]. It is obvious that sample A has a larger responsivity irrespective of the value of applied bias or optical power. Moreover, the ratio of responsivity of two samples remains more or less constant. It is therefore obvious that the PDs made on sample A demonstrate better device characteristics under all the operating conditions. It indicates that the factors other than the dislocation density play a critical role in governing the performance of GaN MSM PDs. In order to pinpoint the fundamental reasons behind the high performance of PDs made on HVPE GaN epilayers (sample A), detailed electronic transport measurements are performed on the two samples. It is generally understood that a low screw dislocation density will lead to a lower dark current in PDs [118].

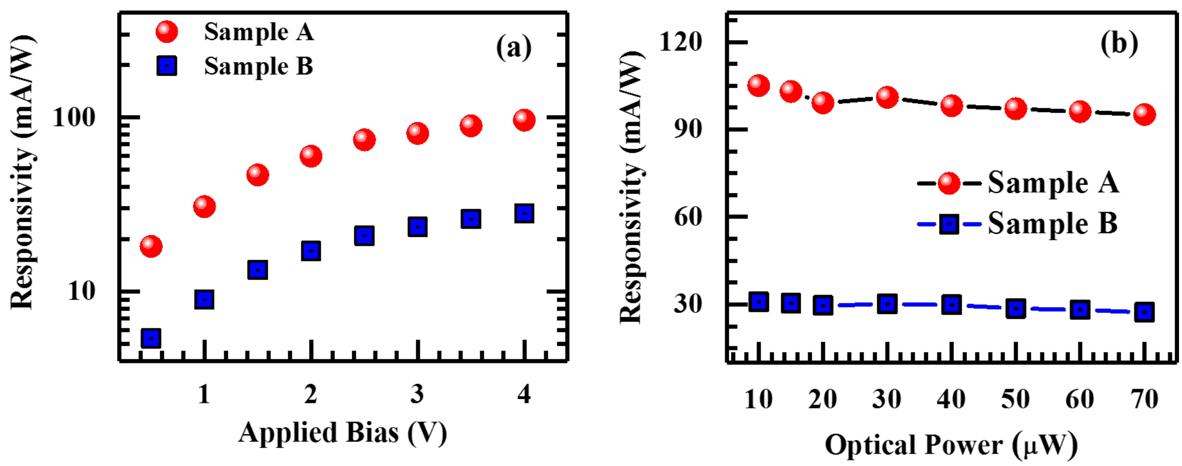

Figure 4.5 Responsivity of GaN MSM PDs as a function of (a) applied bias at 50μW, and (b) optical power at 4 V for sample A and B.

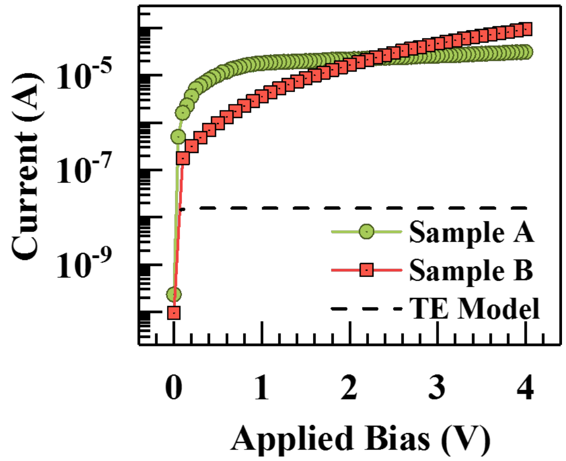

Figure 4.6 Room temperature I-V characteristics of the two GaN samples. Theoretical curve based on the TE model is also shown for comparison purpose.

As can be seen from figure 4.6, it is indeed true in case the applied bias is kept below 2 V where dark current of sample A is higher than that of sample B. However, the situation is just opposite if the applied bias is kept above 2 V. It is surprising to note that the dark current of PDs made out of sample A, which possesses relatively high dislocation density, is lower than that of sample B under high bias condition. Moreover, slope of the two curves is also seen to be very different. Further, it is sample B which shows a much larger difference from the theoretically estimated curve based on TE transport model [9] compared to sample A. It is noticed that the leakage current shows a much stronger dependence on applied bias in sample B. As already discussed in the previous chapter, it is well known that the threading dislocations and point defects provide an alternate path for charge conduction, which often lead to a considerably large leakage current in case of III-nitrides [90, 116, 127].Thus, the TFE process mediated by carrier tunnelling can be considered as a probable mechanism which can explain the I–V characteristics shown in figure 4.6. The reverse bias current under this model as proposed by Padovani and Stratton [54] can be expressed as:

$$I_{TFE} = I_{TFE,S}\, exp\left(-\frac{qV_R}{\zeta}\right) \tag{4.4}$$

where $I_{TFE,S}$ is the saturation current, V_R is the applied bias, and parameter ζ is expressed as

$\zeta = E_{00}\left[\left(\frac{E_{00}}{kT}\right) - tanh\left(\frac{E_{00}}{kT}\right)\right]^{-1}$ where k is the Boltzmann constant, T is the temperature in Kelvin and E_{00} is the characteristic tunnelling energy which is proportional to $\sqrt{N_D}$ as already shown in equation 3.8. As already discussed, a large value of E_{00} indicates about the dominance of TFE mechanism in charge transport [90]. It is observed that I–V characteristics of both the samples can be reasonably fitted by equation 4.4 over a wide temperature range, as shown in figure 4.7. This presents a direct evidence of the dominance of TFE mechanism in these samples. The values of E_{00} obtained from the fitting procedure are plotted in figure 4.8 for both the samples. A considerably high value of E_{00} in both the samples at low temperature indicates that TFE is the dominant current transport mechanism in this temperature regime. Such an observation is usual in HVPE grown GaN samples as already discussed where the presence of a large density of dislocations at the GaN/sapphire interface is found to be responsible for this behaviour [19, 90].

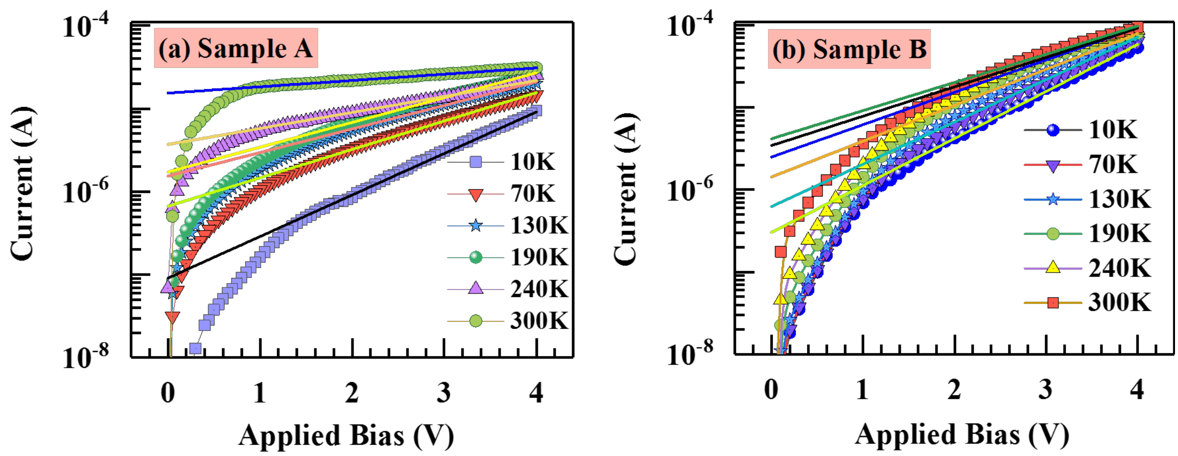

Figure 4.7 Temperature dependent I-V characteristics of (a) sample A, and (b) sample B where the respective solid lines show the corresponding theoretical curves based on the TFE model.

Further, a downward trend in the values of E_{00} can be observed with increasing temperature in both the samples. Note that E_{00} reduces from 7.6 (8.2) to 2.9 (6.0) meV with rise of temperature from 10 to 300 K for sample A (B) respectively. Moreover, an abrupt change is observed in sample A at ~200 K. On the other hand, slope of the curve is not that steep in sample B. These observations indicate that the carrier transport mechanism changes in sample A at ~200 K.

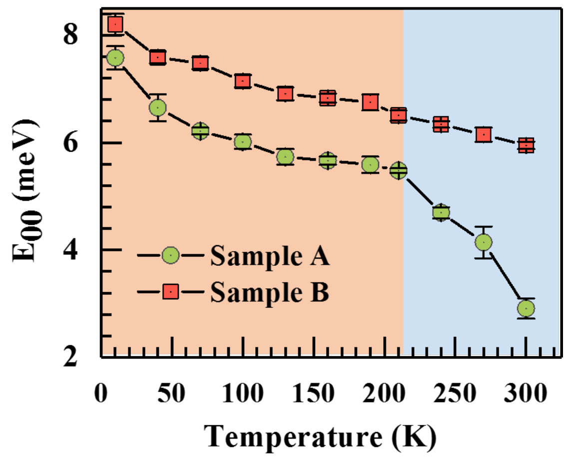

Figure 4.8 Temperature dependence of characteristic tunnelling energy (E_{00}) shown for the two GaN samples, error bars includes both the statistical and fitting errors. Regions showing a steep change in E_{00} values for sample A are highlighted by shading with different colours.

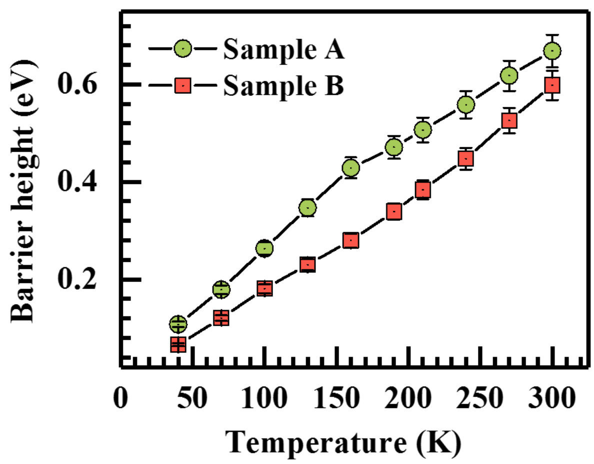

Figure 4.9 Schottky barrier height versus temperature for the two GaN samples. The data points are shown with error bars that includes both the statistical and instrumental errors.

In order to gain further understanding of the impact of carrier tunnelling on the dark current, Schottky barrier height of the two samples are plotted as a function of temperature in figure 4.9. For this purpose, Ni/Au Schottky contacts are fabricated on one side of the sample while Indium is used to make Ohmic contact on the other side. The values of Schottky barrier height shown in figure 4.9 are determined from the forward bias I-V curve considering TE model [90]. It is found that the barrier height monotonically increases with temperature for both the samples. Such a trend is very common in GaN samples as reported already in the previous chapter where interfacial defects and dislocation-related current paths are reported to be responsible for such non-ideal behaviour of Schottky contact [90, 91].

This observation can very well be explained by considering the tunnelling of carrier across the regions surrounding the core of dislocations [90]. An interesting observation can be made from figure 4.9 where the barrier height for sample A is seen to be larger than that of sample B at all temperatures. It is really surprising since the screw component of threading dislocations, which is responsible for lowering the barrier height in GaN [90, 118], is measured to be rather high in sample A as shown in Table 4.1. It therefore indicates that factors other than the dislocations seems to play a more decisive role in lowering (raising) the barrier height (leakage current) in sample B respectively and the same argument can also be applied to understand the contrast observed in the responsivity and transient response of the two samples. It is well known that many kinds of point defects are present in GaN [114] and it is highly possible that those might be responsible for the fall (rise) of barrier height (leakage current) in sample B irrespective of its low dislocation density. In order to investigate this point further, SIMS measurements are performed on the two samples for the identification of possible donor impurities in the two samples. Since Si and O are known to be primary donors in GaN, SIMS depth profiles corresponding to the two impurities are shown in figure 4.10. It can be seen from figure 4.10 (a) that the density of Si impurities is considerably higher in sample B whereas it is below detection limit in sample A. This gives a clear indication that sample B is heavily doped with Si leading to a carrier concentration of the order of 10^{18} cm^{-3}. Such a high intentional doping leads to an increase in the leakage current in this sample. From positron annihilation measurements, Zhao *et al.* [116] reported that even light doping with Si can increase the concentration of Ga vacancies in n-type GaN in comparison to undoped samples. Such Ga vacancies act as deep level defects leading to further rise of leakage current in sample B. On the other hand, the density of oxygen impurities is higher in sample A as shown in figure 4.10 (b). Clustering of oxygen impurities around the dislocation sites leads to the formation of a highly doped impurity channel in sample A which is the primary source of unintentional doping in HVPE GaN epilayer as already discussed [19, 90]. However, the carrier concentration at the edge of the depletion width of Schottky junction obtained from the C-V analysis is found to be two order less in sample A as discussed in the previous chapter [19]. Further, the values of carrier concentration estimated from C-V measurements are more relevant in case of MSM PDs due to the formation of Schottky junction. Hence, it can be concluded that the PDs fabricated on sample A with undoped GaN provide a much lower leakage current, even though those are having a higher dislocation density.

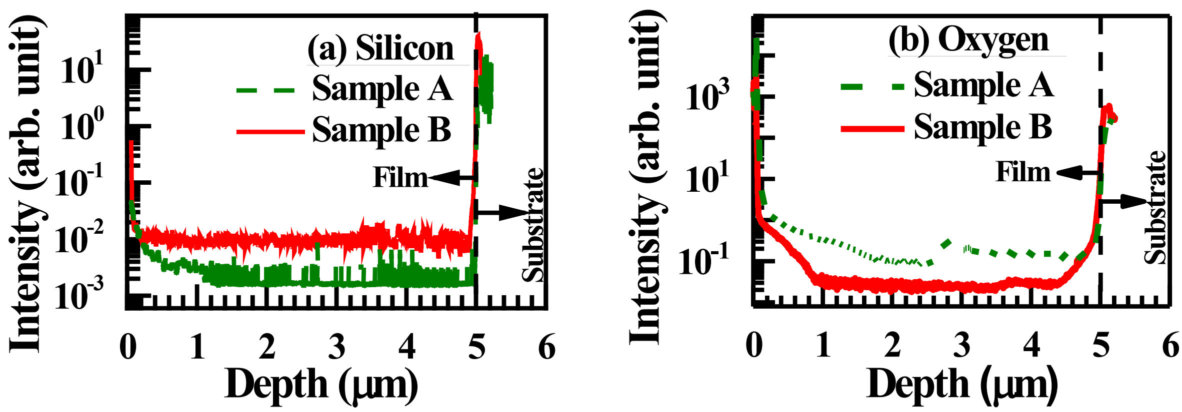

Figure. 4.10. SIMS depth profile for (a) Si, and (b) O impurities of the two GaN samples. For comparison purpose the measured data is normalised by the intensity of Ga secondary ion signal which also helps in minimizing the instrumental errors.

With this model, the observed temperature dependence of E_{00} and barrier height of the two samples can now be explained very well. It is already reported that the areal contribution of highly n-type regions surrounding dislocation cores is only 2-3% of entire Schottky area [95]. Therefore, their contribution is limited at high temperatures where TE mechanism associated with the large junction area plays a major role in the carrier transport. This mechanism leads to a dramatic reduction in the value of E_{00} in sample A in the high temperature range i.e. above ~200 K. Moreover, the dominant transport mechanism switches from TE to TFE during the cooling down process at ~200 K. On the other hand, TFE is the primary transport mechanism in the intentionally doped sample B at all temperatures leading to a comparatively weak temperature dependence of E_{00}. Temperature dependence of barrier height can also be explained on similar lines where sample A always maintains a high barrier since the screw dislocations responsible for the TFE transport are activated within a very small region of the total area. On the other hand in sample B, entire junction area takes part in the carrier transport.

Next, the same argument can also be used to explain the contrast observed in the performance of two sets of devices shown in figure 4.2 and 4.3. Since the drift component dominates the photocurrent in our devices, the magnitude of photo-response will be significantly influenced by the density of photo generated carriers that are available in the depletion region. The zero bias depletion width estimated from C-V measurements for sample A and B are 425 and 30 nm respectively [19]. It is numerically calculated that the photo response will be enhanced by a factor of ~ 4 in sample A due to the enlarged depletion width. It can partially explain the observed difference in the responsivity of two samples plotted in figure 4.2. Note that the density of screw and edge dislocations is few times higher for sample A which reduces the contrast in the responsivity of two samples. Had it not been the case then the measured difference between the photoresponse of two devices would have been larger.

Another point which needs to be explained is the faster response of devices as shown in figure 4.3. It can be understood by considering the role of point defects in sample B as mentioned earlier. It is already known that Si doping increases the concentration of Ga vacancies which reduces the minority carrier diffusion length due to the presence of deep level defects [116]. Ga vacancies trap the photo generated carriers in depletion region leading to the observed reduction in the speed of PDs fabricated on sample B [30, 128]. Further, absorption of excitation beam beyond the depletion width in sample B brings the diffusion component into play, which provides another reason for a slow response of the devices. It is also noticed that the exciton feature is clearly visible in terms of a sharp peak at 361 nm in the spectral response of sample A shown in figure 4.2, which is considerably supressed in sample B. Absence of excitonic feature can be explained by considering a high density of free carriers in sample B which screens the Coulomb interaction and reduces the exciton binding energy [129]. It also explains why a flat spectral response is observed in the above band gap region of sample B whereas a rise in the responsivity is seen with wavelength for sample A in figure 4.2. At shorter wavelength, an enhanced absorption of incident photons near the surface causes a fall in the responsivity due to the capture of photo excited carriers by the surface states. By proper surface passivation with thin oxide layer, a flat spectral response of PDs made on HVPE GaN layers can be achieved as already demonstrated by us [130]. A high density of ionized donors near the sample surface leads to a narrow depletion width in sample B and also minimizes the impact of surface states on the spectral response at shorter wavelength as shown in figure 4.2. Hence, it can be concluded that controlling the density of threading dislocations is not the sole criteria for improving the performance of GaN Schottky PDs, rather one also need to be careful about the density of point defects which can also limits the device performance considerably.

4.4 Origin of persistent photoconductivity in GaN photodetectors

Persistent photoconductivity (PPC) is an inherent problem in GaN UV detectors irrespective of the growth techniques such as MBE [131], MOVPE [132], or HVPE [133]. It has a detrimental effect on the performance of the devices [134]. Researchers found that the PPC effect does exist in GaN epilayers having substantial yellow emission (YL) [135, 136]. Since the YL band is centred at around 580 nm which is far from the band-edge (BE) related emission, it is identified as a defect related feature involving carrier recombination between shallow donor and deep acceptor. Since PPC is also observed in GaN under sub-band gap illumination with photon energy of 2.1 eV, this coincides with the peak of the broad YL band. Hence, it is argued that the defect level responsible for YL band is also involved in PPC effect in GaN. To investigate this further, PPC and PL measurements are performed on sample A and B at room temperature as shown in figure 4.11. As can be seen from the figure, the MOVPE grown sample B which shows large YL intensity also exhibits considerably higher PPC effect with device response time in seconds. On the other hand, the HVPE grown sample A is having much less YL intensity along with considerably faster response i.e. lowering in PPC effect.

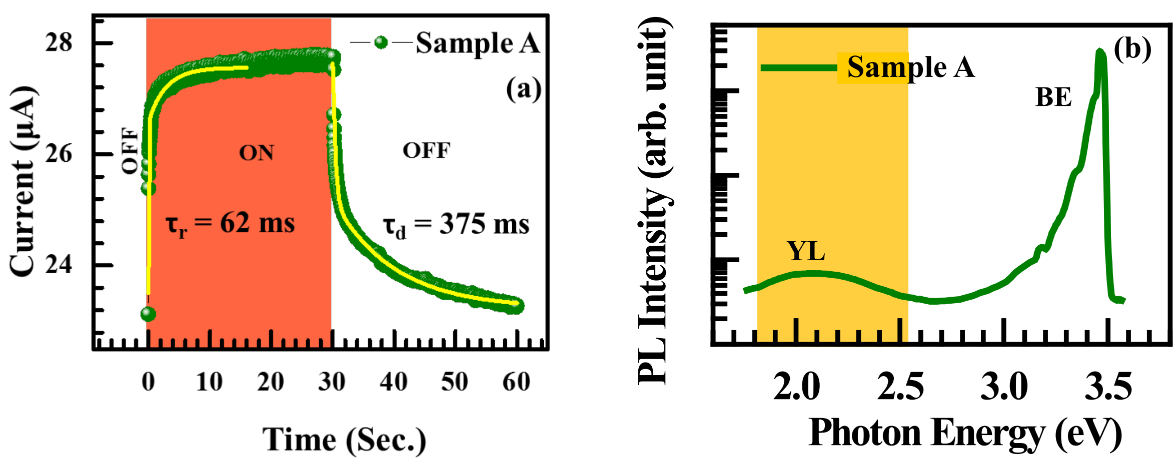

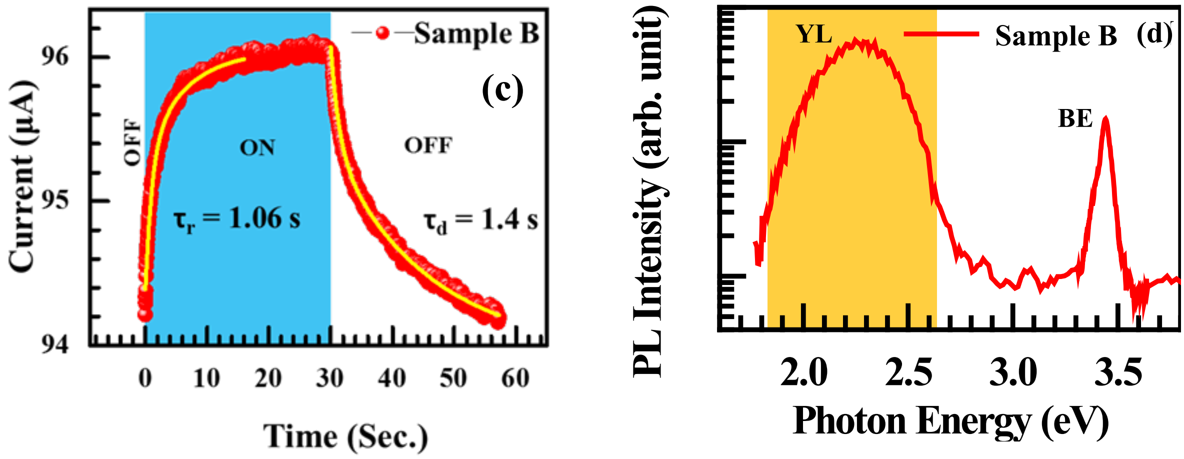

Figure. 4.11. Comparison of transient response and YL band PL data in (a-b) sample A and (c-d) sample B respectively.

To further strengthen the above understanding, spectral dependent PPC measurements are carried out for establishing the relationship between PPC and YL. Interestingly, photo response is observed at 1.93 eV (640 nm) i.e. sub band gap illumination for sample B as shown in figure 4.12. As the photon energy is further increased to 2.33 eV (532 nm), an increase in photo response is observed. Further, a steady increase in the photocurrent is noted as the photon energy is increased from 2.33 eV (532 nm) to 2.8 eV (442 nm). No such observation has been made on sample A with identical sub-band gap illumination.

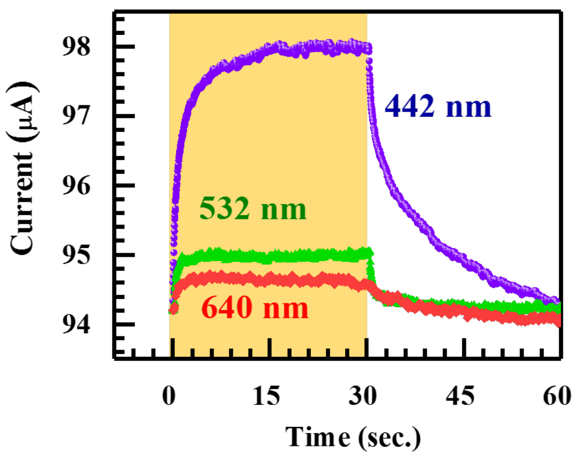

Figure. 4.12. PPC measurements under different sub-band gap illumination in sample B.

Note that the threshold energy of about 1.9 eV for observing PPC in sample B is roughly in good agreement with the energy at which the YL band starts appearing in figure 4.12. Hence, a steady upsurge of the photocurrent over a wide range of photon energy indicates that PPC is originating from a defect level which is spectrally broad in nature. A similar threshold energy for the photoionization of a deep-level defect has been reported in silicon doped GaN samples which is assigned to the YL band [137]. Thus, the present analysis strengthen the argument that PPC and YL in GaN are emerging from the same kind of defect.

4.5 Conclusion

In conclusion, GaN MSM UV PDs are fabricated on n-GaN epitaxial layers grown by HVPE and MOVPE techniques. Contrary to the general understanding, the photo response of HVPE based PDs is found to be ~ 3 times larger than that of the MOVPE based devices. Further, the overall performance of HVPE based PDs turns out to be better than those fabricated on MOVPE GaN, in spite of the variations in device geometry or the operating conditions. It is explained by considering the difference in the depletion width which is primarily governed by the different procedures adopted for the doping of GaN templates. A large carrier concentration at the edge of depletion width in MOVPE grown GaN epilayer leads to higher (lower) leakage current (barrier height) despite a low dislocation density. In temperature dependent I-V measurements, a sharp change in the value of characteristics tunnelling energy is seen at ~ 200 K for HVPE based devices whereas no such behaviour is seen for PDs fabricated on MOVPE grown epilayers. This is explained by considering the switching of electronic transport mechanism from TE to TFE during the cooling down. On the other hand, TFE is found to be the dominant transport mechanism in devices fabricated on MOVPE grown epilayers. It is hereby concluded that controlling the density of threading dislocations is not the sole criteria for improving the performance of GaN Schottky PDs, rather one also need to be careful about the density of point defects which can also marginalize the key figure-of-merits. It is also found that the MOVPE grown sample with larger YL intensity shows greater PPC effect which strengthen the argument that the two emerge from the same kind of defect. The understanding developed here is expected to be helpful in making a judicious choice of GaN templates for the development of specific devices based on them.

Chapter 5

Fabrication of Metal-Oxide-Semiconductor GaN Photodetectors

5.1 Introduction

In spite of a substantial improvement in the performance of nitride-based optoelectronic devices, GaN UV detectors still suffers from several limitations. For example, GaN-PDs often suffer from high leakage current, low photo-to-dark current ratio, and substantial persistent photoconductivity due to large density of threading dislocations and high background carrier concentration [90, 138]. A sluggish response of the device is often reported by researchers [139]. Note that a large barrier height at the metal/semiconductor (MS) interface is essential for the realization of high performance GaN MSM PDs. It offers low leakage current and high breakdown voltage leading to enhanced responsivity and high photo-to-dark current ratio. Selection of metal with larger work function is not the only qualifying criteria for reducing leakage current in GaN since a considerable amount of carriers prefer to tunnel the barrier in presence of large density of threading dislocations rather than crossing the barrier. Insertion of an insulating layer between metal and semiconductor is an effective technique for suppressing the leakage current and also for improving an overall performance of PDs. A significant reduction in the leakage current is already reported by several researchers by incorporating various insulating layers such as SiO_2, ZrO_2, GaO_x and Al_2O_3 [140-142]. Although a considerable amount of work is already carried out on GaN based MOS PDs, but a consensus among researchers is yet to arrive on the choice of material and thickness of insulating layer. For example, Lee *et al*. used 130 nm thick GaO_x interlayer for achieving photo-to-dark current ratio of ~10^6 [141] where a peak responsivity of 9 A/W was demonstrated. On the other hand, Chen *et al*. [142] reported a photo-to-dark current ratio of ~10^3 by using only 30 nm thick insulating layer of ZrO_2 where a peak responsivity of only 0.02A/W was reported. In yet another report, a photo-to-dark current ratio of ~10^4 and peak responsivity of 1.42 A/W was demonstrated by inserting a very thin (only 1.5nm) layer of HfO_2 [143]. Hence, selection of oxide material and layer thickness are not trivial issues since improvement of one detector characteristic may lead to the degradation of another. Moreover, thickness of oxide layer might become the limiting factor in governing the performance of device in many cases, however, this issue is not yet discussed for GaN MOS PDs.

In this chapter, a detail analysis on the reduction of leakage current and improvement in spectral response of GaN UV PDs by insertion of an oxide inter layer is presented. Detectors with different oxide interlayers like SiO_2 and ZrO_2 are fabricated and their performance is compared. The role of oxide layer thickness on the performance of GaN MSM PDs is investigated by performing a comprehensive characterization of Au/Ni/ZrO_2/GaN MSM PDs. The values of dark current in MSM UV detectors without and with oxide layer of varying thickness are compared, and key operating characteristics of PDs are optimized.

5.2 Device fabrication details

GaN MOS detectors in ring contact geometry are fabricated on sample C. After proper organic cleaning, Ti (15 nm)/ Al (80 nm)/ Ni (40 nm)/ Au (100 nm) multi-layer Ohmic contact are deposited using thermal evaporation technique under a base pressure of 5×10^{-6} Torr in a ring geometry with external dia. of 1.2 mm. After that, the contact is annealed at 900^{o}C for 45 s to achieve proper Ohmic contact. SiO_2 and ZrO_2 thin insulating layers of 15 nm thickness are then deposited by electron-beam evaporation under a base pressure of 7×10^{-6} Torr. Further, Ni (15 nm)/ Au (100 nm) Schottky contact dot of 0.8 mm dia. is deposited as shown in figure 5.1. For studying role of oxide thickness on detector performance, four samples are prepared with different ZrO_2 thickness. Sample C is the HVPE grown epilayer without any oxide layer as already discussed in chapter 2, table 2.3. The other three samples D, E and F are having 3, 6 and 9 nm thick ZrO_2 layer deposited on GaN respectively [130]. Thickness of ZrO_2 layer is measured in-situ by quartz crystal and also confirmed by performing x-ray reflectivity (XRR) measurements on a calibration sample (not shown here). ZrO_2 layers are found to be of polycrystalline nature with dominant tetragonal phase. Further details on the structural and morphological properties of ZrO_2 layers are given elsewhere [144]. In a previous study, it was found that the surface region of ZrO_2 shows a gradual change in the electron density with depth due to the presence of surface states and contamination issues [144]. Since the thickness of surface layer was found to be about 3 nm from XRR measurements, thickness of ZrO_2 passivation layer is restricted to 3 nm in this work. Afterwards, Schottky diodes are fabricated on these samples by depositing Ni (15nm)/Au (100nm) contacts by shadow metal mask. Width of the contacts is kept 500 μm, while separation between the contact pads is restricted to 200 μm. A schematic diagram of device geometry is shown in the inset of figure 5.1 (d).

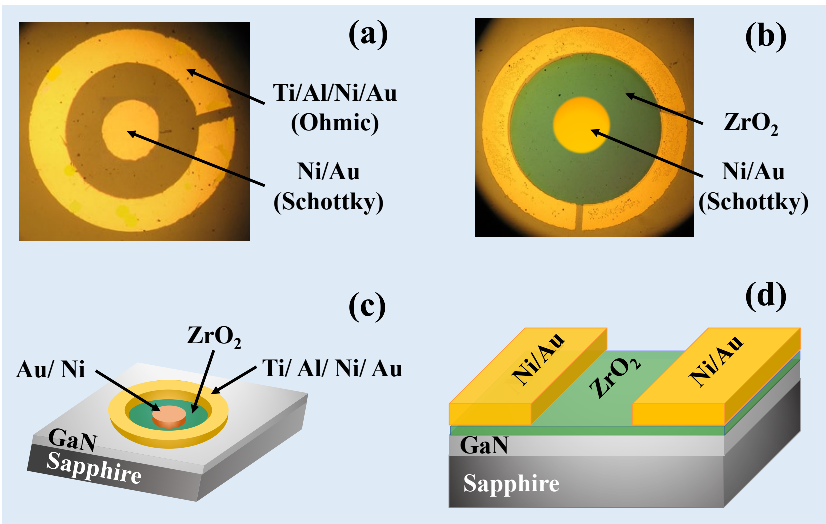

Figure 5.1 Optical microscopic image of the device (a) without and (b) with oxide inter layer, (c-d) Schematic diagram showing the device structure.

5.3 Selection of oxide for the fabrication of GaN MOS detector

In order to investigate the role of oxide interlayer, the reverse bias leakage currents of Au/SiO_2/GaN and Au/ZrO_2/GaN are compared in figure 5.2. As can be seen from the figure, the leakage current is 8 times lower in SiO_2/GaN sample and 28 times smaller in ZrO_2/GaN sample when compared with Au/GaN Schottky junction devices. However, the oxide/GaN MOS system possess a considerably large density of interface states and fixed oxide charges, which can substantially affect the performance of the device. Slower states known as border traps located within the interfacial region of oxide and semiconductor are also detrimental for the device and considered to be the primary challenge for the development of GaN MOS detectors. Charge trapping in these sites is the possible reason behind a high value of leakage current in SiO_2 based device compared to ZrO_2 based one. This can be verified further by C-V hysteresis measurements. The capacitance responses are measured by sweeping applied bias from inversion to accumulation, and subsequently sweeping back toward inversion. The measurement is performed at room temperature and at a high frequency of 1 MHz.

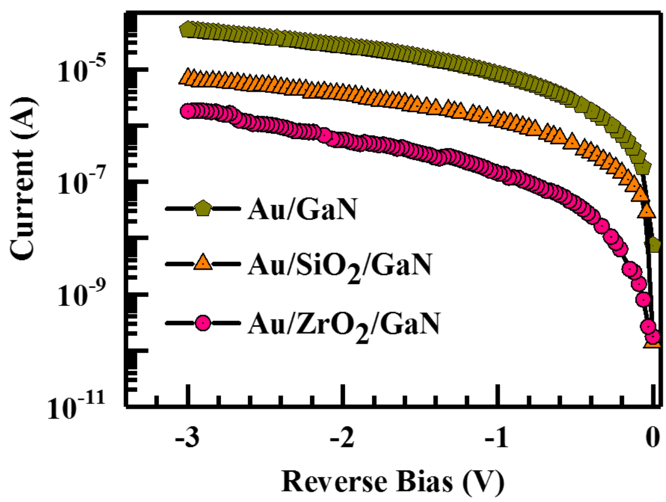

Figure 5.2 Reverse bias leakage current of Au/GaN, Au/SiO_2/GaN and Au/ZrO_2/GaN devices.

The density of trapped charges in units of cm^{-2} is quantified as [145]:

$$Q_{trap} = (C_{ox} \times \Delta V)/q \tag{5.1}$$

where ΔV is the C-V hysteresis in Volts and C_{ox} is the oxide capacitance in F cm^{-2}.

C-V measurement results are represented in figure 5.3, clearly showing that considerably lower C-V hysteresis gap is observed in Au/ZrO_2/GaN sample that leads to one order lower trapped charge density when compared with Au/SiO_2/GaN device.

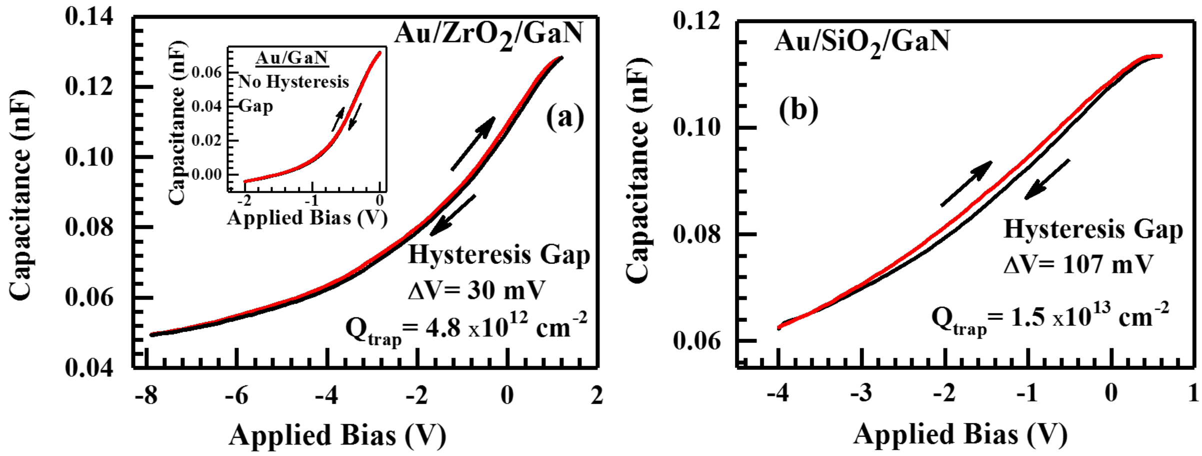

Figure 5.3 Hysteresis in C-V measured at 1 MHz for (a) Au/ZrO_2/GaN and (b) Au/SiO_2/GaN devices. Inset of figure 5.3 (a) shows absence of C-V hysteresis in Au/GaN sample.

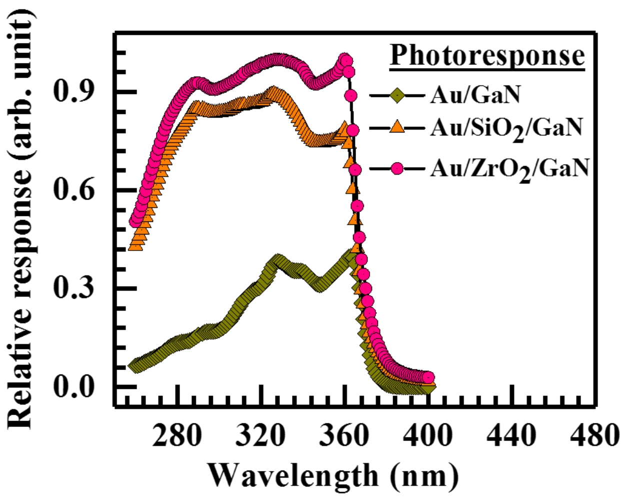

Figure 5.4 Relative spectral response of Au/GaN, Au/SiO_2/GaN and Au/ZrO_2/GaN devices.

The higher charge density in SiO_2 based sample may be due to several reasons including higher source impurity, crystalline defects and off-stoichiometry effect in the deposited oxide layer by e-beam deposition technique. Moreover, the presence of low density of trapped charges causes small leakage current in Au/ZrO_2/GaN device. Photo response curves of three devices are compared in figure 5.4. All the devices clearly exhibit considerable photo response at shorter wavelength side and sharp intrinsic transition above the band edge of GaN occurred at 360 nm. Also, the oxide passivated samples show a relatively flat response in shorter wavelength side in comparison to un-passivated sample. This is because surface passivation reduces surface recombination of photo generated carriers resulting in a flat response in low wavelength range. Hence, considerable improvement in device response is achieved in both the MOS devices with ZrO_2 based device showing superior performance among all detectors.

5.4 Role of ZrO_2 passivation layer thickness on device response

In order to investigate the importance of ZrO_2 passivation layer thickness in the performance of high responsivity GaN UV PDs, room temperature I-V characteristic of the devices fabricated on sample C, D, E and F are compared in figure 5.5. It is seen that the variation of dark current in case of sample C is significantly different when compared with the theoretically predicted curve based on the TE transport model [90]. It is well known that, threading dislocations act as an alternate conduction path in III-nitrides, which often lead to high leakage current in Schottky diodes [90, 127, 146]. Presence of a large density of dislocations at GaN/sapphire interface in similar HVPE grown 5 μm thick GaN samples including their adverse effect on the optoelectronic properties of devices made out of them is already discussed in the previous chapters [19, 90]. By performing temperature dependent I-V measurements, it is concluded that the dislocation assisted tunnelling of carriers across Schottky junction is the dominant transport mechanism in these devices.

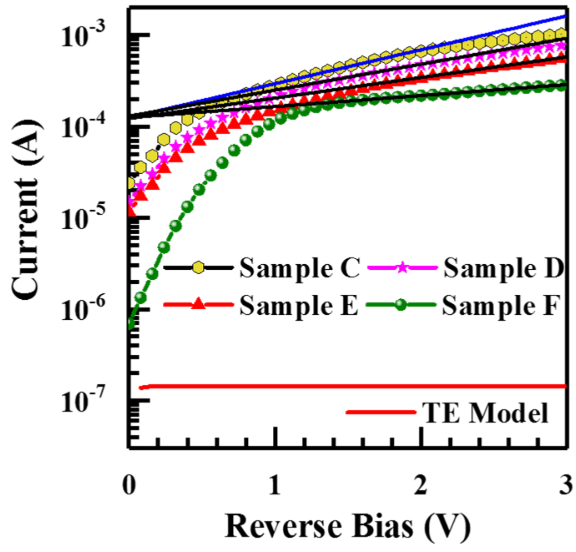

Figure 5.5 Room temperature I-V characteristics of Au/Ni/GaN Schottky diodes without and with ZrO_2 passivation layer where respective solid lines show the corresponding theoretical curves based on TFE model. Theoretical curve based on TE model (red solid line) is also shown for comparison purpose.

Thus, TFE process mediated by dislocation assisted tunnelling becomes an obvious alternative choice for explaining the observed I-V curve for sample C. A detailed analysis by Padovani and Stratton [54] based on the Taylor expansion of tunnelling probability under WKB approximation lead to the following expressions of tunnelling current under TFE;

$$I_{TFE} = I_{TFE,S} \exp\left(-\frac{qV_R}{\xi}\right) \tag{5.2}$$

where $I_{TFE,S}$ is the saturation current, V_R is the applied reverse-bias, and parameter ξ is expressed as $\xi = E_{00}\left[\left(\frac{E_{00}}{kT}\right) - \tanh\left(\frac{E_{00}}{kT}\right)\right]^{-1}$.

I-V curve of sample C is nicely fitted with equation 5.2 as shown in figure 5.5. It provides a direct evidence of the dominance of TFE mechanism. Next, I-V characteristics for the remaining samples with ZrO_2 inter-layer of varying thickness are also shown in figure 5.5. It is seen that the leakage current considerably reduces at large thickness of oxide layer. Once again the I-V curves can be fitted with equation 5.2 where the measured values of E_{00} are summarized in table 5.1. A downward trend in E_{00} with increasing ZrO_2 thickness suggests about the suppression of carrier tunnelling across Schottky junction which in turn reduces the leakage current. In order to understand the role of oxide layer thickness on device characteristics, spectral response of all the four PDs is plotted in figure 5.6. All the devices exhibit good photoresponse in the UV range along with a sharp cut-off near GaN band edge showing a UV-to-visible rejection ratio of ~10^3 which confirms their visible-blind nature. Further, the oxide passivated samples show a relatively flat response in shorter wavelength side with more than 1.6 times higher UV-to-visible rejection ratio in comparison to un-passivated sample.

Table 5.1 A summary of Schottky junction parameters estimated by using TFE model.

Sample No.	**C**	**D**	**E**	**F**
ZrO_2 thickness (nm)	0	3	6	9
***E_{00}* (meV)**	8 ± 0.5	6 ± 0.5	4.6 ± 0.3	3.3 ± 0.4

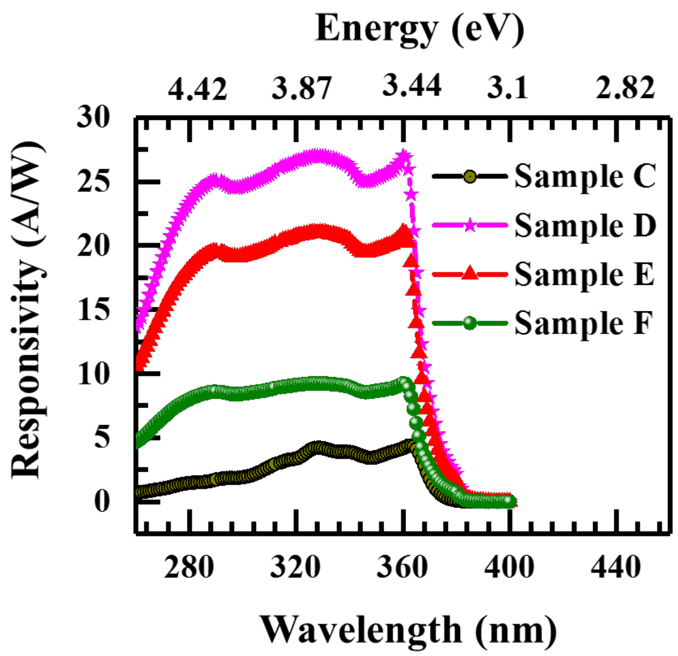

Figure 5.6 Spectral response of GaN PDs without and with different thickness of ZrO_2 layer.

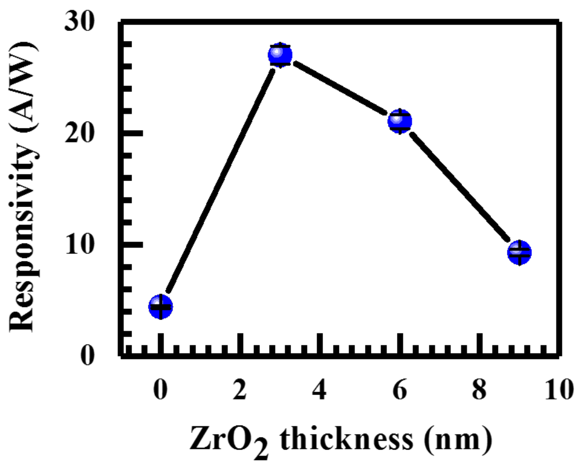

Figure 5.7 Spectral response of GaN PDs without and with different thickness of ZrO_2 layer.

This is because surface passivation reduces surface recombination of photo generated carriers resulting in a flat response in low wavelength range. The peak responsivity is plotted in figure 5.7 which shows a 7 times enhancement after passivation by 3 nm thick ZrO_2 layer followed by a subsequent reduction with further increase of oxide layer thickness. Note that the theoretical limit on the responsivity of an ideal GaN MSM PD at 361 nm is 0.29 A/W, assuming a gain of 1 and an external quantum efficiency of 100%. Thus the responsivity of all the PDs in figure 5.7 is much larger than the theoretical limit, which confirms the existence of internal gain in these devices.

Presence of acceptor like negatively charged states originating from threading dislocations, dangling bonds, and native oxides etc. is reported to be responsible for such a large gain in these devices [147-149]. Note that the peak responsivity of 27 A/W is maximum in sample D for ZrO_2 layer of 3 nm thickness which reduces with further increase of oxide layer thickness. This phenomenon can be explained by invoking the concept of quantum mechanical tunnelling of the photo-generated holes which is assisted by the traps at oxide-semiconductor interface as schematically shown in figure 5.8.

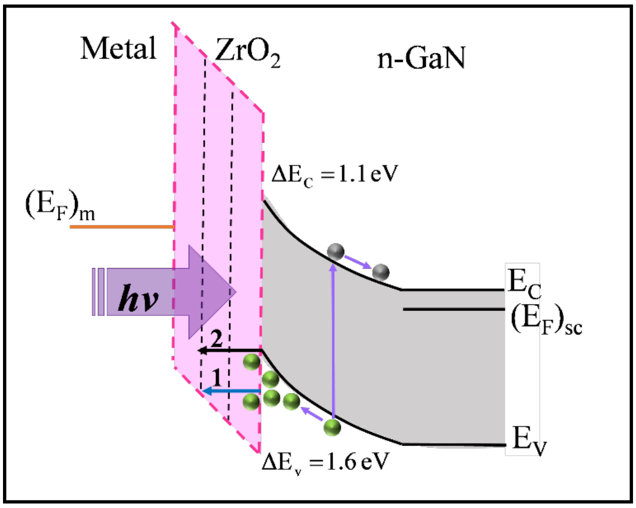

Figure 5.8 Energy band diagram for GaN PDs under reverse bias with varying ZrO_2 thickness (black dashed lines) where arrows 1 (2) represent tunnelling through high (low) energy hole traps respectively.

As shown in figure 5.8, when the thickness of oxide layer is low, holes with small energy can tunnel through the barrier. For a larger value of oxide layer thickness, the tunnelling probability reduces and holes with higher energy will only be able to tunnel through the barrier. Consequently, a low value of photoresponse is recorded for larger (> 3 nm) values of ZrO_2 layer thickness.

Further the response speed of PDs is also affected by the variation in the thickness of oxide layer. Measurement of transient response, which is one of the key figure of merit of any PD can provide more insight into the particular characteristic of the device. As can be seen from figure 5.9, sample D with 3 nm ZrO_2 passivation layer reveals relatively faster response despite of its higher gain. This may be caused by an effective passivation of deep trap states after the deposition of ZrO_2 layer. However, similar to the observations made for peak responsivity, the transient response of the PDs slows down at large thickness of ZrO_2 layer. One possible explanation of such an observation can be given in terms of a considerable enhancement of the number of charge trapping sites referred as slow states or border traps in oxide inter layer with increasing oxide thickness. Further, the stability of the device, with 3 nm ZrO_2 layer is verified by repeating the transient measurement for several ON/OFF cycles, where a representative plot for a few cycles is shown in figure 5.10. The device exhibits a sharp ON/OFF transition in photocurrent with good stability and reproducibility upon light pulse exposure at 4V applied bias.

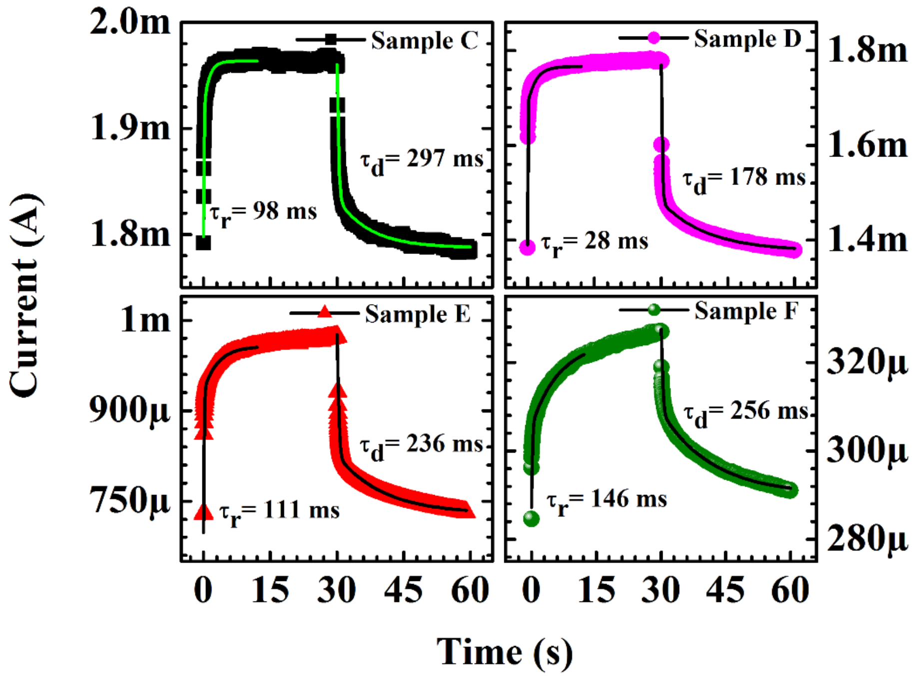

Figure 5.9 Transient photoresponse of four samples measured at 4V applied bias under UV illumination (325 nm) at an optical power density of 25 mW/cm^2.

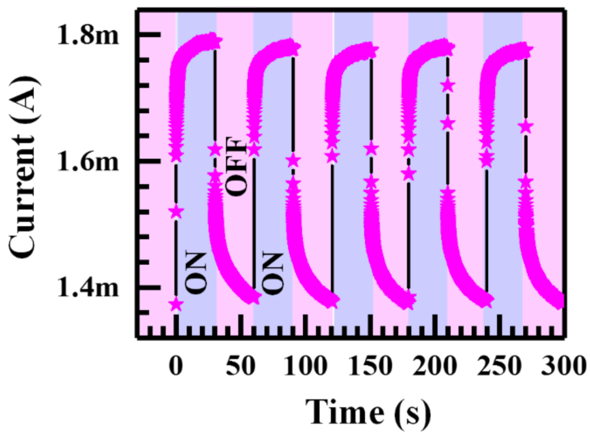

Figure 5.10 Optical switching performance of GaN UV detector with 3nm ZrO_2 inter layer under UV illumination (325 nm) at an optical power density of 25 mW/cm^2.

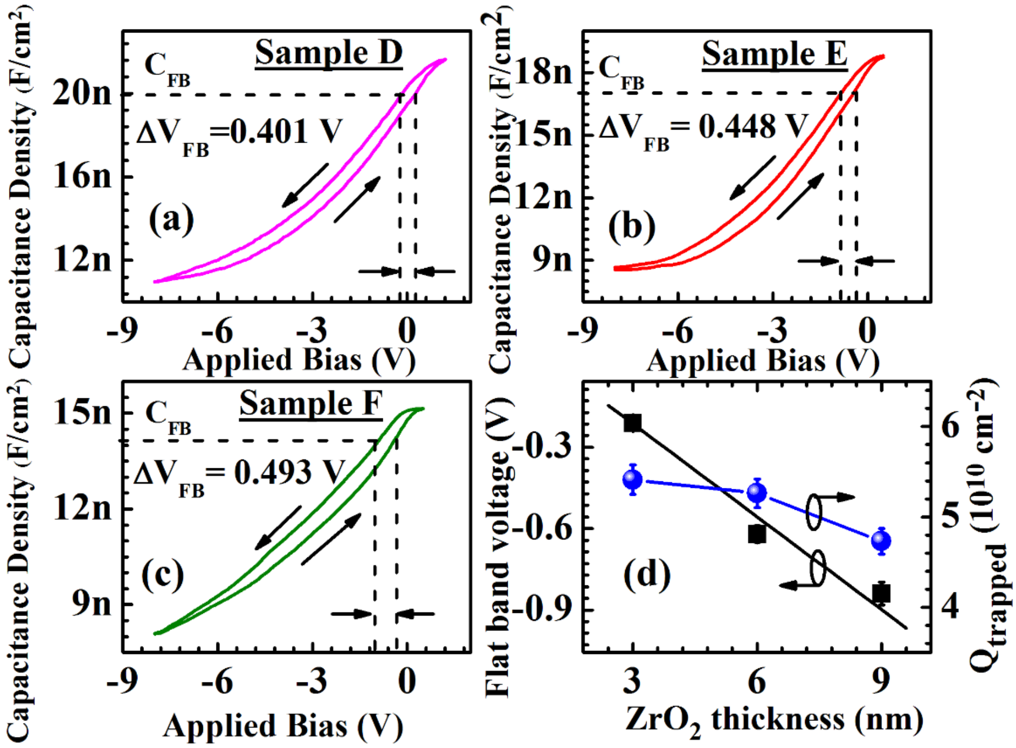

Figure 5.11 C-V hysteresis curves for (a) sample D, (b) sample E and (c) sample F measured at 1 MHz, (d) Flat band voltage (V_{FB}) and charge trapping density ($Q_{trapped}$) as a function of ZrO_2 layer thickness. The data points in figure 5.11 (d) are shown with 3% error bar that includes both the statistical and instrumental errors.

However, due to the presence of large threading dislocation density in GaN epilayers, it is not possible to reduce the dark current below a certain level.

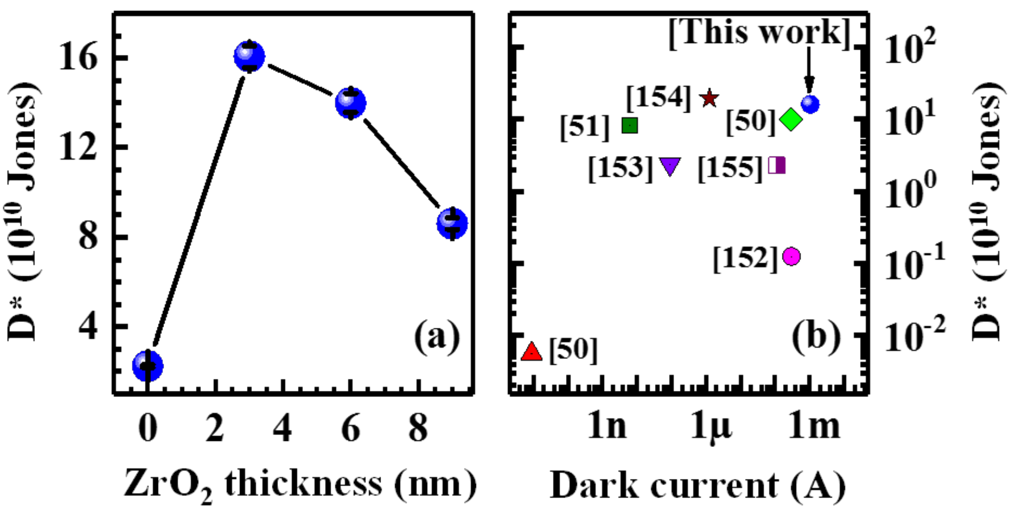

Figure 5.12 (a) Specific detectivity plotted as a function of ZrO_2 thickness and (b) State-of-the-art values of D* versus dark current for GaN UV detectors are plotted for comparison purpose.

The border trap density ($Q_{trapped}$) can be determined from the C-V hysteresis obtained from the separation of C–V curves measured in the forward (depletion to accumulation) and in the reverse (accumulation to depletion) bias sweep as already shown in figure 5.3. Room temperature C-V hysteresis measurements were performed on these samples where the results are shown in figure 5.11. These measurements were performed at a high frequency of 1 MHz to ensure that only depletion capacitance pursues the ac signal. C-V hysteresis is measured from the difference in voltage at the flat band capacitance (C_{FB}) indicated by the dotted lines in figure 5.11. The value of $Q_{trapped}$ extracted from ΔV_{FB} is found to be $5.1 \pm 0.4 \times 10^{10}$ cm^{-2} in all the samples. Note that V_{FB} exhibits a linear relationship with ZrO_2 layer thickness, which along with a constant value of $Q_{trapped}$ provides further evidence that the trapped charge is primarily localised as a line charge (in units of cm^{-2}) at or near the ZrO_2/GaN interface [145, 150]. The above results confirm that no new slow trap states are generated at large thickness of ZrO_2 layer. Hence, a slow transient response of PDs at large thickness of ZrO_2 layer is primarily governed by the low probability of hole tunnelling as evident from figure 5.5 and figure 5.8.

Another important figure-of-merit of PDs is the D* which corresponds to their ability to detect the weakest signal. Recently, a few methods have been proposed by researchers [50, 51, 152-155] for enhancing the value of D* which is actually estimated by following the procedure given in Ref. [156]. In order to compare the values of D* of the present study with the recently reported state-of-the-art values [50, 51, 152-155], the same procedure has been followed here and the estimated values of D* are plotted in figure 5.12. It is found that the value of D* for sample D is 1.6×10^{11} Jones which is about an order of magnitude higher than that of the sample C. Note that D* can be enhanced either by increasing the responsivity or by reducing the dark current.

Under such circumstances, a viable solution for enhancing D* can be obtained by maximizing the value of responsivity via a controlled passivation of surface states in GaN layer as shown in figure 5.12 (a). In figure 5.12 (b), recently reported values of D* for several state-of-the-art visible blind GaN UV PDs are plotted as a function of dark current [50, 51, 152-155] along with the data from the present analysis. Note that the value of D* measured for sample D is higher or comparable to the values reported in literature irrespective of its large dark current. Hence, a controlled surface passivation with appropriate thickness of oxide layer can play a decisive role in obtaining superior performance of UV PDs even in presence of a large density of dislocations. However, a word of caution related to the procedure for the estimation of D* is necessary as suggested by Li *et al.* [157]. Depending upon the dominance of a particular noise mechanism in PDs, the measured value of D* might change. Nevertheless, the trends presented here shall remain intact.

5.5 Conclusion

In conclusion, a considerable improvement in the performance of GaN UV detector has been demonstrated by the insertion of thin oxide layer. The device leakage current is found to be reduced by 8 (28) times in SiO_2 (ZrO_2)/GaN sample when compared with Au/GaN Schottky junction devices. The density of trapped charges is found to be one order less in ZrO_2 based device in comparison to SiO_2 based detector, while no appreciable trapped charges is observed in the device without oxide insulating layer. Further, considerable improvement in photo response is observed in both the MOS devices with ZrO_2 based device showing superior performance among the three PDs. Importance of ZrO_2 passivation layer thickness in the performance of high responsivity GaN UV PDs is investigated further. It is found that an optimum thickness of ZrO_2 layer exists which plays a critical role in controlling the photo and transient responses of the device. Beyond the optimal thickness, performance of PDs deteriorates which is limited by the restricted tunnelling of photo generated carriers across the oxide layer. At an optimum ZrO_2 thickness of 3 nm, a spectral responsivity of 27 A/W at 361 nm is achieved at 4V applied bias along with the fast response of device with rise (fall) time of 28 ms (178 ms) respectively. Such characteristics are found to be similar or better than the recently reported state-of-the-art values for visible blind PDs fabricated on GaN. The results presented here confirm that the surface passivation with an optimal thickness of oxide layer can be used to develop high responsivity GaN based UV PDs irrespective of having a large dark current which is often inevitable due to the presence of a large density of dislocations in GaN epitaxial layers grown on foreign substrates.

Chapter 6

Impact of Reactive Ion Etching on the Characteristic of GaN Photodetectors

6.1 Introduction

Fabrication of an optoelectronic device with smaller geometry requires precise pattern transfer which can be achieved by photolithography and selective chemical etching of the material. Also for fabricating light emitting diodes or PIN PDs based on GaN/sapphire, it is essential to etch part of the sample for the formation of the bottom contact with n-GaN layer in vertical geometry. However, as already discussed in chapter 2, there are no reliable wet etchants for III-nitrides due to their inertness towards harsh chemical environment [158]. Precise pattern transfer during the fabrication of optoelectronic devices therefore involves dry etching methods using high energy ions [159]. Several dry etching methods using a variety of plasma conditions have been employed during the last decade where Cl_2 based plasma is found to be very effective in etching nitride semiconductors [159-162]. It is also known that the etch rate is invariably restricted by the sputter removal of etch products [160] which in turn depend on the ion energy. For the ion energy being too low, many reactions do not occur, which results in a poor yield of etching process [163]. On the other hand, for too high ion energy, unwanted sputter etching may damage the substrate surface which can change the stoichiometry and chemical bond of the surface region up to a depth of several atomic layers [164]. Energetic ion bombardment can lead to the creation of lattice defects and dislocations, implantation of etch ions or formation of dangling bonds on the substrate surface [165]. It may also introduce deep levels and nonradiative recombination centres which reduce the optical quality of material [165]. Hence, the energetic ion bombardment-induced damage may deteriorate the electrical and optical properties of nitride materials and subsequently the performance of semiconductor devices made out of them [166, 167]. Since GaN is chemically more inert than GaAs, it is reasonable to use relatively high energy of ions for etching nitride semiconductors while keeping the crystal damage as minimum as possible. Therefore, optimization of dry etching process becomes a crucial step in bringing the performance of nitride based devices close to the theoretically predicted values. It is already reported that the plasma induced damage degrades the Schottky junction properties substantially while improves the Ohmic contact properties [168, 169]. It is explained on the basis of a preferential sputtering of nitrogen atoms leading to the creation of nitrogen vacancy (V_N) at the surface which acts as shallow donors [169-171]. Attempts have been made to recover the etch-induced surface damage by means of thermal annealing [166, 172], wet etching [173], surface passivation [174], surface treatment [175] and plasma treatment [176, 177] etc. However, most of these methods are unable to restore the electrical properties of near-surface region of plasma etched GaN completely [176, 178]. Out of all the recovery methods, post etch O_2 plasma treatment is relatively easy and is highly practical since O_2 plasma can be created in the same chamber by maintaining the inert atmosphere without exposing the sample to atmosphere. Although there exists a few reports on the improvement of optoelectronic properties of GaN after O_2 plasma treatment [179], a systematic study related to the response of GaN UV photo detector is missing. Note that the nature of defect levels contributing in PL of plasma etched GaN epi-layer and of those affecting the photo response of GaN photodetector is not necessarily the same. Therefore, an in-depth analysis of the plasma etch induced degradation of electronic and optical properties of GaN epitaxial layers and also the photoresponse of GaN Schottky photo detector is required.

In this chapter, effect of BCl_3 plasma etching induced damage on the surface morphology, electrical and optical properties of heavily doped n-type GaN samples is investigated. A qualitative analysis of defect associated surface tunnelling of carriers with increasing ion energy is carried out by considering TFE model. Extent of depth up to which GaN epi-layer is damaged by the plasma etching is also estimated. Recovery of the optoelectronic properties of GaN epi-layer under post etch O_2 plasma treatment is also systemically studied. Further, the effect of plasma etch induced damage on the performance of GaN based Schottky photodiodes is analysed and a marked recovery of photoresponse after treatment with O_2 plasma along with an improved deep UV response of the detector is demonstrated.

6.2 Device fabrication details

Reactive ion etching (RIE) is carried out in a conventional RIE chamber with parallel electrodes and a radio-frequency (RF) generator (13.56 MHz) at a chamber pressure of 28 mTorr under a BCl_3/N_2 (10 /10 sccm) plasma with RF power varying from 100-250W. The system details are discussed in chapter 2. The etching studies are performed on n-GaN epilayers grown by HVPE (sample A) technique. Proper organic cleaning of the samples is carried out as already mentioned in the section 2.7.1 of chapter 2. Prior to etching, the chamber is pumped down to a base pressure of about 5×10^{-6} Torr. The etch rate of BCl_3 plasma is determined by measuring the step height in dry etched GaN with the help of Dektak profilometer. A 250 nm thick SiO_2 mask deposited by e-beam evaporation technique is used on the samples for dry etching purpose. In order to recover the etch-induced damages, post etch O_2 plasma treatment is carried out in the same RIE chamber at an RF power of 300 W for 1 min with O_2 flow rate of 30 sccm. Plasma etched GaN epi-layers are then taken out of RIE chamber for metallization as shown schematically in figure 6.1(a).

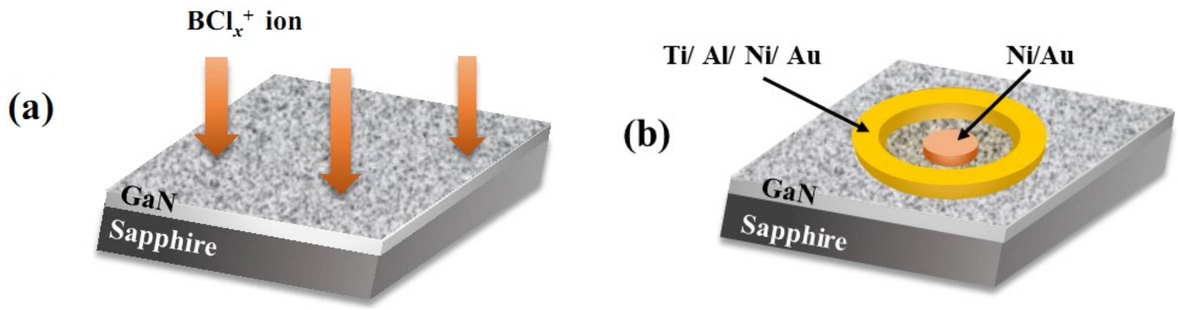

Figure 6.1 Schematic diagram of (a) reactive ion etched GaN epilayer, and (b) GaN UV photodetector made out of dry etched GaN epilayers.

Four samples are prepared for comparison purpose: sample A stands for as-grown GaN whose detail is already discussed in Table 2.3 of chapter 2, sample G for 150W and sample H for 250W RF plasma etched GaN and sample I for O_2 plasma treatment on post 250W RF plasma etched sample. In order to make low resistance Ohmic contacts, Indium (In) dots are placed on the samples which are subsequently annealed at 375°C for 30s under nitrogen ambient. For studying the effect of RIE induced damage on Schottky diode properties, Ni (100nm)/Au (250nm) Schottky contact pads are deposited on etched GaN epi-layer using thermal evaporation technique under a base pressure of 4×10^{-6} Torr through a circular metal mask with 0.8 mm dia. Photo-response of the device is measured in ring contact geometry where Ti (20nm)/ Al (60nm)/ Ni (20nm)/ Au (150nm) multi-layer Ohmic contacts are fabricated using shadow metal mask (ring type) with inner (outer) diameter of 3 (4) mm and are subsequently annealed at 850°C for 45s under nitrogen ambient. Afterwards, Ni (100nm)/ Au (250nm) Schottky contact pads are deposited in the centre of ring contact as shown in figure 6.1(b). As can be seen from figure 6.1(b), both the Ohmic and Schottky contacts are fabricated on the top of GaN epi-layer since Sapphire substrate is insulating.

6.3 Effect of RIE on the performance of GaN Schottky detectors

In order to investigate the impact of plasma etching, the surface morphology of etched GaN epilayers is examined by Scanning Electron Microscopy (SEM). Representative SEM images depicting the surface morphology of plasma etched GaN epilayers with increasing RF power are shown in figure 6.2. It is found that the etch rate increases from 12 nm/s at 100W RF power to 40 nm/s at 250W while maintaining the chamber pressure and BCl_3/N_2 flow rate constant. With increasing RF power, the induced dc bias corresponding to the energy of etchant ions increases [75]. This increases the bond breaking efficiency, which is the only rate-limiting step in etching of nitrides, thus resulting in high etch rate. But as expected, the SEM images show that the ion bombardment during dry etching roughens the surface in sample G and H which indicates that the other material properties may also be altered by the energetic impinging ions. Moreover, the etch residues disappeared from the surface up to a certain extent resulting smoother n-GaN surface after O_2 plasma treatment in sample I as observed in figure 6.2 (d).

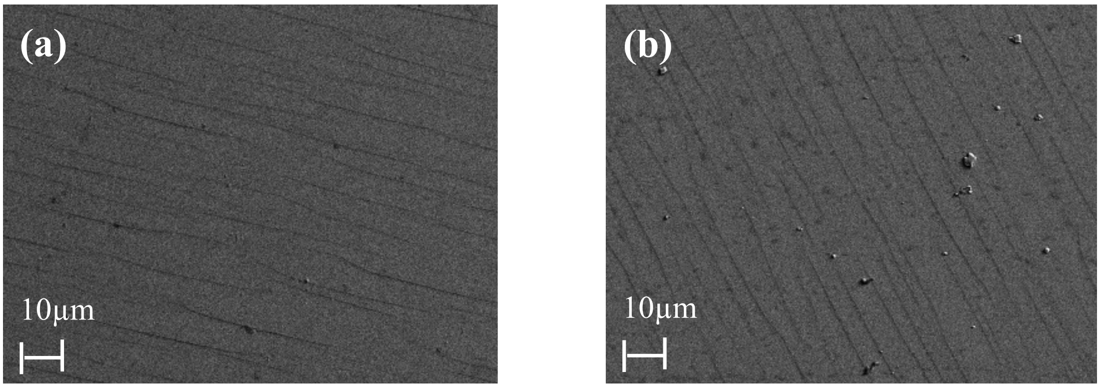

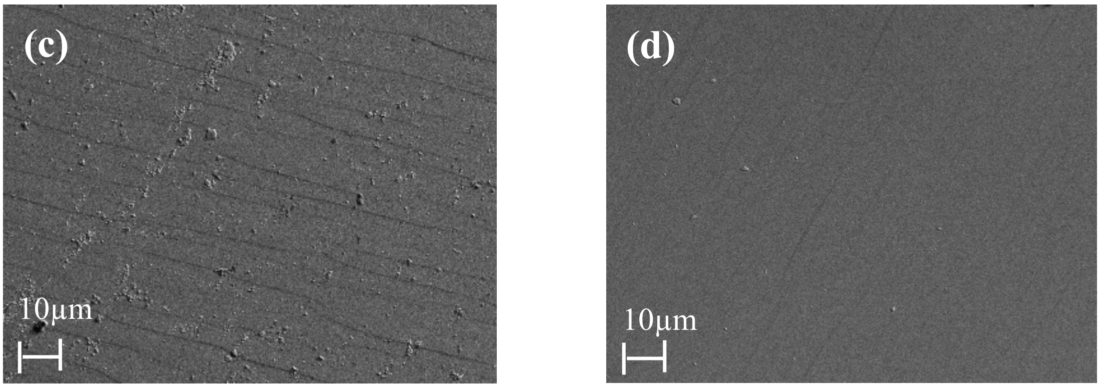

Figure 6.2 SEM image of (a) sample A, (b) sample G, (c) sample H, and (d) sample I.

It is reported in literature that the enhanced surface roughness after plasma etch is due to a preferential loss of nitrogen atoms during chlorine based plasma treatment which can be suppressed by oxygen creating a smoother surface oxide/ oxy-nitride layer [173]. It should be noted that the RF power for O_2 plasma treatment plays a crucial role in the recovery of etched GaN surface [180]. A systematic surface cleaning of 250W BCl_3 etched GaN surface with varying O_2 plasma power from 100 to 300 W is therefore performed. The representative SEM images depicting the variations in surface morphology with in-situ O_2 plasma are shown in figure 6.3. As can be seen from the figure, large number of etch residues remains on the sample surface after 100W O_2 plasma treatment as obvious from figure 6.3 (a) which significantly disappear from the sample surface after 200W O_2 plasma treatment as shown in figure 6.3 (b).

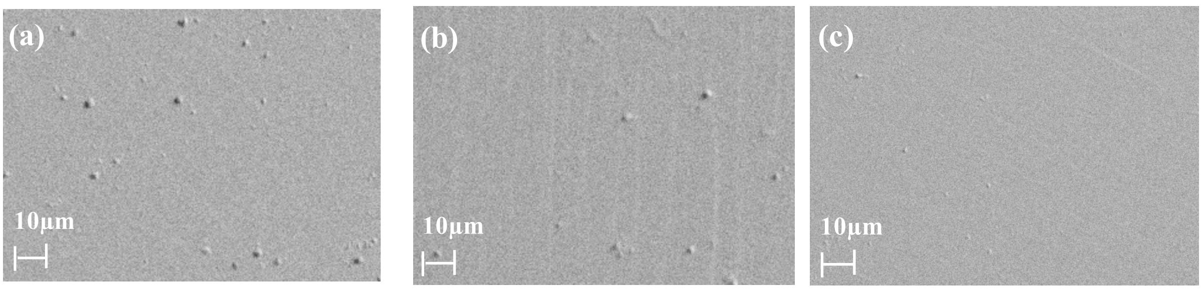

Figure 6.3 SEM image of (a) 100W, (b) 200W and (c) 300W RF O_2 plasma treated GaN samples subsequent to dry etching by 250W RF BCl_3 plasma in the same chamber.

A superior surface morphology with minimum surface roughness is obtained for 300 W RF O_2 plasma treated GaN surface as shown in figure 6.3 (c). Hence, a systematic evaluation of RF oxygen plasma cleaning of the 250 W BCl_3 RF plasma etched GaN surface suggests an efficient surface cleaning using O_2 plasma with RF power of 300 W.

The removal of residues and decrease in surface roughness is of great interest since it would improve the electrical and optical properties of layer. It will help in improving the efficiency of optoelectronic devices fabricated following the dry etch [181, 182]. To understand this in more detail, the optical properties of BCl_3 plasma etched GaN epilayers are studied by performing room temperature PL measurement as shown in figure 6.4. A near band edge emission (NBE) peak corresponding to free exciton (FX_A) recombination appears at 3.41 eV which is accompanied by a phonon replica in all the samples [183]. Further, a very feeble yellow luminescence (YL) band peaking around 2.39 eV can also be identified. No appreciable change in the intensity of YL band is seen even after etching with 250W BCl_3 plasma (sample H).

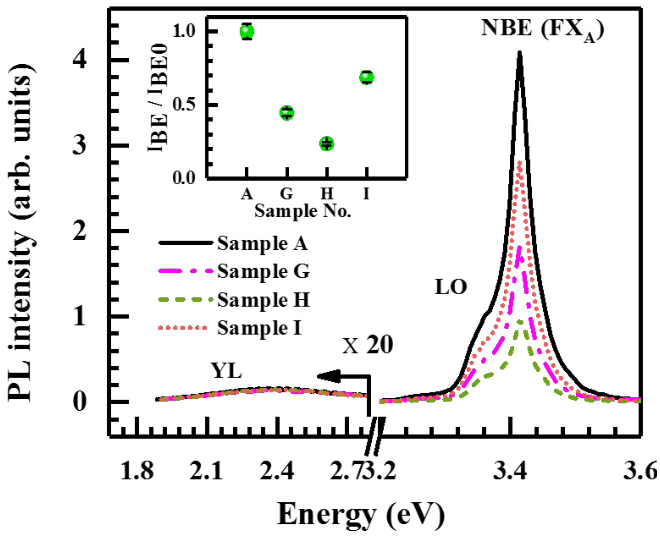

Figure 6.4 Room temperature PL spectra of samples A, G, H and I. Inset shows the corresponding I_{BE} /I_{BE0} ratios where I_{BE} (I_{BE0}) stand for PL intensity of NBE peak of the plasma etched (as-grown) sample respectively. Error bars in inset show the variation of PL intensity at different locations across the samples.

It implies that the radiative recombination centres associated with YL band are distributed over a large depth of GaN layer [184]. From depth dependent PL analysis, Basak *et al*. also concluded that the origin of YL is rather distributed uniformly in epilayer, therefore it will be less perturbed by the plasma etch induced defects which are mostly generated near the surface [185]. It is known that the above band gap photons are strongly absorbed by the material compared to sub band gap photons. Consequently, the escape probability of band edge PL signal generated near the surface is greater than that created deep inside the bulk GaN. Hence, band edge PL signal is expected to be more sensitive to RIE induced surface damage compared to YL band. Under identical excitation, the intensity ratio of NBE emission of as-grown (I_{BE0}) to plasma etched samples (I_{BE}) can be used as a figure of merit for assessing the optical quality of etched GaN surface. Such a plot is shown in the inset of figure 6.4 where a low value indicates a poor optical quality of the sample. It is obvious that the PL intensity of NBE peak reduces with increasing RF power and becomes only 24% of the as-grown sample at 250 W. The observed reduction in the intensity of NBE peak after dry etching indicates generation of non-radiative recombination centres such as V_N defects due to high energetic ion bombardment [75, 186]. Moreover, V_N defect acts as shallow donor which increases the electron concentration. This may also increase the leakage current of GaN based Schottky junction device [186]. Further, a considerable increase in NBE emission is observed after post etch O_2 plasma treatment as shown in case of sample I in figure 6.4. It is reported that O_2 plasma treatment oxidize a large number of Ga atoms segregated at the etched surface [181]. This reduces the effective density of V_N defects and increases the intensity of NBE peak for sample I [181]. Since the plasma etch induced damage and its recovery using O_2 plasma can substantially influence the electrical properties of GaN, impact of dry etching on electrical transport properties of Au/Ni/GaN Schottky junction needs to be investigated. Hence, C-V measurement is performed at room temperature on the plasma etched samples which can be useful to measure the density of ionized carriers at the edge of depletion width. Inverse square of the capacitance ($1/C^2$) of Au/Ni/GaN Schottky diode is plotted as a function of applied reverse bias (V) in figure 6.5. Such a variation is already explained by considering the expression given in equation 2.11. The values of carrier concentration and Schottky junction barrier height obtained from C-V measurements are summarized in Table 6.1. As can be seen from Table 6.1, the barrier height value obtained for sample G and H show a slight reduction from its pristine value in sample A.

Another important observation is that the carrier concentration values obtained from C-V measurements are found to be two orders low compared to the values obtained from Hall measurements. This is due to the presence of a highly conducting interfacial layer with large dislocation density at GaN/sapphire interface which largely dominates the Hall carrier concentration. A detail analysis regarding the presence of this parasitic channel in HVPE grown GaN and its adverse effect on device fabrication is already given in Chapter 3 [19, 90]. Further, the carrier concentration obtained from C-V slightly increases with rise in RF power as shown in Table 6.1. It is also observed that the post etch O_2 plasma treatment does not change the barrier height and carrier concentration value for sample I significantly. One of the possible reasons for this observation may be that the C-V measurements provide the values of transport parameters at the edge of depletion width. Since, the zero bias depletion width is about 250 nm in our sample, it might be possible that the plasma etch induced damage might not influenced the carrier concentration up to such depth making C-V technique quite insensitive to the surface damage. Moreover in C-V measurements, one essentially measures an average barrier height over the entire contact area where sharp variations in barrier height over minuscule domains might not be weighed at all [95, 187].

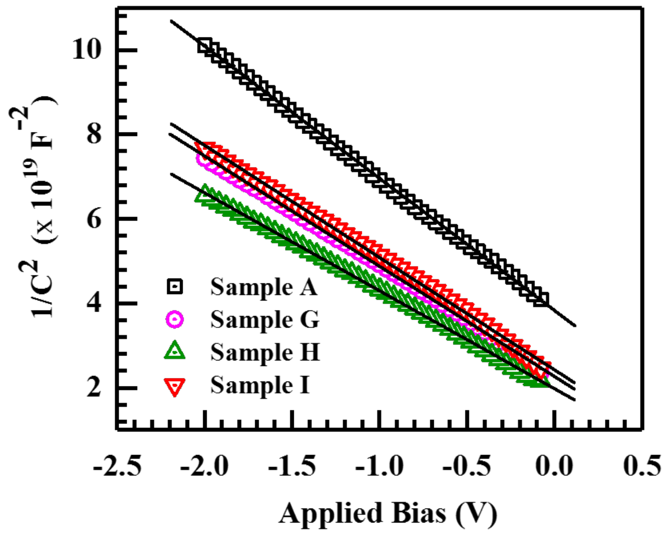

Figure 6.5 An outcome of C-V measurements where $1/C^2$ is plotted as function of applied bias.

Table 6.1 Electrical transport parameters of GaN Samples used in the present work.

Sample No.	RF Power in RIE (W)	Barrier height (eV)	Carrier concentration (cm^{-3})
A	0 (As grown)	1.11 ± 0.03	$1.72 \pm 0.01 \times 10^{16}$
G	150 W	0.98 ± 0.02	$2.44 \pm 0.01 \times 10^{16}$
H	250 W	0.96 ± 0.02	$2.76 \pm 0.01 \times 10^{16}$
I	250 W (post etch O_2 plasma treatment)	1.01 ± 0.03	$2.37 \pm 0.02 \times 10^{16}$

Furthermore, if there are n-type highly doped regions present around V_N cores then carriers can tunnel across those channels. Hence, C-V characteristics might not be significantly affected by the surface tunnelling of carriers because of small size of domains containing V_N cores within the contact area. On the other hand, forward bias I-V characteristic should be largely dominated by the carrier tunnelling if that becomes the primary transport mechanism across Au/Ni/ GaN Schottky junction due to the dry etching step. Room temperature I-V characteristics of all the four samples are shown in figure 6.6.

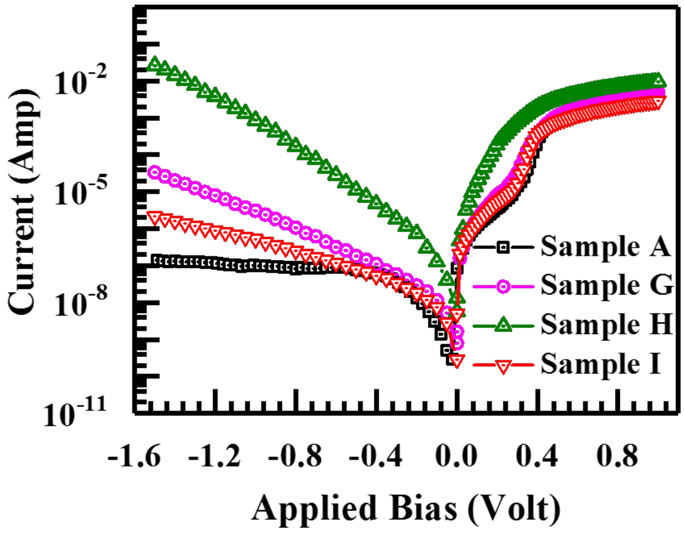

Figure 6.6 Room temperature I–V characteristics of Au/Ni/GaN Schottky diodes.

Table 6.2 Schottky barrier height and carrier concentration estimated from I-V measurements.

Sample No.	RF Power in RIE (W)	Barrier height (eV)	Ideality factor (η_F)
A	0 (As grown)	0.78 ± 0.02	1.02 ± 0.03
G	150 W	0.69 ± 0.02	1.38 ± 0.04
H	250 W	0.54 ± 0.01	1.77 ± 0.05
I	250 W (post etch O_2 plasma treatment)	0.75 ± 0.02	1.17 ± 0.03

First, the measured I-V characteristics is analysed in the intermediate-bias range considering conventional thermionic emission model which is already described in section 2.4.3 of chapter 2. The values of barrier height and ideality factor estimated from the forward bias I-V characteristics using equation 2.15 and 2.17 for all the samples and are shown in Table 6.2. It is obvious from Table 6.2 that the value of barrier height across Au/Ni/GaN Schottky junction monotonically reduces with increase in RF power. After 250W BCl_3 plasma treatment in sample H, 0.24 eV reduction in barrier height is observed with respect to sample A. Further, the ideality factor also shows a considerable increase with RF power. Such an enhancement of ideality factor and fall of barrier height with increasing RF power suggest that the thermionic emission cannot be the primary transport mechanism across the Schottky junction post RIE process [188]. Moreover, a substantial recovery of the values of barrier height and ideality factor post etch O_2 plasma treatment is noted in case of sample I as shown in Table 6.2. It is reported that highly energetic ion bombardment in RIE process causes significant changes in surface stoichiometry by a preferential sputtering of nitrogen leading to the creation of nitrogen vacancies (V_N) at the surface [186]. Since V_N acts as shallow donor, the generation of such vacancies causes the etched GaN surface to be heavily n-type doped, which causes the Fermi level to move inside the conduction band around such isolated regions [169, 174]. As a result, the carriers in these pockets see a thin barrier and hence can easily tunnel through. A large difference in barrier height estimated from C-V and I-V measurements with increasing RF power also supports the assumption that RIE process may promote a strongly localized surface tunnelling of carriers. However, the size of such heavily doped domains is negligible in comparison to the total Schottky junction area, thus making C-V technique to be quite insensitive in probing this behaviour. Moreover, a substantial rise in the leakage current is observed in figure 6.6 for plasma etched samples which also strengthens the understanding that the thermionic emission cannot be the dominant current transport mechanism in post dry etched samples.

For further validation, a quantitative analysis of carrier tunnelling mechanism is essential. In order to explain the observed deviation of forward bias I-V characteristics from the ideal TE model in samples G and H, we consider a tunnelling transport component based on the TFE model proposed by Padovani and Stratton [54]. In TFE model, forward bias current transport in the intermediate bias range is dominated by the tunnelling of thermally excited electrons as already explained in section 1.5.2 of chapter 1. The tunnelling probability for such a process increases exponentially with energy since electrons near the tip of potential profile see a lower and thinner barrier as shown in figure 1.12 [189]. The tunnelling process effectively reduces the height of Schottky barrier under TFE mechanism. The amount of barrier lowering under tunnelling process depends on the dopant density and temperature. The forward bias current ($I_{TFE,F}$) under this model can be expressed as [54],

$$I_{TFE,F} = I_{TFE,FS} \exp\left(\frac{V}{E_0}\right) \tag{6.1}$$

where,

$$I_{TFE,FS} = \frac{A\,A^*\,T^2\,\sqrt{q\pi E_{00}\,(\Phi_B - V + V_n)}}{k_B\,T \cosh\left(E_{00}/k_B\,T\right)} \exp\left[\frac{qV_n}{k_B\,T} - \frac{q\,(\Phi_B + V_n)}{E_0}\right] \tag{6.2}$$

for the forward bias regime where V_n is $(E_C\text{-}E_F)/q$,

$$E_0 = E_{00} \coth\left(\frac{E_{00}}{k_B T}\right) \tag{6.3}$$

Here, E_{00} is the characteristic tunnelling energy which is proportional to $\sqrt{\mathbf{N_D}}$ as already shown in equation (3.11). Note that Φ_B in equation 6.2 is the thermionic Schottky barrier height as given by equation 2.15. The experimental data fitted with equation 6.1 considering TFE model is shown in figure 6.7. First, the forward I-V curve of as-grown sample (sample A) is fitted using thermionic emission model given by equation 2.15 and extract the value of Φ_B. As can be seen from the figure 6.7, a decent fit for sample A is obtained with Φ_B value of 0.81 ± 0.03 eV. However, a different slope of I-V curve is observed in case of other samples.

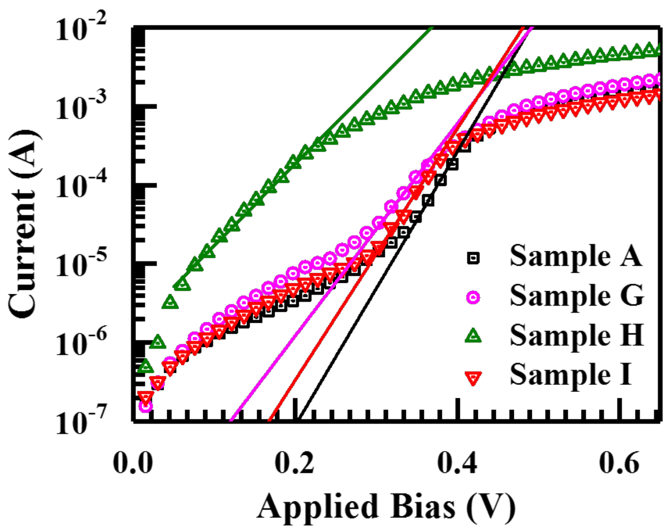

Figure 6.7 Forward bias I–V characteristics of Au/Ni/GaN Schottky diodes in the intermediate bias range before and after BCl_3 plasma etch. The solid lines are the theoretical fit of the forward I-V using equation 6.1.

It implies that thermionic emission is not the primary transport mechanism in those samples. Under such circumstances, the forward bias I-V curves is fitted with equation 6.1 by keeping the value of Φ_B fixed to 0.81 eV as shown in figure 6.7. Here, the slope of the I-V curve is first extracted from the fit which is then used to estimate the value of E_{00}. This helps in measuring the value of N_D. A rise in the value of N_D is directly related to the density of shallow donors generated via V_N defects because of RIE induced surface damage.

Table 6.3 A summary of Schottky junction parameters estimated by using TFE model.

Sample No.	RF Power in RIE (W)	Φ_B (eV)	E_{00} (meV)	N_d (cm^{-3})
A	0 (As grown)	0.81 ± 0.03	----	----
G	150 W	0.81 ± 0.03	22 ± 2	3 ± 0.5 × 10^{18}
H	250 W	0.81 ± 0.03	36 ± 1	8 ± 0.5 × 10^{18}
I	250 W (post etch O_2 plasma treatment)	0.81 ± 0.03	11 ± 1	7 ± 1.0 × 10^{17}

After finding the value of E_{00}, entire theoretical I-V curve is vertically shifted by varying the product (AA^*) such that it matches with the experimental curve. Schottky junction parameters obtained from the curve fitting exercise are shown in Table 6.3.

Few important observations can be immediately made from Table 6.3. First, a high dopant density is measured in plasma etched samples and the values are much higher than those obtained from C-V measurements given in Table 6.1. A large value of dopant concentration is in good agreement with the understanding that TFE mechanism assisted by the tunnelling of thermally excited carriers dominates the electronic conduction in dry etched samples. Second, it should be noted that the critical carrier concentration at which Fermi level moves into the conduction band in GaN is 2×10^{18} cm^{-3} [190]. Hence, with increasing RF power (sample G to H), Fermi level moves deeper into the conduction band leading to a further high value of E_{00}. It is well known that an upward trend in the value of E_{00} with respect to k_BT signifies the dominance of carrier tunnelling [72]. However, a substantial reduction in E_{00} and hence in N_D is obtained in case of sample I as shown in Table 6.3. Such an observation explains why one sees a major recovery of the reverse bias leakage current in sample I as shown in figure 6.6.

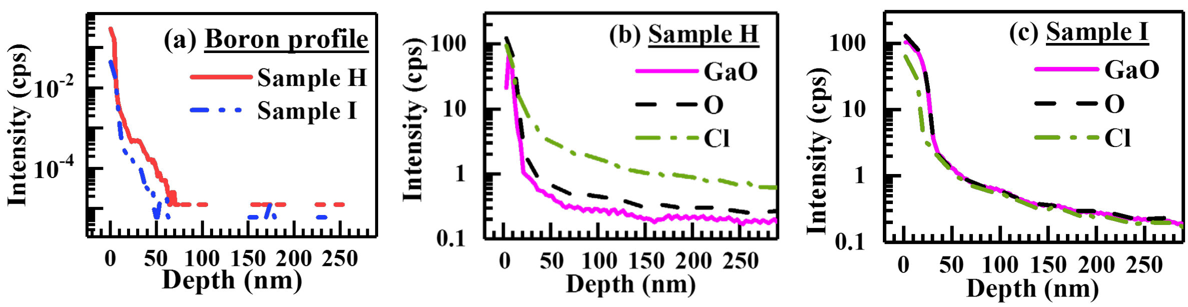

Figure 6.8 SIMS depth profile for (a) boron in sample H and I (b) GaO, O and Cl in sample H and (c) GaO, O and Cl in sample I. Intensity of boron in figure 6.8 (a) is normalized by the intensity of Ga_2 secondary ion signal whereas the secondary ion intensity of all the negative ions in figure 6.8 (b) and (c) are normalised by the intensity of Ga secondary ion signal in order to minimize the instrumental errors.

O_2 plasma considerably oxidized a large number of extra Ga atoms on the etched GaN surface, resulting in a substantial reduction in the density of V_N and hence the extent of carrier tunnelling in a region around V_N [181]. Considering the effective area over which carrier tunnelling takes place to be very small compared to the actual area of Schottky diode, and inability of C-V technique in probing the strongly localized carrier tunnelling within the depletion region, it is quite understandable why C-V measurements are insensitive to RIE induced changes in dry etched samples [95]? To investigate the later possibility in more detail, we analyse the extent of depth up to which RIE induced damage severely affect the sample characteristics via SIMS measurements. SIMS measurements are performed on the two selected samples (H and I) due to the obvious reasons that one expect maximum RIE induced damage in sample H while Sample I has shown a sign of recovery post O_2 plasma treatment. Hence, a comparison of the extent of RIE induced damage in these two samples is of worth. SIMS depth profiles corresponding to B, GaO, O and Cl are shown in figure 6.8. It is evident from figure 6.8 that a large change in all the SIMS profiles appears mostly within first 100 nm of depth which affirms our previous assumption that plasma induced damage is rather shallow and is confined to the vicinity of sample surface. Note that a thin layer of boron is detected close to the surface in both the samples and boron content is much higher in sample H when compared with sample I as obvious from figure 6.8 (a). Further, presence of chlorine atoms is detected at much larger depth when compared with boron as obvious from figure 6.8 (a) and (b). The observed features related to B and Cl secondary ions in sample H and I can be explained by noting the fact that the GaN sample was placed at negatively biased electrode which was bombarded by positively charged ions. It can be reasonably assumed that the particles that are bombarded on GaN surface are positively charged BCl_x (x = 1–2) radicals.

A fraction of these ionized radicals are implanted in GaN layer which causes the observed rise in SIMS signal corresponding to B and Cl secondary ions. It is already known that Cl reacts with GaN surface to form $GaCl_x$ (x = 1-3) which is then adsorbed on GaN surface [191]. Further, a strong suppression of Cl signal is observed in case of sample I due to oxygen plasma as obvious from a comparison of figure 6.8 (b) and (c). At the same time, signal corresponding to GaO and Oxygen species rises post O_2 plasma treatment. It suggests that BCl_3 related contaminates at GaN surface are effectively removed by O_2 plasma treatment. Further, $GaCl_x$ (x = 1-3) species incorporated in sample H are considerably reduced and more stable GaO is formed post O_2 plasma treatment. A large concentration of Oxygen bonded with Gallium is already reported in literature post O_2 plasma treatment [181]. This causes an effective surface passivation of plasma etched GaN surface reducing the carrier tunnelling and improving the leakage current under Au/Ni/GaN Schottky junction as seen earlier in figure 6.6 and 6.7.

Next the impact of plasma etching on the charge collection efficiency of GaN based Schottky photodiodes is studied. Photoresponse curves of Au/Ni/GaN Schottky photo diodes fabricated on the as-grown (sample A), plasma etched (samples G and H) and post etch O_2 plasma treated (sample I) samples are compared in the spectral range of 320-400 nm as shown in figure 6.9. It is observed that the peak spectral response (~360 nm) reduces by 50% in sample G and by 90% in sample H. Such a sharp fall of photoresponse can be attributed to the reduction of charge collection efficiency due to the generation of non-radiative recombination centres by the plasma etching. Note that the intensity of excitonic feature (~360 nm), which is clearly visible in as-grown sample, diminishes in sample G and no such peak is observed in case of sample H. Plasma induced defects and inhomogeneity in the material broadens the excitonic density of states which leads to such an observation.

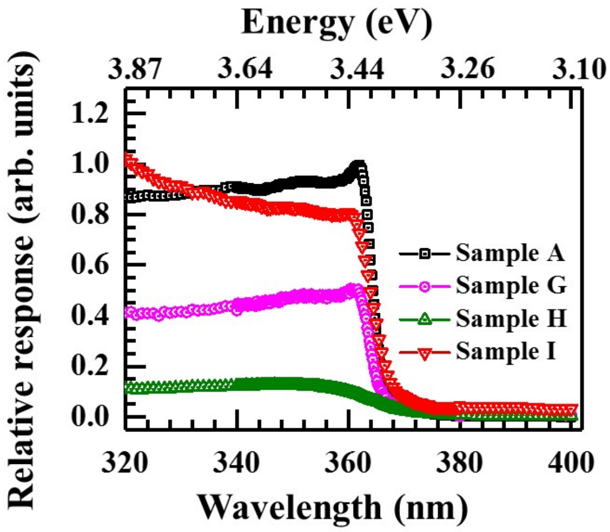

Figure 6.9 Plasma etching induced degradation and post etch O_2 plasma treatment induced recovery of photo response of Au/Ni/GaN Schottky photodetector.

It goes in line with our earlier observation in figure 6.4 where intensity of NBE peak located at 3.41 eV is seen to fall by more than 75% in case of sample H. Interestingly, the NBE photo response considerably recovers after post etch O_2 plasma treatment in sample I. Moreover, the device response significantly enhances in the above band gap region due to an effective surface passivation by O_2 plasma. In particular, the photoresponse below 330nm is larger than the value recorded in case of as- grown GaN sample. It clearly shows a systematic improvement made in the photoresponse of detectors subsequent to the O_2 plasma treatment which validates the usefulness of the process [192, 193]. Similarly an improvement in the detectivity by an order of magnitude is also observed post O_2 plasma treatment. This observation is strongly supported by the SIMS measurement where a strong suppression of Cl signal along with enhancement in GaO and Oxygen is obtained in post O_2 plasma treated sample I as shown in figure 6.8 (b) and (c). These results suggest that the BCl_3 plasma etch induced surface damage, which causes the reduction in above band edge photoresponse, is not only recovered considerably after O_2 plasma treatment but also stable GaO is formed on the etched GaN surface which thereby passivates the surface defects and improves the above band edge photo response.

Further, in order to compare the response speed among different photodetectors, the transient response of the fabricated devices are measured, by switching the UV excitation on and off. The UV illumination intensity of 9 mW /cm^2 was used as the UV light source while keeping the device geometry unaltered throughout the experiments. Figure 6.10 represents the rise and decay transients from where the time constants are estimated by using the fitting of exponential rise and decay curves. The rise and decay curves are fitted using the exponential rise and decay equations 2.26 and 2.27. The values of the transient photoresponse parameters estimated for dry etched and post etch O_2 plasma treated samples are tabulated in Table 6.4. As can be seen from the table, there is a faster (τ_1) and a slower (τ_2) component of decay constant obtained for sample A. Whereas for 250W RF plasma etched sample H, the faster component merge in to the slower component and the entire rise and decay curve can be fitted considering only a single value of τ. This indicates that the photo generated carriers are captured by the dry etch induced defects where they might recombine non-radiatively leading to a slower response to the applied electric field.

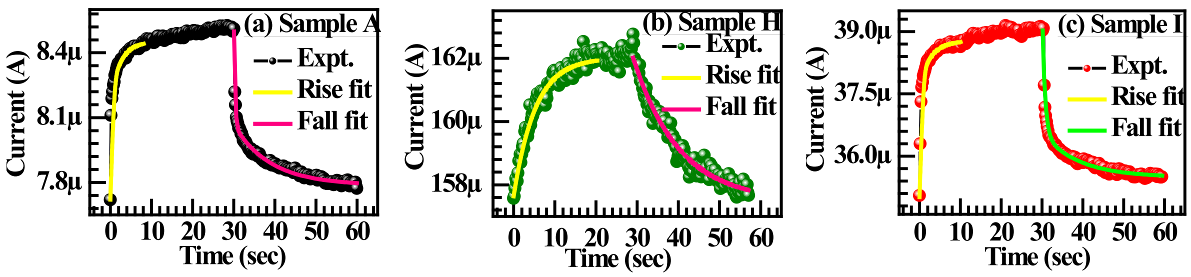

Figure 6.10 The time response of the photocurrent measured at reverse bias 2V for (a) sample A , (b) sample H and (c) sample I.

Table 6.4 The rise and decay time constants calculated for different dry etched samples.

Sample No.	RF Power in RIE (W)	Rise time constant		Decay time constant	
		τ_1 (ms)	τ_2 (s)	τ_1 (ms)	τ_2 (s)
G	150 W	128	2.4	243	9
H	250 W	----	5.2	----	11
I	250 W (post etch O_2 plasma treatment)	275	2.8	682	9

However, the situation improves after post etch O_2 plasma treatment in sample I where a considerable improvement in the value of τ_2 along with the reappearance of fast component with enhanced value of τ_1 confirms our previous understanding that the O_2 plasma treatment has a major role in an overall recovery of the optoelectronic properties and photo response of GaN Schottky photodetector.

6.4 Fabrication of GaN PIN detector using RIE

After developing an in-depth understanding on the extent of damage created by plasma etching on the surface morphology, optical and electrical properties of GaN and a method of recovery of the damage by O_2 plasma treatment, the immediate aim is to fabricate a GaN PIN detector using RIE. For this purpose, HVPE grown GaN PIN structure is commercially procured with device structure of: Sapphire/2 µm undoped GaN /500nm GaN:Si (N-layer) / 3.5 µm undoped GaN (I-layer) /350nm GaN:Mg (P-layer). Figure 6.11 shows the schematic diagram of GaN PIN detector. It also presents the depth profile of major dopants present in the epitaxial structure performed using SIMS technique. Note that, the data on y-axis is not calibrated to the impurity concentration due to the lack of standard samples in SIMS lab. Hence, a quantitative analysis of the dopant concentration present in the p and n-layer is not possible.

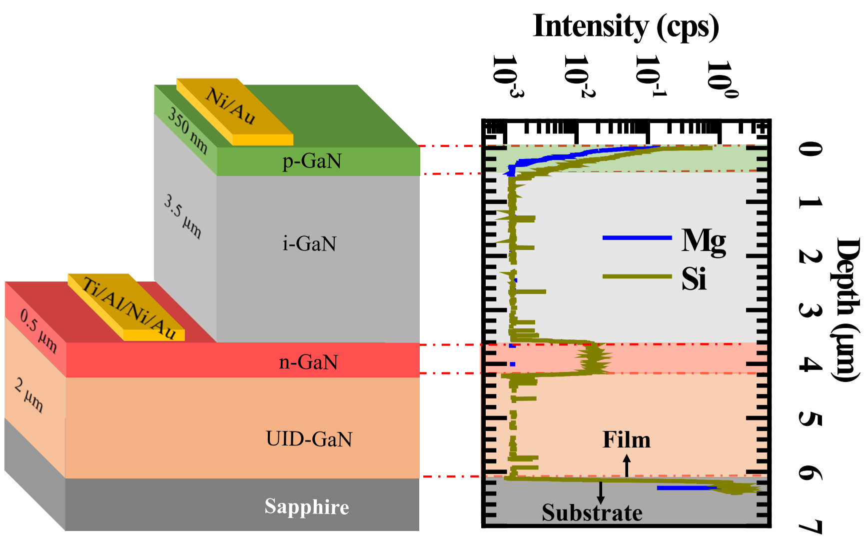

Figure 6.11 Schematic diagram of GaN PIN detector along with SIMS profile showing the major dopants profile of Mg and Si for the p and n-GaN layers respectively.

However, as can be seen from the figure, the intensity of Mg signal remains below the detection limit of the SIMS instrument in the entire depth profile other than in the p-GaN layer. Similarly, one order increase in the intensity of Si dopant can be observed in the 0.5 μm thick n-GaN layer. Thus, the SIMS profile of Si and Mg dopants confirm that the epitaxial structure matches well with the design of the PIN detector structure.

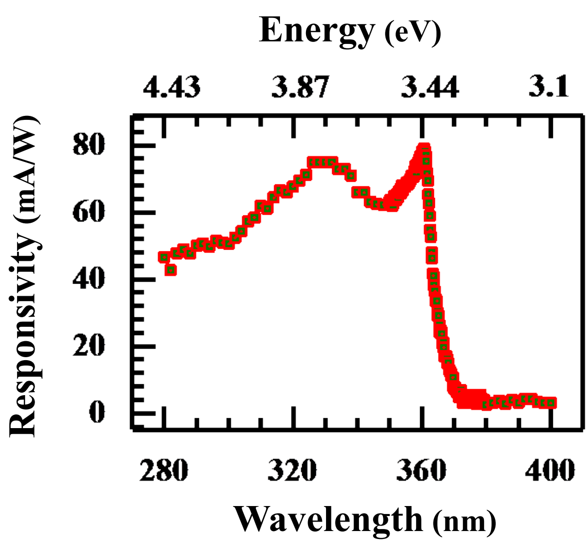

Figure 6.12 Room-temperature spectral response of GaN PIN detector at an applied bias of 0.5V.

Fabrication of PIN detector is initiated with mesa formation using RIE. Here, SiO_2 is used to mask a portion of about 5×5 mm^2 sample. BCl_3/N_2 (10 /10 sccm) plasma with RF power of 150W is used for the mesa etching upto the bottom n-GaN layer. Other parameters during the etching process are kept same as already discussed earlier in section 6.2. After mesa formation, Ti/Al/Ti/Au and Ni/Au metal stacks are deposited by thermal evaporation technique and subsequently annealed at 850°C for the Ohmic contact formation with n and p-GaN layers, respectively. The width of p and n-contacts are 200 µm and separation between the contacts is 250 µm. The spectral response of the PIN detector is recorded over the spectral range of 280–400 nm at an applied bias of 0.5V and power density of 0.5 mW/cm^2 and is shown in figure 6.12. It can be observed that the peak responsivity is located at about 362 nm and the cut-off wavelength is located at about 370 nm. The peak responsivity at 0.5 V applied bias is measured to be 80 mA/W. The value of D* of the device is also estimated considering shot noise as the limiting factor in D* and it is found to be 6×10^{11} Jones which is considerably higher than the D* achieved in GaN MOS detector as discussed earlier in chapter 5.

6.5 Conclusion

In conclusion, the impact of RIE induced damage on the optoelectronic properties of epitaxial layer and photoresponse of Schottky photodetector is demonstrated. Surface morphology is observed by SEM which shows a large degradation with increasing ion energy. More than 70% reduction in the intensity of NBE PL peak after 250W RF plasma etching along with etch insensitive YL band suggests that etch induced non-radiative centres are located rather close to the surface of sample. This observation is further supported by C-V measurements on Au/Ni/GaN Schottky diodes which along with SIMS results confirm that the RIE induced damage is mostly confined within 100 nm from the surface of GaN layer. Further, clear evidence of carrier tunnelling across plasma etch induced heavily doped n-type pockets within the area of Schottky contact is revealed using TFE model. It is proposed that the generation of V_N defects post plasma etching over small size domains leads to heavily doped n-type regions thus shifting the Fermi level deep inside the conduction band locally to enable the carrier tunnelling. The peak spectral response of Au/Ni/GaN Schottky photodetector also shows upto 90% reduction post plasma etching. Further, a method for the recovery of plasma etch induced damage by O_2 plasma treatment is also demonstrated. A substantial recovery of the spectral and transient response and along with an improved deep UV response of photodetector is achieved through O_2 plasma treatment. Using the optimized etch parameters, mesa etching is performed to fabricate GaN PIN detector. The spectral response of the detector is recorded over the spectral range of 280–400 nm showing a peak responsivity of 80 mW/A at 362 nm and a high value of D* of 6×10^{11} Jones which is found to be better than that of GaN MOS detector. The results presented here are helpful in gaining the required understanding of RIE induced damage and also in the minimization of plasma etch induced degradation in optoelectronic properties of GaN epitaxial layer and spectral response of Schottky photodetectors.

Chapter 7

Impact of Gamma Irradiation on the Performance of GaN Photodetectors

7.1 Introduction

One of the major aims of this thesis is to test the performance of photodetectors under high radiation environment and the same is discussed in this chapter. Since nitride devices are more radiation tolerant than Si and GaAs based devices, they are suitable candidate for applications in high radiation environments like nuclear reactors, particle accelerators and spacecraft as mentioned earlier in chapter 1. Study of high-energy irradiation induced defects on the operational characteristics is an essential objective for estimating the long-term reliability of GaN based optoelectronic devices under harsh radiation environment. Exposure of GaN semiconducting layers to high energy radiation/particles leads to the creation of vacancy and interstitial point-defects through the displacement of Ga and N atoms from their respective lattice sites. It introduces new energy levels in the forbidden gap which act as scattering centres and can either be donor, acceptor or recombination centres. However, isolated defects may endure thermally activated defect migration and formation of defect clusters through interaction among themselves and also with the native defects even at room temperature. Such an observation was made by Chow *et al.*, where interstitial Ga defects generated by 2.5 MeV electrons were found to be stable at low temperature which became mobile at room temperature [194]. Since the probability of cluster formation is enhanced by the presence of native defects in material, effect of irradiation induced defects on the electrical transport properties critically depends on the background carrier concentration [195]. Though a large amount of literature is available on the effect of irradiation on moderately doped GaN, a systematic study on the electronic transport in heavily doped n-type GaN is missing. Only one group have reported that the effect of Gamma (γ) radiation induced defects in GaN varies as a function of carrier concentration. However, no efforts were made by them to understand the origin of defects [195]. In chapter 3, it is shown that the carrier transport in n^+-GaN epilayers can be significantly influenced by the presence of charge dislocations that are generally present at GaN/Sapphire interface [19]. Therefore, the impact of irradiation induced defects on electrical transport is not a trivial matter since interfacial transport of carriers might dominates over the thermally activated bulk transport in specific cases. This aspect is not yet highlighted while studying the effect of irradiation on heavily doped n-type GaN samples.

In this chapter, effect of γ-radiation on the electrical transport in heavily doped n-type GaN is meticulously studied by considering the effect of interfacial dislocations. Experiments are conducted by irradiating the GaN samples with varying gamma (γ) ray dose. Contribution of interfacial dislocations in carrier transport is isolated from that of the bulk layer in both pristine and irradiated GaN samples using the two-layer model. Activation energy of defect levels is estimated by using the charge balance equation. It allows to comment about the microscopic origin of radiation induced defects in a comprehensive manner. Further, the effect of radiation induced defects on the performance of GaN based Schottky devices is analysed and demonstrated to be less significant as comparted to GaAs based Schottky devices. Importance of greater radiation tolerance of GaN based optoelectronic devices is also manifested through self-recovery within a day after irradiation even with a sizable dose of ^{60}Co γ rays.

7.2 Device fabrication details

The impact of γ irradiation on the electrical transport of GaN epitaxial layer is investigated on HVPE grown sample A. Sample details are already given in chapter 2. Hall measurements are performed after γ irradiation using Van der Pauw geometry at 1 mA current and under 0.4 Tesla magnetic field [19, 196]. For studying the effect of irradiation induced damage on Schottky diode properties, Ni /Au Schottky contact pads are deposited on GaN using thermal evaporation technique under a base pressure of 4×10^{-6} mbar through a metal mask of circular dots of 0.8 mm diameter. Photo-response of the device is measured in ring contact geometry where Ti / Al / Ni / Au multi-layer Ohmic contacts are fabricated using metal mask (ring type) and are subsequently annealed at 850°C for 45 second under nitrogen ambient. Afterwards, Ni /Au Schottky contacts are deposited in the centre of ring as shown in figure 7.1. Since Sapphire substrate is insulating, both Ohmic and Schottky contacts are fabricated on the top of GaN epilayer as shown in figure 7.1. Room temperature γ-irradiation is carried out in a 2490 Curie ^{60}Co γ-chamber and electronic transport experiments are carried out immediately after the exposure.

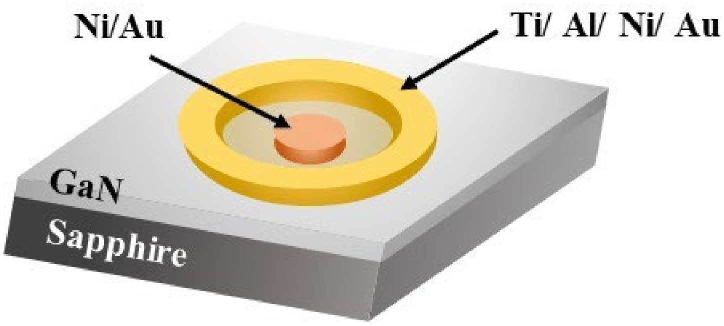

Figure 7.1 Schematic diagram of GaN UV photodetector.

In order to evaluate the impact of self-recovery, transport measurements were performed at room temperature within 15 minutes of irradiation. After this, sample was cooled down to 50 K and temperature dependent data was collected within ~4 hours. In the end, measurements were again repeated at room temperature. No appreciable difference was observed between the two room temperature measurements. Note that the sample was kept at low temperature during most of the measurement period. Hence, chances of self-recovery are rather low during the period of measurements. Typical dose rate of irradiation system is 1 kGy/hr. More details about the γ-radiation chamber are reported elsewhere [104, 197]. In this chapter, wherever dose is mentioned, it is the total dose emitted by the ^{60}Co source to which the samples are exposed. Since the attenuation length of ^{60}Co γ in GaN is large (~ 1 cm) in comparison to the thickness of GaN sample (5μm), it can be safely assumed that the entire device is uniformly irradiated.

7.3 Effect of irradiation on GaN epitaxial layer

In order to understand the effect of ^{60}Co γ-radiation on the carrier concentration and mobility of GaN epitaxial layers, temperature dependent Hall measurements are performed over a wide temperature range varying from 60 to 300 K and the results are shown in figure 7.2. It is observed that the carrier concentration increases while mobility decreases with rise of radiation dose. An important observation of the present study is the unusual behaviour of carrier concentration and mobility at temperature below 80 K. In the low temperature range, the carrier concentration slightly increases and then remains almost independent of temperature. Further, the rise of carrier concentration is more prominent in case of irradiated samples. Such an observation confirms the presence of a degenerate, n-type shallow donor level with high density of dislocations at GaN/ sapphire interface [19, 85, 104].

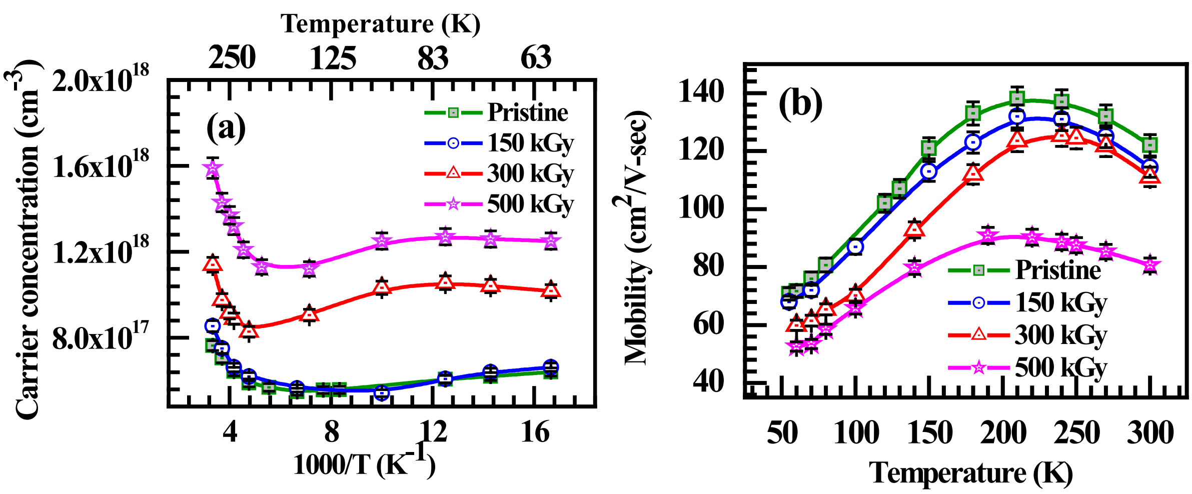

Figure 7.2 Temperature dependence of (a) carrier concentration, and (b) mobility for the pristine and ^{60}Co γ-irradiated samples. The data points are shown with 3% error bar that includes both the statistical and instrumental errors.

This phenomena is already discussed in detail in section 3.3 of chapter 3. Particularly at low temperature, when electrons are frozen on their parent donors, electrical conduction is dominated by carriers activated from the temperature-independent interfacial donor level.

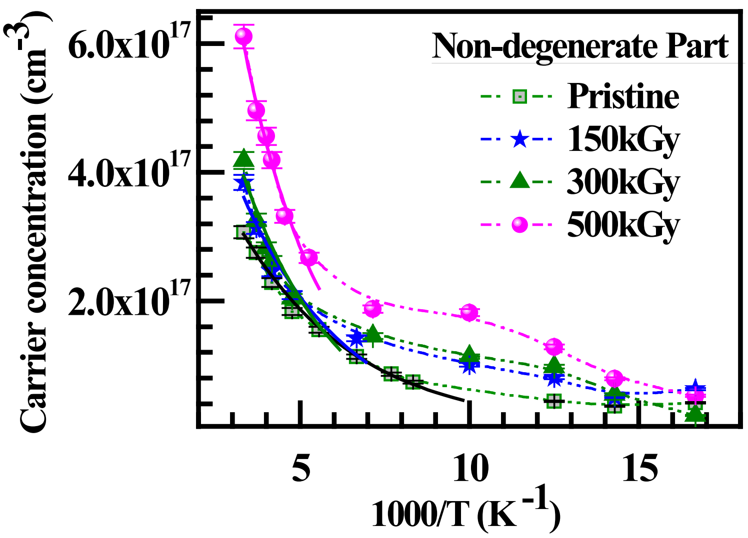

Figure 7.3 Temperature dependent carrier concentration before and after ^{60}Co γ-irradiation extracted from the uncorrected Hall data in figure 7.2 using Look's model [83] where solid lines represent numerical fit to the experimental data over a selective temperature range using equation 7.1. The data points are shown with 3% error bar that includes both the statistical and instrumental errors.

Further, a two-layer model given in equation 3.2 and 3.3 [83] is used to separate the contribution of temperature dependent and independent part of carrier concentration from the measured values of carrier concentration in Hall data [19, 104]. Assuming the temperature independent carrier concentration and mobility to be the contribution arising from the degenerate donor level at interface, the contribution of non-degenerate donor energy level in the measured carrier concentration is extracted and is plotted in figure 7.3. As can be seen from this figure, a pronounced increase in thermally activated carrier concentration is observed after irradiation.

An important observation can be made from figure 7.3, where carrier density is found to increase monotonically with irradiation at a given temperature. It is a unique observation since most of the researchers report a clear fall of carrier density subsequent to irradiation. It includes studies based on γ and electron irradiation, since the nature of irradiation induced defects are quite similar in both the cases [60]. For example, in electron irradiated samples with moderate doping (~10^{16}-10^{17} cm^{-3}), both the carrier concentration and mobility decrease with irradiation [87, 198, 199]. On irradiation with high energy electron (~0.7-1 MeV), Look *et al*. showed that the room temperature carrier concentration was reduced from 8.4×10^{16} cm^{-3} to 6.9×10^{16} cm^{-3} via the creation of N Frenkel pairs involving V_N shallow donors and N_I deep acceptors where radiation induced donor level lie at around 60 meV below the conduction band edge [60]. It is only in the articles from Ioffe Institute, Russia [195, 200, 201] where a rise in the carrier concentration with γ-irradiation is reported for heavily doped GaN samples. It is also reported by them that the electron concentration decreases after γ-irradiation for slightly doped epilayers, while it increases for heavily doped GaN epilayers [195]. However, no reason for the same is given by the respective authors. Nevertheless, it gives enough indications that the nature of temperature dependent carrier concentration profile of γ-irradiated GaN samples is somehow associated with the donor concentration of GaN sample. A quantitative analysis is therefore necessary to understand such a complex observation. Since both the degenerate and non-degenerate part of carrier concentration increase after γ-irradiation, the origin of donor levels giving rise to present observations in both the regions are investigated separately. To estimate the activation energy and dopant concentration of thermally activated donors in pristine and irradiated samples, the non-degenerate part of the carrier concentration shown in figure 7.3 is fitted by the charge balance equation [60, 87]:

$$n + N_A = \frac{N_D}{1 + n/\phi} \tag{7.1}$$

where $\phi = (1/2)N_C^{/}T^{3/2}\exp(-E_D/kT)$. Here $N_C^{/}$ is the effective density of states at 1 K ($N_C^{/}$ = 4.98×10^{14} cm^{-3} for m* = 0.22 m_0), N_D and E_D are the donor concentration and donor energy level, N_A is the acceptor concentration [60, 87]. A single donor fit of the carrier concentration profile of pristine sample is also shown in figure 7.3. This gives N_{D1}= (6 ± 0.2) ×10^{17} cm^{-3}, E_{D1}= 32 ± 1 meV and N_A= (1 ± 0.5) ×10^{16} cm^{-3}. While fitting the irradiation induced carrier concentration data, we surprisingly found that no new donor levels are needed to be considered. Rather, all the data can be fitted by considering the activation of single donor level located at about 32 meV. Note that the value of N_D increases by several folds in case of 500 kGy irradiated sample when compared with the pristine sample, as shown in Table 7.1.

Table 7.1 Electrical transport parameters before and after ^{60}Co γ-irradiation obtained by fitting the experimental data shown in figure 7.3 with equation 7.1.

Dose (kGy)	N_{D1}(cm^{-3})	E_{D1}(meV)	N_A(cm^{-3})
Pristine	6 ± 0.2 ×10^{17}	32 ± 1	1 ± 0.5 ×10^{16}
150	9 ± 0.5 ×10^{17}	32 ± 1	7 ± 1 ×10^{16}
300	1.3 ± 0.5 ×10^{18}	32 ± 1	2 ± 0.5 ×10^{17}
500	2.6 ± 0.2 ×10^{18}	32 ± 1	3 ± 1 ×10^{17}

It should be noted here that the values of measured parameters are free from the influence of interfacial layer and are solely governed by the donors present in bulk GaN layer. It is known that Si impurities act like shallow donors in GaN where activation energy of 30.18 ± 0.1 meV is reported in case of HVPE grown GaN samples by Moore *et al*. [202]. Hence, the defect levels identified in pristine sample in our case correspond to Si impurities. It is also known that ^{60}Co γ-radiation gives rise to appearance of point defects like vacancies and self-interstitials. For example, Umana-Membreno *et al.* [203] reported generation of γ irradiation induced three shallow donor levels located at about 88, 104 and 144 meV which they attributed to nitrogen–vacancy related defects. On the other hand, Look *et al.* reported generation of (V_N –N_I) Frenkel pairs with V_N as shallow donors and N_I as deep acceptors while irradiating moderately doped GaN samples with 1 MeV electrons. Look *et al.* [60, 87] reported that the defect donor lies 60-80 meV below the conduction band.

However, in this case, the activation energy of donor level remains constant at 32 meV, even after irradiation with 500 kGy radiation dose. Note that the donor level of same activation energy also exists even in the pristine sample which is associated with Silicon impurity. This indicates that either no new electrically active defects are generated or their activation energy is close to that of the Silicon donors. Rise of donor concentration in irradiated samples can be understood in terms of the activation of radiation induced electrically inactive complexes via their interaction with native defects. Activation of Si donors, which are present in the pristine sample in electrically inactive form, by γ-irradiation is the main mechanism behind this observation. Such a hypothesis is already proposed in GaN [195], and GaAs [204] materials.

Next, it is worth to discuss the effect of ^{60}Co γ-irradiation on the temperature independent degenerate carrier concentration where the measured value increases from 6×10^{17} to 1.2×10^{18} cm^{-3} after exposure to 500kGy dose as shown in figure 7.2 (a). Note that in the low temperature region (< 150K), a degenerate interfacial layer lying at GaN/Sapphire interface dominates the conduction process. One finds in figure 7.2 (a) that the carrier concentration first increases and then becomes almost constant in the low temperature range. This is a clear indication of the presence of a degenerate layer in our sample. Such an observation is already made by several other researchers [19, 60, 83, 85, 87]. Under such conditions, the low temperature Hall data shown in figure 7.2 (a) shall be corrected for a low value of degenerate layer thickness which is reported to be of the order of 0.3 μm [60, 85]. One gets a typical value of low temperature carrier concentration of the order of $1x10^{19}cm^{-3}$ (pristine) by using 0.3 μm as the layer thickness. This clearly supports the presence of a degenerate layer in the present sample. However, such a correction is not essential since 1) it will create confusion because the sheet density obtained from Hall measurements needs to be divided by the two different thicknesses in the two temperature ranges, 2) one needs to consider different thicknesses of the two layers for estimating the value of carrier concentration under parallel conduction method given in [83]. Further, the exact values of interfacial layer thickness and temperature where transition from degenerate to non-degenerate occurs are not known. Moreover, it doesn't pose a serious limitation for understanding the response of GaN layers to radiation exposure where the overall trends will remain rather unaltered irrespective of the condition whether that the particular correction is incorporated or not. Since, the carrier concentration increases with radiation exposure as shown in figure 7.2 (a), the Fermi level moves further up in the conduction band at low temperature. Considering the movement of Fermi level with radiation exposure, it can be concluded that the radiation induced degenerate donors in our sample are rather shallow. Further the origin of such a temperature independent donor behaviour is related to the diffusion of oxygen impurities occupying nitrogen site. High energy γ irradiation enhances the probability of formation of nitrogen vacancies increasing the rate of oxygen impurity diffusion at the interface [84]. It leads to a substantial increase in density of interfacial donors and hence carrier transport through the GaN/sapphire interface.

7.4 Effect of Gamma irradiation on GaN Schottky diodes

The defect complexes produced by γ irradiation in GaN are expected to affect the performance of Schottky diodes. In order to get a quantitative estimate of damage, I-V characteristics of pristine and irradiated Au/Ni/GaN Schottky diodes are compared at room temperature as shown in figure 7.4. The reverse I–V characteristics shown in figure 7.4 manifest a gradual degradation of Schottky contact with increasing radiation dose. At a reverse bias of 2V, the leakage current increases from a pre-irradiation level of 6.5×10^{-7}A to 7.7×10^{-5} A after exposure to 450 kGy of ^{60}Co γ-radiation. Such a large increase of leakage current is a direct consequence of radiation induced activation of defects. In addition to this, the radiation induced degradation of Schottky junction parameters like ideality factor and barrier height is also studied from the forward I–V characteristics. In the forward bias region, each plot consists of a linear region with varying slope over an intermediate-bias range. The measured I-V characteristics can be analysed by using the conventional TE model which is described by the equations 2.14 - 2.17.

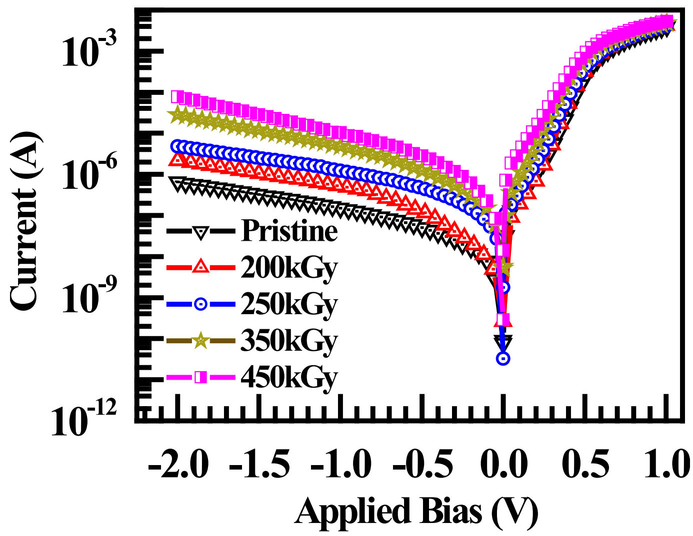

Figure 7.4 I–V characteristics of Au/Ni/GaN Schottky diodes before and after exposure to ^{60}Co γ rays.

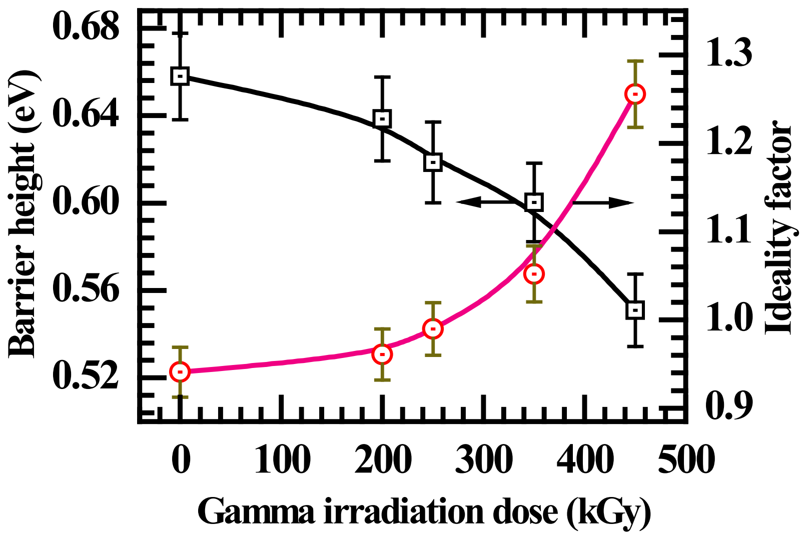

Figure 7.5 Room temperature Schottky barrier height and ideality factor as a function of γ irradiation dose determined from the forward I-V characteristics. The data points are shown with 3% error bar that includes both the statistical and instrumental errors.

The variation of ideality factor and barrier height as a function of ^{60}Co γ-radiation dose obtained from forward bias I-V characteristics using equations 2.14 - 2.17 are plotted in figure 7.5. As can be seen, the barrier height value of pristine GaN sample is much lower than the theoretical Schottky-Mott barrier height of 1.04 eV for Ni/GaN contact [82]. A similar deviation of the estimated values of Schottky junction parameters from theoretically predicted values is already reported by other researchers [91, 93]. Surface states, interfacial defects, material non-uniformity, dislocation-related current paths etc. are proposed to be linked with this kind of non-ideal behaviour of Schottky junction parameters [90, 91, 205]. In addition, a non-ideal behaviour modifies the ideality factor significantly. Irradiation induced defect complexes enhance the current flow through the non-ideal paths, which further decrease the barrier height and enhance the ideality factor. It is clearly observed in figure 7.5, where the barrier height decreases from 0.66 (± 0.02) eV to 0.56 (± 0.016) eV while the ideality factor increases from 0.94 (± 0.03) to 1.26 (± 0.04).

The radiation induced modification of current transport mechanism is expected to be more prominent at low temperature where thermally activated carriers freeze on their parent dopant atoms and carrier transport is mainly governed by carrier tunnelling. To investigate this point further, temperature dependent I-V characteristics for pristine and 300kGy irradiated samples are performed. The estimated values of barrier height and ideality factors are shown in figure 7.6 (a) and (b) respectively. As obvious from figure 7.6 (a), the barrier height decreases on lowering the temperature for both pristine and irradiated samples. Reduction in barrier height endorses the fact that the tunnelling contribution to current transport increases at low temperature which is already discussed in chapter 3 and 4. However, the effect of irradiation is more evident in the temperature dependence of ideality factor [206]. For both, irradiated and pristine samples, the ideality factor increases monotonously on lowering the temperature as shown in figure 7.6 (b). However, the two curves are well separated at low temperature and their separation decreases with rise in temperature.

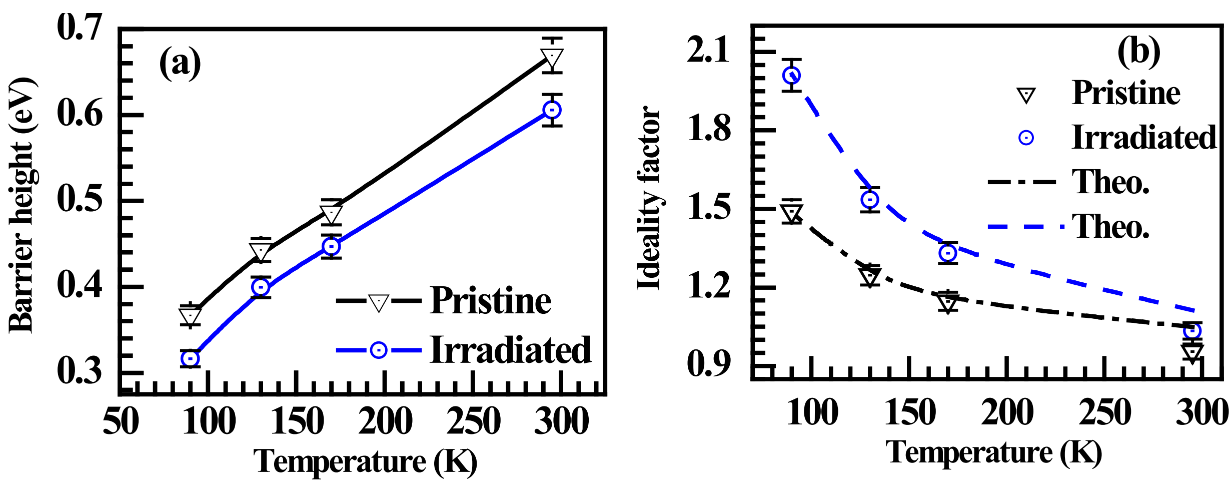

Figure 7.6 (a) Variation of barrier height with temperature for pristine and γ irradiated samples obtained from the temperature dependent I-V characteristics of Au/ Ni/ GaN Schottky diodes, (b) Ideality factor plotted as a function of temperature for pristine and 300 kGy irradiated sample. The dash-dot/dashed lines show the numerically calculated curves using the two values of characteristic tunnelling energy (E_{00}). The experimental data points are shown with 3% error bars that include both the statistical and instrumental errors.

The carrier transport mechanism responsible for this kind of behaviour of ideality factor can be quantitatively explained by evaluating the values of characteristic tunnelling energy (E_{00}). A comparison of E_{00} with thermal energy kT, where k is the Boltzmann constant, shows that the TE dictates the carrier transport for $k\text{T} > E_{00}$, whereas TFE dominates when $k\text{T} \sim E_{00}$. In the extreme case of $k\text{T} < E_{00}$ field emission process governs the carrier transport across metal-semiconductor Schottky diodes [72]. The dependence of ideality factor on E_{00} can be expressed by equation 3.10. One can easily estimate the value of E_{00} by fitting the temperature dependent ideality factor data with equation 3.10 as shown by the dotted line in figure 7.6 (b). It is observed that the two different values of E_{00} have to be considered to reproduce the temperature dependence of ideality factor for pristine and irradiated samples. For pristine sample, E_{00} is estimated to be 9 ± 0.5 meV, which increases to 14 ± 0.5 meV after irradiation. Since a large value of E_{00} (in comparison to kT) indicates suppression of TE mechanism, rise in the value of E_{00} subsequent to irradiation shows that the dislocation assisted tunnelling of carriers across the Schottky junction is enhanced after irradiation.

In order to gain an insight of the current transport mechanisms, the dopant concentration of GaN epilayers obtained from the two values of E_{00} is correlated with a value obtained from Hall measurements using equation 3.8. The N_D values obtained from equation 3.8 for the two values of E_{00} are $5 \pm 0.5 \times 10^{17}$ cm^{-3} and $1.14 \pm 0.08 \times 10^{18}$ cm^{-3} for pristine and 300 kGy irradiated samples. Interestingly, these values of N_D are in good agreement with the donor concentration obtained from the flat region of low temperature Hall data shown in figure 7.2 (a). It certifies that the dislocation assisted carrier transport, which dominates the low temperature Hall experiments, also governs the carrier transport across Schottky junction in both pristine and 300 kGy γ irradiated samples.

After studying the effect of γ irradiation on carrier transport in bulk and Au/Ni/GaN Schottky junctions, it is of prime importance to compare the radiation induced degradation of

GaN with that of the well-established GaAs Schottky junctions. As already discussed in Table 1.1, the displacement energy of Ga and N in GaN are 20.5 and 10.8 eV respectively which is larger than the corresponding values for GaAs. Hence, it is expected that the radiation induced damage in GaN based devices will be less when compared with GaAs devices. To illustrate this point further, the change in leakage current after ^{60}Co γ irradiation in GaN and GaAs based Schottky diodes are compared. The room temperature carrier concentration of GaN and GaAs is chosen to be of the same order (~10^{18} cm^{-3}). The leakage current in pristine and 200kGy irradiated GaN and GaAs detectors of identical geometry is plotted in figure 7.7. As can be seen from figure 7.7, there is a two order increase in leakage current after irradiation in GaAs whereas only a nominal rise of leakage current is observed in case of GaN. A similar observation has been made by Fauzi *et al*. under neutron irradiation [207]. In contrast to the forward bias I-V, the reverse bias leakage current is primarily governed by generation-recombination (g-r) centres within the depletion width. The current due to g-r centres depends on two major parameters, namely the number density of g-r centres and the band gap of material [175]. Because of high displacement energy, the number density of g-r centres after irradiation will be less in GaN. Large band gap of GaN further restricts the increase in g-r current, leading to only a nominal increase in leakage current in comparison to GaAs.

7.5 Effect of Gamma irradiation on GaN Schottky detector

Next, it is worth to investigate the impact of γ irradiation on the charge collection efficiency of GaN based Schottky photodiodes. Here, exposure to γ-radiation primarily affects the charge collection efficiency by reducing the lifetime of photo-generated carriers [208]. In order to explore this point further, I-V characteristics of Au/Ni/GaN Schottky diodes exposed to ^{60}Co γ radiation are recorded and are found to recover within a day as shown in figure 7.8 (a).

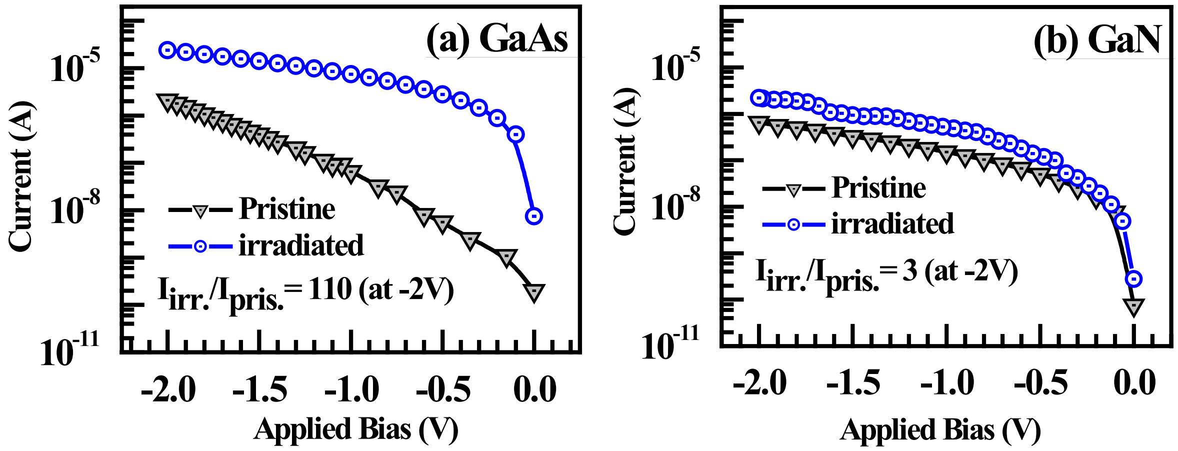

Figure 7.7 Reverse bias I-V characteristics of (a) GaAs, and (b) GaN Schottky diodes, $I_{pris.}$ and $I_{irr.}$ stand for the reverse current for pristine and 200kGy irradiated samples at a reverse bias of -2V.

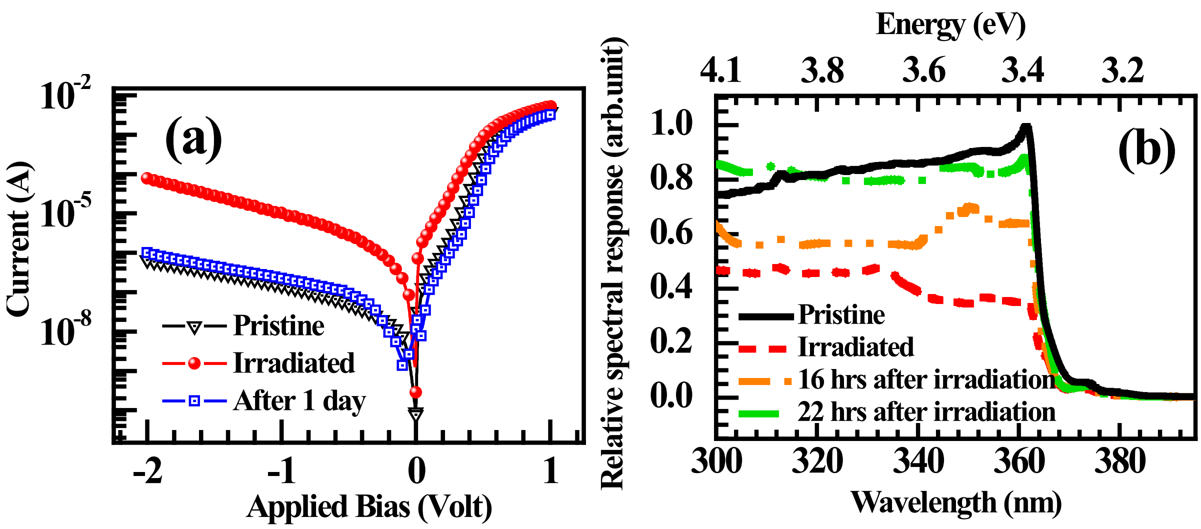

Figure 7.8 Recovery of (a) I-V characteristics of Au/Ni/GaN Schottky diode, (b) Photo response of GaN Schottky photo detector after irradiation with ^{60}Co γ source.

Further, the spectral response of pristine and 200 kGy irradiated GaN Schottky photodiodes is compared in the range of 300 – 400 nm as shown in figure 7.8 (b). The two curves are normalized to the peak response of pristine photodetector in order to make a direct comparison. It is observed that the peak spectral response decreases by 60% after irradiation, which can be attributed to the reduction of charge collection efficiency. Note that the excitonic feature which is clearly observed in pristine sample at 360 nm, also disappears after irradiation.

This is attributed to the irradiation induced decrease in exciton lifetime because of the presence of non-radiative centres. A similar observation in GaAs has been made by Parenteau *et al.* [209]. Interestingly the photo response partially recovers after 16 hours of irradiation which is found to recover completely within a day. Such a recovery of spectral response is attributed to the room temperature annealing of irradiation induced defects states. However, the rate of recovery observed in this work is rather surprising since the recovery time of several weeks at room temperature is usually reported in literature [210]. Self-annealing of irradiation induced defects at room temperature is reported over a month period in case of InGaAs/GaAs quantum well by Dhaka *et al.* [211]. Similarly, a self-recovery of neutron irradiated AlGaN/GaN high electron mobility transistor (HEMT) devices is reported by Kim *et al*. [212] where the electrical response of device completely recovered within 3 weeks of irradiation. The only difference is that the device in the present study is recovered within a day which might be governed by the extent of damage caused by a different type of irradiation in this experiments.

7.6 Conclusion

In conclusion, GaN Schottky photo detectors are fabricated on n^+-GaN epitaxial layers grown by HVPE and the effect of irradiation on the electronic transport in epitaxial layer and Schottky detectors is studied by varying ^{60}Co γ irradiation dose. In contrast to the usual trends seen in moderately doped GaN, a steady rise of carrier concentration is observed with irradiation dose. Using a two layer model, the contribution of bulk layer in measured carrier concentration is extracted and is fitted by considering the charge balance equation. It is observed that the activation energy of donor level remains constant at 32 meV even after irradiation with 500 kGy dose. This indicates that either no new electrically active defects are generated or their activation energy is close to that of the Si donors. However, even the bulk carrier concentration increases after irradiation. It implies about the radiation induced enhancement in activation of native Si impurities which are already present in electrically inert form in pristine sample. It is a unique observation especially for n^+-GaN samples. It is also seen that the irradiation induced nitrogen vacancies stimulate the diffusion of oxygen impurities leading to the observed increase in interfacial carrier concentration after irradiation. It is correlated with the characteristic energy values obtained from the temperature dependent ideality factor variation of pristine and 300kGy irradiated Au/Ni/GaN Schottky devices which confirms that the dislocation-assisted tunnelling dominates the low temperature current transport even after irradiation. Further the leakage current of GaN photodetector is compared with that of GaAs which clearly demonstrate a high radiation tolerance of GaN. The recovery of photo response of GaN photodetector is also studied after 200kGy ^{60}Co γ-irradiation which showed an outright recovery of the spectrum at room temperature within a day. The present work considerably helps in understanding the effect of ^{60}Co γ-irradiation on the electronic transport in n^+-GaN epilayers which are an integral part of nitride devices. The understanding developed here might be very useful in studying the behaviour of nitrides based optoelectronic devices in radiation harsh environment.

Chapter 8

Summary and Future Scope

8.1 Summary of the thesis work

During the course of this thesis, novel electrical characterization techniques are used to investigate the electronic transport in GaN epitaxial layers and Au/Ni/GaN UV detector for potential application in harsh radiation environment. An indigenously developed nitride MOVPE growth system is used for the epitaxial growth of GaN. However, the crystalline quality of GaN layers is found to be rather modest, where a high background carrier concentration makes them unsuitable for photodetector applications. In-depth electronic transport measurements are thereafter performed on commercially available MOVPE and HVPE grown GaN samples. Further, a good control on the dislocation formation during epitaxial growth and a knowledge of dislocation behaviour are the two pre-requisite for optimizing the performance of nitride devices. These two issues are addressed in this thesis where 1) results from the epitaxial growth of GaN are presented by highlighting the issues related to dislocation density, and 2) role of dislocations in the performance of GaN based radiation hard UV photodetectors is explored. In particular, results from the MSM and MOS configurations of GaN photodetectors are presented, where a state-of-the-art performance of GaN based MOS devices is demonstrated.

Systematic electronic transport measurements are performed on 5 μm thick GaN/Sapphire epilayers grown by HVPE and MOVPE technique to understand the fundamental mechanisms associated with current conduction in GaN epilayers and Schottky diode under various experimental conditions. It is found that though the two samples possess a carrier density of ~2×10^{18} cm^{-3}, their electrical characteristics are very different. It is observed that the carrier concentration measured by Hall for HVPE grown samples is two orders larger than the value provided by C-V technique. Such a large difference in carrier concentration is associated with the formation of a degenerate layer at the layer-substrate interface, which is consisted of a large density of threading screw and edge dislocations. A 2-layer model is used to extract the appropriate values of carrier concentration of HVPE grown samples from Hall data. It is learnt that there exists a critical thickness of HVPE GaN epilayers below which the electronic transport properties of layers grown on top of them are severely limited by the interfacial charged dislocations. On the contrary MOVPE grown samples are found to be free from such limitations, which makes them attractive for device fabrication. Further, the impact of dislocations on the electronic transport properties of Au/Ni/GaN Schottky diodes fabricated on HVPE GaN template is evaluated. It is found that one needs to consider the activation of two donors operating in the two separate temperature ranges for understanding the temperature dependence of ideality factor. The two donors correspond to the fundamental mechanisms associated with 1) TE of carriers from bulk donors that dominates at high temperature, and 2) TFE associated with charged dislocations that dominates at low temperature.

Once the electronic transport in GaN epilayer and across Au/Ni/GaN Schottky diode is understood, attention is paid to fabricate GaN MSM UV detectors. From electronic transport studies, it is found that the HVPE GaN epilayers are largely influenced by the threading dislocations. On the other hand, MOVPE GaN epilayers are found be free from such limitations. It is therefore obvious that MOVPE GaN epilayers might be a preferred choice for the fabrication of optoelectronic devices. However, a high cost associated with MOVPE GaN epilayers becomes a major factor that compels researchers to look for other alternatives like HVPE GaN epilayers. MSM photodetectors are made on MOVPE and HVPE GaN epilayers for comparison purpose. Contrary to above, it is surprising to note that the photo response of HVPE based PDs is ~3 times higher than that of the MOVPE based devices. Further, the overall performance of HVPE based PDs is found to be better than those fabricated on MOVPE GaN, in spite of the variations in device geometry or the operating conditions. It is explained by considering the difference in the depletion width which is primarily determined by the different procedures adopted for the doping of HVPE and MOVPE GaN templates. A large carrier concentration at the edge of the depletion width in MOVPE grown GaN epi-layer leads to higher (lower) leakage current (barrier height) despite a low dislocation density. Moreover, Si doping leads to generation of Ga vacancies which act as deep level defects leading to further rise of leakage current and reduction of photo response. In temperature dependent I-V measurements, a sharp change in the value of characteristics tunnelling energy is seen at ~200 K for HVPE GaN, to show the switching of electronic transport mechanism from TE to TFE during the cooling down. On the other hand, TFE is found to be the dominant transport mechanism at all temperature in devices fabricated on MOVPE GaN. The understanding developed here indicates that controlling the density of threading dislocations is not the sole criteria for improving the performance of GaN Schottky PDs, rather one also need to be careful about the density of point defects which can also marginalize the key figure-of-merits. With an aim of improving the device performance further, GaN MOS detector is fabricated by including an oxide layer in the device architecture. The oxide passivated samples show a relatively flat response in shorter wavelength side due to a suppressed surface recombination of photo generated carriers. Moreover, at an optimum ZrO_2 thickness of 3 nm, a high photo responsivity of 27 A/W is achieved along with the fast response of the device with a rise (fall) time of 28 ms (178 ms), respectively. It is also found that the thickness of ZrO_2 layer plays a critical role in controlling the photo-response and transient response of the devices. However, beyond an optimum thickness of oxide interlayer, the device response slows down along with a reduction in responsivity which is mainly governed by the impediment of hole tunnelling across the oxide layer. It is worth to note that the detectivity of PDs with optimized thickness of ZrO_2 interlayer is found to be similar or better than the recently reported state-of-the-art values for visible blind UV GaN PDs with similar dark current.

Fabrication of GaN PIN detector in vertical geometry requires selective spatial etching of the material. In case of GaN, plasma etching is a preferred method since wet chemical etchants are not available. However, during this process, several kinds of plasma-induced damages can lead to the creation of lattice defects and dislocations, ion implantation or formation of dangling bonds on the surface. Impact of RIE induced damage on the optoelectronic properties of GaN epilayers and also on the photoresponse of Schottky PDs is investigated further. The observation of surface morphology of GaN epilayers post RIE confirms a large degradation with increasing energy of the reactive ion beam. More than 70% reduction in the intensity of near band edge PL peak is observed after 250W RF BCl_3 plasma etching which along with the etch insensitive YL band suggests that etch induced non-radiative centres are located rather close to the surface. This observation is further supported by C-V measurements on Au/Ni/GaN Schottky diodes which along with SIMS results confirm that the RIE induced damage is mostly confined within 100 nm from the sample surface. The peak spectral response of PDs also shows up to 90% reduction post plasma etching. A method for the recovery of plasma etch induced damage by O_2 plasma treatment is also demonstrated. A substantial recovery of the spectral and transient response along with an improved deep UV response of PDs is achieved through O_2 plasma treatment. Availability of this knowledge shall be highly beneficial in gaining the required understanding of RIE induced damage and also in the minimization of plasma etch induced degradation in the performance of GaN devices.

One of the major aims of this thesis is to test the performance of devices under high radiation environment. Here, the effect of ^{60}Co gamma irradiation on the electronic transport properties of heavily doped n-type GaN epilayers and Schottky PDs is investigated. A steady rise of carrier concentration with increasing irradiation dose is observed. By considering a 2-layer model, the contribution of interfacial dislocations in carrier transport is isolated from that of the bulk layer for both the pristine and irradiated samples. It is found that no new kind of electrically active defects are generated by gamma radiation even at 500 kGy dose. The irradiation induced rise of carrier concentration is attributed to the activation of native Si impurities that are already present in an electrically inert form in the pristine sample. This observation is found to be unique, especially for highly conducting samples. It is also seen that the irradiation induced nitrogen vacancies stimulate the diffusion of oxygen impurities, leading to the observed increase of the interfacial carrier concentration. Further, the leakage current of GaN PDs is compared with that of GaAs which clearly demonstrates a high radiation resistance of GaN. A fast self-recovery of photo response within a day after irradiation is also demonstrated, which signifies the compatibility of devices for operation in high radiation zones.

In conclusion, it is essential to understand the electronic transport properties of GaN/Sapphire epitaxial layers and the role of charged dislocations lying at the interface, prior to the fabrication of devices. A comparison of the spectral and transient response of PDs fabricated on GaN templates can help the device manufacturers in making a judicious choice of GaN templates. Further, an optimum thickness of ZrO_2 layer is needed for the development of state-of-the-art GaN PDs. Radiation resistant nature of GaN PDs along with a fast self-recovery makes them attractive for possible applications in high radiation zones. The understanding developed in this thesis is useful for the development of high performance radiation hard GaN ultraviolet PDs.

8.2 Scope for future work

The understanding developed in the present thesis can be further strengthened by addressing several unresolved issues in the fabrication and characterization of GaN epitaxial layers and UV detectors that deserve further investigations. In presence of a large density of structural defects and dislocations in GaN, it is really challenging to grow superior quality GaN epitaxial layers on Sapphire. Optimization of the epitaxial growth parameters to achieve low background free carrier density is one of the major requirement to improve the performance of the GaN UV detectors. Controlling the density of defect and trap centres will not only reduce the dark current but also encourage faster response of the device since it will reduce the response delay due to hole trapping at the defect centres. Growth of epitaxial lateral overgrowth (ELOG) GaN epilayers on patterned substrates need to be explored in this context as this is a very promising approach for effective reduction in dislocation density of GaN epilayers. Also conductive atomic force microscopy (C-AFM) surface scan can help in obtaining the information about the electrically active dislocations present at the GaN surface which largely controls the low temperature carrier transport. In device aspect, scaling down the dimension of the MSM electrodes is the necessary requirement to achieve advancement in existing device performance. This will help in reducing the dark current and improve the responsivity and detectivity as well as transient response time of the device. Also a detailed analysis of GaN PIN detector is required to explore the new possibilities that PIN detector offers including detection of very weak signal. In this context, the role of dry etching for the fabrication of PIN detector can be better understood by using ICP RIE technology with which it is possible to decouple ion current and ion energy applied to the wafer, enlarging the process window.

In the radiation hard detector application part, performance evaluation under different radiation environment like neutron, electron, x-rays is necessary to demonstrate versatile applications of the device in the radiation field. Also understanding the role of high temperature annealing for quick recovery the radiation induced damages in these detectors will be highly beneficial for the field applications of these detector devices.

Annexure 1

CERTIFICATION ON ACADEMIC INTEGRITY

1. I **ABHISHEK CHATTERJEE**, HBNI Enrolment No. PHYS03201504011, hereby undertake that, the Thesis titled ***ELECTRONIC TRANSPORT STUDIES ON GaN EPITAXIAL LAYERS FOR THE FABRICATION OF RADIATION HARD ULTRAVIOLET PHOTODETECTORS*** is prepared by me and is the original work undertaken by me and free of any plagiarism. That the document has been duly checked through a plagiarism detection tool and the document is plagiarism free.

2. I am aware and undertake that if plagiarism is detected in my thesis at any stage in future, suitable penalty will be imposed as per the applicable guidelines of the Institute/ UGC.

Abhishek Chatterjee
Date: 07/04/2021

Endorsed by Ph.D. Thesis Supervisor
(I certify that the work done by the Researcher is plagiarism free)

07/04/2021
Signature (with date)

Name: Tarun Kumar Sharma
Designation: Professor, & Head MSS, RRCAT
Department/ Centre: Materials Science Section, RRCAT
Name of the CI/ OCC: Raja Ramanna Centre for Advanced Technology

Thesis Highlights

Name of the Student: Abhishek Chatterjee

Name of the CI/OCC: Prof. T. K. Sharma **Enrolment No.: PHYS03201504011**

Thesis Title: Electronic transport studies on GaN epitaxial layers for the fabrication of radiation hard ultraviolet photodetectors

Discipline: Physical Science **Sub-Area of Discipline:** Semiconductor Physics

Date of viva voce: 19/03/2021

This thesis deals with the fabrication of high performance GaN based ultraviolet (UV) photodetectors (PDs) for potential application in high radiation environment. Owing to a wide band gap, GaN based optoelectronic devices are capable to operate under high electric field often exceeding 1 kV and at high temperatures up to 600 ^{o}C. However, a large density of dislocations in nitride heterostructures is often proven to be a limiting factor. Thus, a good control on the dislocation formation during epitaxial growth and a knowledge of dislocation behaviour are the two pre-requisite for optimizing the performance of nitride devices. The two issues are addressed in this thesis where 1) results from the epitaxial growth of GaN are presented by highlighting the issues related to dislocation density, and 2) role of dislocations in the performance of GaN based radiation hard UV photodetectors is explored.

An indigenously developed nitride Metal Organic Vapour Phase Epitaxy (MOVPE) system is used for the epitaxial growth of GaN epitaxial layers. However, the crystalline quality of GaN layers is found to be rather modest, where a high background carrier concentration makes them unsuitable for photodetector applications. In-depth electronic transport measurements are thereafter performed on commercially available MOVPE and Hydride Vapour Phase Epitaxy (HVPE) grown GaN samples. Presence of a highly conducting interfacial layer is observed in HVPE GaN epilayers. On the other hand, MOVPE GaN epilayers are found to be free from this limitation which makes them attractive for the device development. Metal-semiconductor-metal (MSM) PDs are thereafter made on both the samples where the performance of devices made on HVPE GaN turns out to be better, which is rather surprising. It is explained by citing the difference in doping method of the GaN epi-layers in the two samples. A method to enhance the detector performance is demonstrated by the insertion of a thin layer of ZrO_2 in metal-oxide-semiconductor (MOS) geometry. Here, the role of ZrO_2 layer thickness is found to be rather critical where the specific detectivity of PDs is found to be similar or better than the state-of-the-art values reported in literature. Further, the role of dry etching in the fabrication of GaN PIN detectors in vertical geometry is discussed where a method to recover the etching induce damage is demonstrated by using post etch O_2 plasma treatment. A few samples are also exposed to a high dose of ^{60}Co gamma rays which proves the radiation resistant nature of indigenously developed PDs along with a fast self-recovery, which signifies their usefulness for possible applications in harsh radiation environment. Systematic electronic transport measurements are performed to understand the fundamental mechanisms associated with current conduction in GaN epilayers and PDs under various experimental conditions. The understanding developed in this thesis is useful for the development of high performance radiation hard GaN ultraviolet PDs.

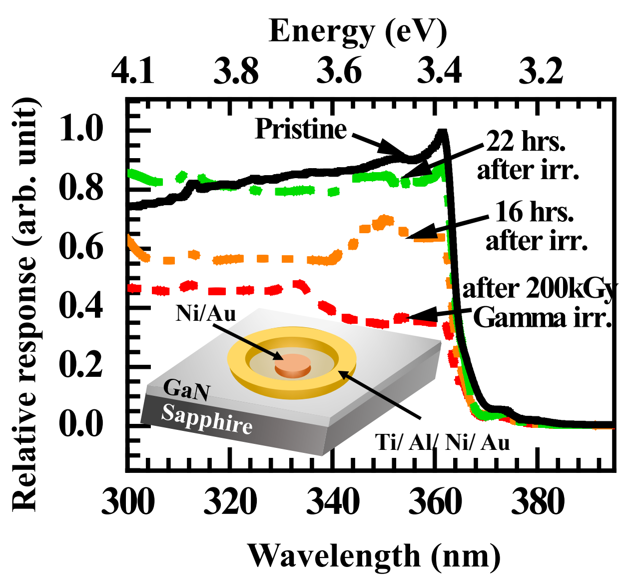

Fig.1: Photo response of GaN Schottky photo detector after irradiation with ^{60}Co Gamma source. Inset shows the schematic of device geometry.